UNIVERSITY OF CALIFORNIA, SAN DIEGO

Interaction and transport in low-dimensional carbon nanostructures

A dissertation submitted in partial satisfaction of the
requirements for the degree
Doctor of Philosophy

in

Phyiscs

by

Lingfeng M. Zhang

Committee in charge:

Professor Michael Fogler, Chair
Professor Daniel Arovas
Professor Prabhakar Bandaru
Professor Leonid Butov
Professor Yuan Taur

2010

The dissertation of Lingfeng M. Zhang is approved, and it is acceptable in quality and form for publication on microfilm and electronically:

_____

_____

_____

_____

_____
Chair

University of California, San Diego

2010

DEDICATION

To my family.

EPIGRAPH

A problem daily makes a theorist happy.

—anonymous

TABLE OF CONTENTS

LIST OF FIGURES

LIST OF TABLES

ACKNOWLEDGEMENTS

This thesis is an accumulation of works in the last six years, over which I cannot be successful without the help and encouragement of many. Foremost is my thesis advisor Prof. Misha Fogler, whose patience, motivation, and constant assistance helped me with problems after problems in the completion of this tome. Prof. D. Arovas, Dr. Z. Q. Li, and Prof. D. Bassov, who we collaborate with, have been a constant source of fruitful discussion and inspiring ideas. Also, Dr. A. Meyertholen and Mr. A. Rodin are both excellent physicists and colleagues off whom I have bounced countless stupid ideas.

I have learned so much from the many great physicists of the Department in the past few years. Specifically, the memorable and challenging classes offered by Prof. M. Di Ventura, Prof. T. Hwa, Prof. C-J. Wu, and others, have made me a much better physicist. I would like also to thank the members of my committee.

I am thankful for the help of the Physics Department staff in various academic and administrative areas.

On a more personal note, I appreciates the friendship from all the new acquaintances I made in San Diego who made graduate life, which can otherwise be dull sometimes, enjoyable.

Finally, I am eternally indebted to his parents for their patience, aspiration, dedication, and allowance over the years.

Chapter 2, almost in full, is a reprint of the materials as it appears in L. M. Zhang and M. M. Fogler. Nonlinear screening and ballistic transport in a graphene p-n junction. *Phys. Rev. Lett.*, 100(11):116804, 2008. Chapter 3, almost in full, is a reprint of material as it appears in L. M. Zhang, Z. Q. Li, D. N. Basov, M. M. Fogler, Z. Hao, and M. C. Martin. Determination of the electronic structure of bilayer graphene from infrared spectroscopy. *Phys. Rev. B*, 78(23):235408, 2008. Chapter 4, almost in full, is a reprint of an unpublished manuscript L. M. Zhang, M. M. Fogler, and D. P. Arovas Magnetoelectric coupling, berry phase, and landau level dispersion in a biased bilayer graphene. (Unpublished), 2010. It is submitted to *Phys. Rev. B*. The dissertation author was the primary investigator and author of all the above papers.

VITA

2003	B. S. in Engineering Physics, University of California, Berkeley
2003-2010	Teaching and Research Assistance, University of California, San Diego
2010	Ph. D. in Physics, University of California, San Diego

PUBLICATIONS

L. M. Zhang and M. M. Fogler. Scanned gate microscopy of a one-dimensional quantum dot. *Nano Lett.*, 6:2206, 2006.

L. M. Zhang and M. M. Fogler. Nonlinear screening and ballistic transport in a graphene p-n junction. *Phys. Rev. Lett.*, 100(11):116804, 2008.

L. M. Zhang, Z. Q. Li, D. N. Basov, M. M. Fogler, Z. Hao, and M. C. Martin. Determination of the electronic structure of bilayer graphene from infrared spectroscopy. *Phys. Rev. B*, 78(23):235408, 2008.

L. M. Zhang, M. M. Fogler, and D. P. Arovas Magnetoelectric coupling, berry phase, and landau level dispersion in a biased bilayer graphene. (Unpublished), 2010.

ABSTRACT OF THE DISSERTATION

Interaction and transport in low-dimensional carbon nanostructures

by

Lingfeng M. Zhang

Doctor of Philosophy in Phyiscs

University of California, San Diego, 2010

Professor Michael Fogler, Chair

Mono and bilayer graphene are novel carbon materials with many remarkable properties. Their electronic properties, including the basic band structure, can be tuned by electrostatic gating. Calculation of the effect of the gate requires solving self-consistent screening problem. An overview of the electronic properties of graphene system is given in Chapter 1. Chapter 2 illustrates the physics of Dirac fermion on the example of a graphene p-n junction. The results are shown to be essential for experimental verification of Klein tunneling in graphene. Chapter 3 discusses the effect of gating on bilayer graphene and how their signatures have been observed by the IR spectroscopy. Chapter 4 discusses the theory of semiclassical Landau quantization in bilayer subject to both electric and magnetic fields. This explains the role of the Berry phase, valley polarization.

Chapter 1

Overview and Introduction

1.1 Introduction

Carbon based systems have shown tremendously versatilities in that not only is carbon atom the base of all organic chemistry, the flexibility in the bonding behavior allows for an unlimited number of structures with a large variety of physical characteristics. This work study a system that consists only of carbon atoms, graphene–a two dimensional allotrope of carbon–which is the basis for the understanding of the electronic properties in other carbon-only system. The carbon atoms in graphene occupy a honeycomb structure or equivalently that it has a hexagonal crystal structure with two atoms per unit cell.

Graphene is the basic building block of other carbon-only systems with perhaps the exception of diamond. For example, Fullerenes are molecules in which carbon atoms are arranged spherically and therefore is a zero-dimensional object. Fullerenes can be thought of as wrapped-up graphene because it can be obtained from graphene with the introduction of pentagons defects that creates positive curvature. Carbon nanotubes are obtained by rolling a graphene sheet along a particular direction. Carbon nanotube also consists only of hexagon and can be thought of as a one dimensional object. Finally, graphite, the most common form of carbon, is obtained by stacking graphene layers with only the weak van der Waals force coupling between the layers. This weakness of interlayer coupling is what makes pencil useful.

Being such an abundant material, it is perhaps somewhat surprising that only centuries [5] later a single atomic flake of graphene was finally isolated in the laboratory. In order to isolate and identify graphene flakes, one would first need the experimental tools to search for one-atom-thick [6]. The optical effects that graphene sitting on top of SiO_2 substrates [5] finally allows its observation with optical microscopy [7].

The band structure of graphene was first written by P. R. Wallas who showed that graphene is a gapless semimetal. [8]. His work was done in the context of research in graphite. During the ensuing years, the study of graphite culminated with the Slonczewski-Weiss-McClure (SWMc) band theory of graphite, which describes the electronic property of this material [9, 10] and agrees well with the experimental data [11, 12, 13, 14, 15, 16]. The SWM model is however unable to describe the van der Waals-like interactions between graphene planes, a problem that requires the understanding of many-body effects that go beyond the band-structure description [17, 18, 19]. This issue of course do not concern graphene monolayer but would be present in the cased of stacked graphene system such as bilayer or trilayer. Stacking can therefore change the electronic properties of considerably and as we will see in Chapter 3 and 4.

A major reason that graphene has attracted much attention, especially by theoreticians, is that its low-energy excitations are massless, chiral, Dirac fermions. The low energy spectrum of graphene is that of two Dirac cones and in neutral graphene the chemical potential is at exactly the Dirac point where the tip of the two cones meet (see Sec. 1.2). The low energy dispersion then mimics the physics of quantum electrodynamics (QED) for massless fermion except that the fermion in graphene moves with Fermi velocity v_F, which is a about 300 times smaller than the speed of light c. As a result, graphene is a condensed matter system in which one can potentially observe many of the unusual properties of QED, albeit with the slower "light speed"[20, 21, 22].

One such interesting feature of Dirac fermion is their behavior under an external electrostatic potential due to the so-called Klein paradox. That is, under an external potential, the Dirac fermions can be transmitted with probability one

through a classically forbidden region [23, 24]. In QED where the charged fermion electron is massive, Klein tunneling occurs only for large electric field that creates a potential energy difference of order $m_e c^2$ within the tunneling distance, an impossible feat. In graphene where we have massively quasiparticle, however, it is clearly possible. Indeed, Klein tunneling is the basis on which the transport properties of graphene p-n junction can be explain (See Chapter 2). It's been noted [24] that Dirac fermion behave unusually in the presence of a confining potentials, leading to the phenomenon of *Zitterbewegung*, or jittery motion of the wave function. In graphene, confining potential of electron and hole is always present due to unavoidable disorder in any material. Therefore, the effect of disorder on the electrons in graphene and its transport properties has attracted a lot of interests. The starting point of all these is the band structure of graphene, which one can obtain from a tight-binding description.

1.2 Single Layer Tight-binding Hamiltonian

Here we give a quick overview of the Dirac particle nature of graphene's low energy Hamiltonian. Wallace [8] first computed the band structure of graphene in the context of the study of graphite. The lattice stucture and the corresponding first Brillouin zone in the reciprocal lattice space shown in Fig. 1.1 Within the tight-binding model, graphene monolayer has the following Hamiltonian as function of reciprocal space vector $\boldsymbol{q}$:

$$H_{\mathrm{MLG}} = -\gamma_0 \begin{pmatrix} 0 & S_{\boldsymbol{q}} \\ S_{\boldsymbol{q}}^* & 0 \end{pmatrix} , \tag{1.1}$$

where $\gamma_0 \approx 3.0\mathrm{eV}$ is the nearest neighbor hopping integral. Here, as in Wallace[8], we define the dimensionless in-plane hopping amplitude

$$S_{\boldsymbol{q}} = \exp\left(-i\,\boldsymbol{\delta}_1 \cdot \boldsymbol{q}\right) + \exp\left(-i\,\boldsymbol{\delta}_2 \cdot \boldsymbol{q}\right) + \exp\left(-i\,\boldsymbol{\delta}_3 \cdot \boldsymbol{q}\right) , \tag{1.2}$$

in which $\boldsymbol{\delta}_1 = \left(-\frac{\sqrt{3}}{2}, -\frac{1}{2}\right)\delta_0$, $\boldsymbol{\delta}_2 = \left(\frac{\sqrt{3}}{2}, -\frac{1}{2}\right)\delta_0$, and $\boldsymbol{\delta}_3 = (0,1)\,\delta_0$ are the three lattice vectors (Fig. 1.1).

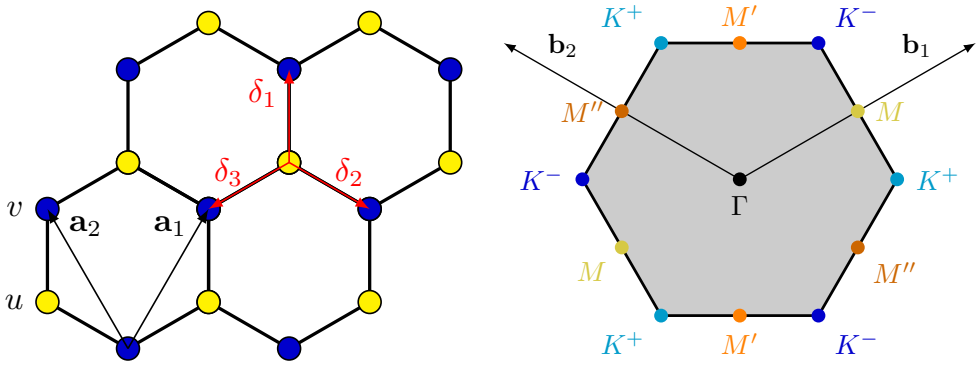

Figure 1.1: Atomic lattice vectors and first Brillouin zone of the corresponding reciprocal lattice space of graphene. The lattice constant $\delta_0 \approx 1.44$Å. Since there are two atoms per unit cell, the six corners of the Brillouin zone consists of two classes of inequivalent points called valley, denoted K^+ and K^-

The monolayer graphene Hamiltonian Eq. (1.1) can be diagonalized to yield the band structure. We find that $E(\boldsymbol{q}) = \pm\gamma_0 |S_{\boldsymbol{q}}(\boldsymbol{q})|$, and

$$|S_{\boldsymbol{q}}|^2 = 3 + 2\cos\left(\sqrt{3}p_y\right) + 4\cos\left(\frac{3}{2}p_x\right)\cos\left(\frac{\sqrt{3}}{2}p_y\right) \tag{1.3}$$

A plot of the band along few edges of the Brillouin zone is plotted in Fig. 1.2.

The low energy behavior of graphene is dominated by excitation near the two inequivalent K-points (valleys). Expanding $S_{\boldsymbol{q}}$ about each:

$$S_{\boldsymbol{q}}(\pm\boldsymbol{K} + \boldsymbol{p}) \simeq -\frac{3}{2}(\pm p_x + ip_y)\ , \tag{1.4}$$

in which we take the $+[-]$ sign for the $K^+[K^-]$ valley. The Hamiltonian near each valley takes the form:

$$H^{\pm}_{\mathrm{MLG}} = v_0 \begin{pmatrix} 0 & \pi^{\pm} \\ (\pi^{\pm})^* & 0 \end{pmatrix}\ , \tag{1.5}$$

where $\pi^{\pm} = \pm p_x + ip_y = \pm p e^{\pm i\varphi_p}$ and $v_0 = \frac{3}{2}\frac{\gamma_0\delta_0}{\hbar}$ is the Fermi velocity. $v_0 \approx 10^8$.

Eq. (1.5) is the Hamiltonian for a massless Dirac particle. It can be rewritten as

$$H^{\pm} = \boldsymbol{\sigma}^{\pm} \cdot \boldsymbol{p} \tag{1.6}$$

with $\boldsymbol{\sigma}^{\pm} \equiv \pm\sigma_x\,\hat{\boldsymbol{x}} - \sigma_y\,\hat{\boldsymbol{y}}$. σ_x and σ_y are the Dirac matrices. Eq. (1.6) is not manifestly covariant. For completeness, the full time-dependent Schrödinger-Dirac

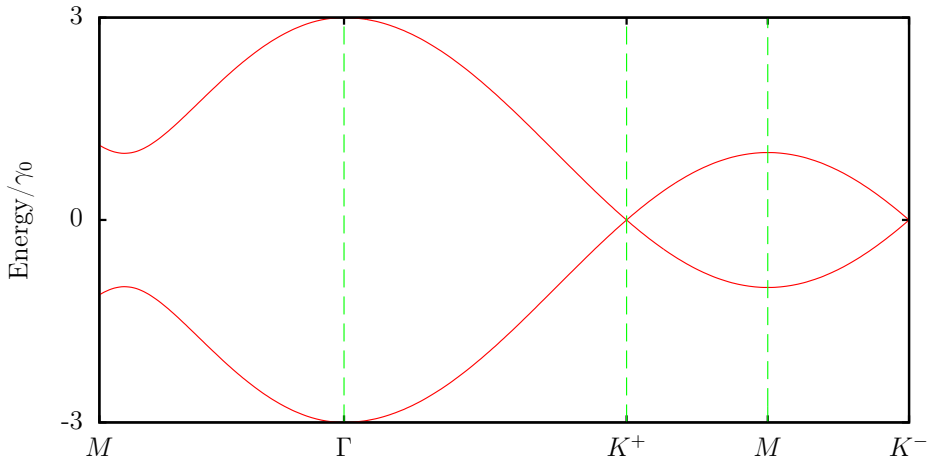

Figure 1.2: Monolayer graphene energy band along few edges of the Brillouin zone.

equation in Lorentz covariant form is:

$$0 = \gamma^\mu \partial_\mu \, \varphi \, , \tag{1.7}$$

with $\gamma^0 = \sigma_z$, $\gamma^1 = i\,\sigma_y$, and $\gamma^2 = -i\,\sigma_x$. Written in this form, one can easily perform a Lorentz boost by using the matrix in spinor space:

$$\Lambda_{\text{spinor}}\,(\theta, \hat{n}) = \exp\left(\frac{\theta}{2}\,\hat{n}\cdot\boldsymbol{\sigma}\right) . \tag{1.8}$$

Eq. (1.8) corresponds to boost in the $\hat{n}$ direction with speed $\beta = \tanh\theta$.

1.2.1 Zero magnetic field

Well known from previous literature [25], the band structure of bilayer graphene is shown in Fig. 1.3. In this section we summarize its main properties, focusing on analytic results.

The unit cell of a graphene bilayer, depicted in Fig. 1.4, consists of four atoms, which we label u, v, $\tilde{u}$, and $\tilde{v}$. The underlying Bravais lattice is the triangular Bravais lattice of either honeycomb monolayer (Fig. 1.1). The Bravais lattice sites are at locations $\boldsymbol{R} = n_1\,\boldsymbol{a}_1 + n_2\,\boldsymbol{a}_2$, where $\boldsymbol{a}_1 = a_0\,\hat{\boldsymbol{x}}$ and $\boldsymbol{a}_2 = a_0\left(\frac{1}{2}\hat{\boldsymbol{x}} + \frac{\sqrt{3}}{2}\hat{\boldsymbol{y}}\right)$ are primitive direct lattice vectors, $n_{1,2}$ are integers, and $a_0 = 2.461\,\text{Å}$ is again

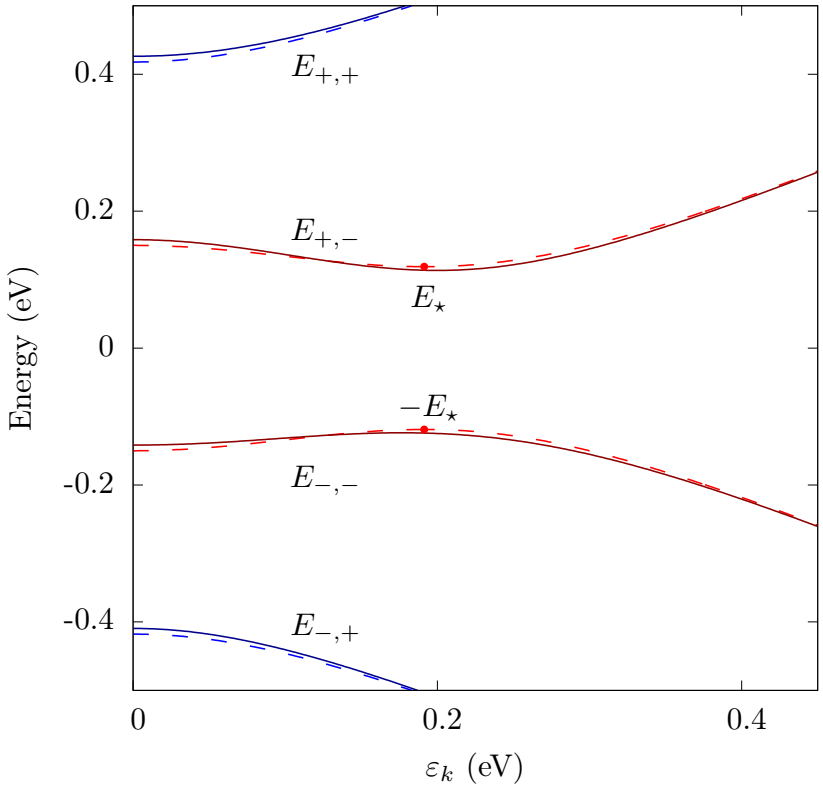

Figure 1.3: BLG band dispersion as a function of $\varepsilon_k = \hbar v_0 k$, where k is the momentum measured from the nearest $K^\pm$ point. At $B = 0$ the bands are valley-degenerate. The dashed curves show their dispersion calculated from Eq. (1.14) for the interlayer bias $2U = 240\,\text{meV}$. In a finite field, the bands acquire a pseudo-Zeeman shift, Eq. (4.36), opposite in the two valleys. The solid curves show the result for K^+ at $B = 5\,\text{T}$.

the lattice constant. The corresponding elementary reciprocal lattice vectors are $\boldsymbol{b}_1 = \frac{4\pi}{a_0\sqrt{3}}\Big(\frac{\sqrt{3}}{2}\hat{\boldsymbol{x}} - \frac{1}{2}\hat{\boldsymbol{y}}\Big)$ and $\boldsymbol{b}_2 = \frac{4\pi}{a_0\sqrt{3}}\,\hat{\boldsymbol{y}}$. The three nearest neighbor separation vectors $\boldsymbol{\delta}_{1,2,3}$ are given by $\boldsymbol{\delta}_1 = -\frac{1}{3}\,\boldsymbol{a}_1 - \frac{1}{3}\boldsymbol{a}_2$, $\boldsymbol{\delta}_2 = \frac{2}{3}\,\boldsymbol{a}_1 - \frac{1}{3}\boldsymbol{a}_2$, and $\boldsymbol{\delta}_3 = -\frac{1}{3}\,\boldsymbol{a}_1 + \frac{2}{3}\boldsymbol{a}_2$, each of length $|\boldsymbol{\delta}_j| = a_0/\sqrt{3} = 1.42\,\text{Å}$. The in-plane locations of the four sublattices are then given by the subscripts: $u_{\boldsymbol{R}}$, $v_{\boldsymbol{R}+\boldsymbol{\delta}_1}$, $\tilde{u}_{\boldsymbol{R}+\boldsymbol{\delta}_1}$, and $\tilde{v}_{\boldsymbol{R}-\boldsymbol{\delta}_1}$, and the separation between the (u, v) and $(\tilde{u}, \tilde{v})$ planes is $d = 3.35\,\text{Å}$. The $(\tilde{u}, \tilde{v})$ layer (B) is shifted by $\boldsymbol{\delta}_1$ relative to the (u, v) layer (A), a configuration known as Bernal stacking.

Repeating the Bernal stacking ABABAB... generates the common form of graphite. In graphite, the v and $\tilde{u}$ sublattices form one-dimensional chains, while the u and $\tilde{v}$ sites lie above and below hexagon centers in neighboring planes. The electronic structure of graphite dates to the seminal work of Wallace[8] and subsequent work by McClure[9] and by Slonczewski and Weiss[10], known as the Slonczewski-Weiss-McClure (SWMc) model. The SWMc model is equivalent to a seven-parameter tight binding model which describes nearest neighbor in-plane hopping (amplitude $-\gamma_0$), three interplane hopping processes $(\gamma_1, \gamma_3, \gamma_4)$, two next-nearest plane hoppings (γ_2, γ_5), and an on-site energy shift Δ' which distinguishes the chain sites $(v, \tilde{u})$ from the non-chain sites $(u, \tilde{v})$ in each unit cell[1]. The numerical values we assume are: $\gamma_0 = 3.0\,\text{eV}$, $\gamma_1 = 0.41\,\text{eV}$, $\gamma_3 = 0.3\,\text{eV}$, $\gamma_4 = 0.15\,\text{eV}$, and $\Delta' = 0.018\,\text{eV}$. For the interpretation of these parameters within the tight-binding picture, see Fig. 1.4. For a discussion of their numerical values, including the uncertainties, see Ref. [1]. Finally, to describe a gated bilayer, we include a scalar potential $\pm U$ on the different monolayers.

The Hamiltonian in second quantized notation is written as $\widehat{H} = \sum_{\mathbf{q}} \Psi^\dagger_{\mathbf{q}}\, H_{\mathbf{q}}\, \Psi_{\mathbf{q}}$, where

$$\Psi^\dagger_{\mathbf{q}} = \begin{pmatrix} u^\dagger_{\mathbf{q}} & v^\dagger_{\mathbf{q}} & \tilde{u}^\dagger_{\mathbf{q}} & \tilde{v}^\dagger_{\mathbf{q}} \end{pmatrix}, \tag{1.9}$$

[1]The SWMC parameter Δ combines the intrinsic on-site energy shift Δ' with the hopping parameters γ_s and γ_5, with $\Delta' = \Delta - \gamma_2 + \gamma_5$. In bilayer graphene, the hoppings γ_2 and γ_5 do not enter, and we are left with five parameters. One further expects[1] $\Delta'_{\text{BLG}} = \frac{1}{2}\Delta'_{\text{graphite}}$.

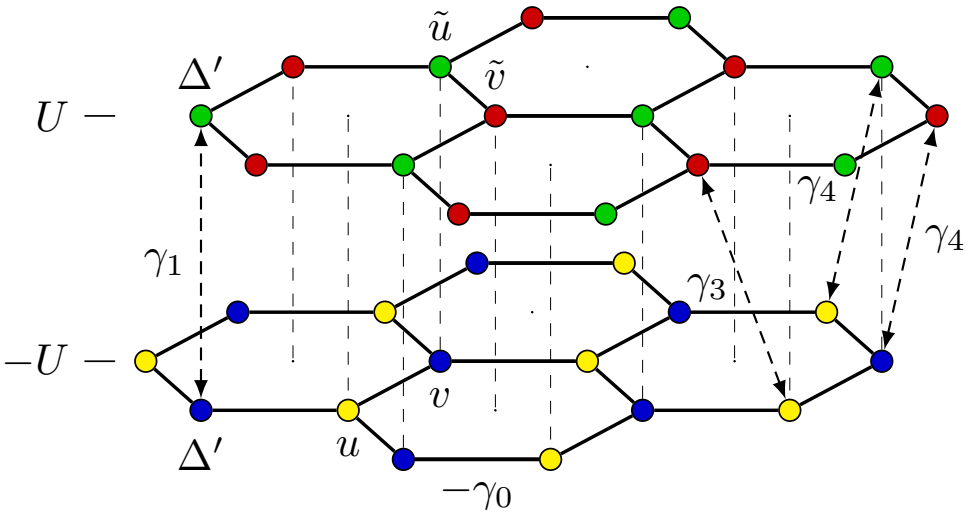

Figure 1.4: Crystal structure of bilayer graphene. We label four sublattices by u, v, $\tilde{u}$, $\tilde{v}$. Also shown is the assignment of the hopping parameters γ_j of the tight-binding model. The labels $\pm U$ indicate the electrostatic potential energies of the layers.

is a four (sublattice) component creation operator with crystal momentum $\mathbf{q}$, and

$$H_{\mathbf{q}} = \begin{pmatrix} -U & -\gamma_0\, S_{\mathbf{q}} & \gamma_4\, S_{\mathbf{q}} & \gamma_3\, S_{\mathbf{q}}^* \\ -\gamma_0\, S_{\mathbf{q}}^* & -U+\Delta' & \gamma_1 & \gamma_4\, S_{\mathbf{q}} \\ \gamma_4\, S_{\mathbf{q}}^* & \gamma_1 & U+\Delta' & -\gamma_0\, S_{\mathbf{q}} \\ \gamma_3\, S_{\mathbf{q}} & \gamma_4\, S_{\mathbf{q}}^* & -\gamma_0\, S_{\mathbf{q}}^* & U \end{pmatrix} . \tag{1.10}$$

In the vicinity of the two inequivalent Brillouin zone corners $\mathbf{q} = \pm\mathbf{K}$ (see Fig. 1.1), the function $S_{\mathbf{q}}$ vanishes, and writing $\mathbf{q} = \pm\mathbf{K} + \mathbf{k}$ one finds

$$S_{\mathbf{K}+\mathbf{k}} = -\frac{\sqrt{3}}{2}\left(k_x - ik_y\right)a_0 + \mathcal{O}(k^2)\,, \tag{1.11}$$

$$S_{-\mathbf{K}+\mathbf{k}} = +\frac{\sqrt{3}}{2}\left(k_x + ik_y\right)a_0 + \mathcal{O}(k^2)\,. \tag{1.12}$$

Setting all parameters but γ_0 to zero, one obtains the monolayer dispersion,

$$\varepsilon_k = \gamma_0|S_{\mathbf{q}}| = \hbar v_0|\mathbf{k}| + \mathcal{O}(k^2)\ , \tag{1.13}$$

where $v_0 = \sqrt{3}\gamma_0 a_0/2\hbar \approx 1.0 \times 10^8\,\mathrm{cm/s}$ is the Fermi velocity.

If we turn on the interlayer hopping γ_1 and the interlayer potential U, keeping $\gamma_3 = \gamma_4 = \Delta' = 0$, we obtain[2] the spectrum

$$E_{s_1 s_2, k} = s_1 \sqrt{\frac{1}{2}\gamma_1^2 + U^2 + \varepsilon^2 + s_2\, \Lambda^2(\varepsilon_k)}\,, \tag{1.14}$$

$$\Lambda(\varepsilon) \equiv \left[\frac{1}{4}\gamma_1^4 + (\gamma_1^2 + 4U^2)\,\varepsilon^2\right]^{1/4}. \tag{1.15}$$

Here s_1 and s_2 label the four bands as follows: $s_1 = \pm$ labels the conduction and valence bands, respectively, while $s_2 = +1$ for the outer bands and $s_2 = -1$ for the inner bands. Thus, the ordering of levels is

$$E_{-+} < E_{--} \le E_{+-} < E_{++}\,. \tag{1.16}$$

(For aesthetic reasons, we will usually abbreviate $s_{1,2} = \pm$ in the subscripts, as above.)

Due to particle - hole symmetry when $\gamma_4 = \Delta' = 0$, we may restrict our attention to the conduction bands $s_1 = +1$. In this case, the shape of the energy bands is as follows. For the outer band, E_{++} is a monotonic function of ε, starting at $\mathbf{q} = \pm\mathbf{K}$, where $E_{++} = E_\diamond \equiv \sqrt{\gamma_1^2 + U^2}$ and extending to $E_{++}(0) \approx 3\gamma_0$ (assuming $\gamma_0 \gg \gamma_1, U$). We will be interested mainly in the inner ($s_2 = -1$) bands, shaped as the Mexican hats near $\mathbf{q} = \mathbf{K}^\pm$, i.e., $\mathbf{k} = 0$. For example, the conduction band $E_{+-,k}$ has a local maximum at $\varepsilon_k = 0$, where $E_{+-} = U$ and a local minimum at $\varepsilon_k = \varepsilon_\star$, where

$$\varepsilon_\star = \sqrt{U^2 + E_\star^2}\,, \quad E_\star = \frac{\gamma_1 U}{\sqrt{\gamma_1^2 + 4U^2}}\,. \tag{1.17}$$

Thus, this minimum is attained on circles of radius $k_\star = \varepsilon_\star/\hbar v_0$, centered at the zone corners.

Inverting the relation between E and ε, and suppressing the labels $s_{1,2}$, one finds

$$\varepsilon_k^2 = E_k^2 + U^2 - s_3 \Gamma^2(E_k)\,, \tag{1.18}$$

$$\Gamma(E) \equiv \left[(\gamma_1^2 + 4U^2)E^2 - \gamma_1^2\, U^2\right]^{1/4}, \tag{1.19}$$

[2]The main effect of finite γ_4 and Δ' is to produce a small but measurable electron-hole asymmetry. [1]

where $s_3 = \pm 1$. This equation has no solutions when $E^2 < E_\star^2$, which is the band gap. There are two solutions when $E_\star \leq |E| \leq U$, both in the inner ($s_2 = -1$) band. For $U \leq |E| \leq E_\diamond \equiv \sqrt{U^2 + \gamma_1^2}$, the energy is between the local maximum of the inner band and the minimum of the outer band, and there is one solution. Finally, for $|E| > E_\diamond$ there are again two solutions, one with $s_2 = -1$ and one with $s_2 = +1$. As we shall see in Sec. 4.4.1, the existence of two solutions E within the inner band — one on the inside and the other on the outside of the Mexican hat — gives rise to multiple level crossings when magnetic field is turned on.

If one is interested only in the inner bands and low energies, $|E_{s_1,-,k}| \ll \gamma_1$, one can implement a unitary transformation, discussed in Appendix 4.7.1, which decouples the inner ($s_2 = -1$) and outer ($s_2 = +1$) bands. [26, 27] The results of this procedure are further described in Sec. 4.2.1.

Chapter 2

Nonlinear screening and ballistic transport in a graphene p-n junction

As reviewed in Chapter 1, a monolayer graphene is a gapless two-dimensional (2D) semiconductor whose quasiparticles (electrons and holes) move with a constant speed of $v \approx 10^6\,\mathrm{m/s}$. The densities of these "Dirac" quasiparticles can be controlled by external electric fields. Recently, using miniature gates, graphene *p-n* junctions (GPNJ) have been realized experimentally [28]. In such junctions the electron density $\rho(x)$ changes *gradually* between two limiting values, $\rho_1 < 0$ and $\rho_2 > 0$, as a function of position x. This change occurs over a lengthscale D determined by the device geometry. For a junction created near an edge of a wide gate (Fig. 2.1), D is of the order of the distance to this gate.

Besides opening the door for device applications, the study of transport through GPNJ may also test intriguing predictions of Klein tunneling [29, 30], Veselago lensing [31], microwave-induced [32] and Andreev [33] reflection. Klein tunneling in graphene is both similar and different from its counterpart for massive Dirac quasiparticles studied much earlier in semiconductor tunneling diodes. In such diodes the quasiparticle tunneling probability is given by [34] $T = \exp(-\pi\Delta^2/\, e\hbar v|F_{pn}|)$, where F_{pn} is the electric field in the gapped region (presumed to be uniform). The *single-particle* problem for a massless case is mathematically equivalent, except the

role of the gap Δ is played by $\hbar v k_y$. Integrating $T(k_y)$ over the transverse momentum k_y to get conductance and then inverting it, one finds the ballistic resistance R per unit width of the GPNJ to be [30]

$$R = (\pi/2)(h/e^2)\sqrt{\hbar v \,/\, e|F_{pn}|}\,. \tag{2.1}$$

Therefore, the absence of a finite energy gap prevents R from becoming exponentially large. This makes GPNJs orders of magnitude less resistive than tunneling diodes, in a qualitative agreement with experiment [28]. However quantitative accuracy of Eq. (2.1) is dubious because of many-body effects. The model of a uniform electric field, which is crucial for the validity of Eq. (2.1), is simply not correct in real graphene devices. First, the absence of a gap and second, the nonlinear nature of screening due to strong density gradients in a GPNJ invalidate such an approximation. Furthermore, since the massless electrons and holes can approach the p-n interface very closely, their coherent recombination takes place inside a "Dirac" strip of some characteristic width $x_{\rm TF}$ (Fig. 2.1) whose properties inherit the properties of the Dirac vacuum. Those can be profoundly affected by strong Coulomb interactions and presently remain not fully understood.

Below we show that a controlled analysis of this problem is nevertheless possible if one treats the dimensionless strength of Coulomb interactions $\alpha = e^2/\kappa_0\hbar v$ as a small parameter. Here κ_0 is the effective dielectric constant. Small α can be realized using HfO_2 and similar large-κ_0 substrates or simply liquid water, $\kappa_0 \sim 80$. For graphene on a conventional SiO_2 substrate, $\kappa_0 \approx 2.4$ and $\alpha \approx 0.9$. For such α we expect nonnegligible corrections to our analytic theory, perhaps, 25% or so.

Our main results are as follows. The electric field at the p-n interface is given by

$$e|F_{pn}| = 2.5\,\hbar v\,\alpha^{1/3}(\rho'_{\rm cl})^{2/3}\,, \tag{2.2}$$

where $\rho'_{\rm cl} > 0$ is the density gradient at the p-n interface computed according to classical electrostatics. Equation (2.2) implies that $e|F_{pn}|$ exceeds a naive estimate $e|F_{pn}| = \hbar v k_F(\rho_1)/\,D$, where $k_F = \sqrt{\pi|\rho|}$ is the Fermi wavevector, by a parametrically large factor $(\alpha k_F D)^{1/3} \gg 1$ (which in practice may approach ~ 10). The

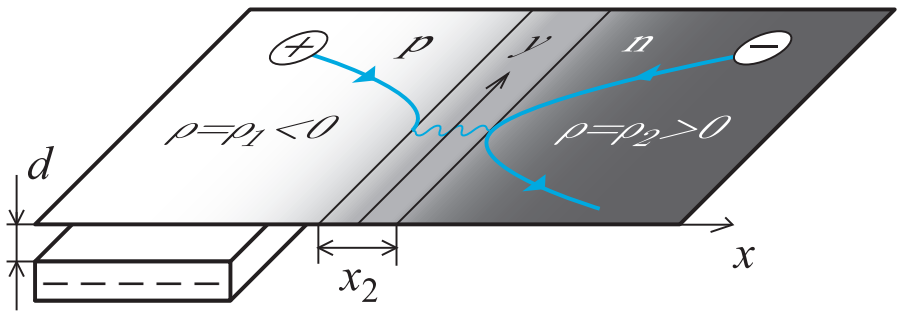

Figure 2.1: Device geometry. The semi-infinite gate on the left side (beneath the graphene sheet) controls the density drop $\rho_2 - \rho_1$ across the junction, while another infinite "backgate" above the sheet (not shown) fixes the density ρ_2 at far right. The smooth curves with the arrows depict typical ballistic trajectories of an electron ($-$) and a hole ($+$). The wavy curve symbolizes their recombination via quantum tunneling.

enhancement is caused by the lack of screening at this interface where the quasiparticle density is very small. As shown below, the calculation of F_{pn} requires going beyond the usual linear-response approach [35] to screening [36]. We demonstrate that Eq. (2.1) is rigorously valid if $\alpha \ll 1$, in which case it is legitimate to substitute F_{pn} from Eq. (2.2) in Eq. (2.1) to obtain[1]

$$R = (1.0 \pm 0.1)\,(h/e^2)\,\alpha^{-1/6}\,(\rho'_{\rm cl})^{-1/3}\,. \tag{2.3}$$

This value of R is parametrically larger than $(\pi/2)(h/e^2)\sqrt{k_F(\rho_1)/D}$ that one would obtain from Eq. (2.1) using the aforementioned naive estimate of $e|F_{pn}|^2$. This, however, only amplifies the result (considered paradoxical in the early days of quantum electrodynamics) that larger barriers are more transparent for Klein tunneling.

Note that Eq. (2.3) is universal. It is independent of the number, shape, or size of the external gates that control the profile of $\rho(x)$ far from the junction. It is instructive however to illustrate Eq. (2.3) on some example. Consider therefore a prototypical geometry depicted in Fig. 2.1. The voltage difference $-V_g$ between graphene and the semi-infinite gate with the edge at $x = x_g$ determines the total density drop $\rho_2 - \rho_1 = -\kappa_0 V_g/4\pi eD$. The density ρ_2 is assumed to be fixed by

[1]Disorder, unavoidable in real systems, may produce correction to this formula, see [37].

[2]These incorrect values of F and R could be inferred from Ref. [30] if D is incautiously identified with parameter d therein, as Fig. 1 of that paper indeed prompts one to do.

other means, e.g., a global "backgate" on the opposite side of the graphene sheet (not shown in Fig. 2.1). This model is a reasonable approximation to the available experimental setups [28]. An analytical expression for $\rho_{\rm cl}(x)$ follows from the solution of a textbook electrostatics problem, Eq. (10.2.51) of Ref. [38]. It predicts that function $\rho_{\rm cl}(x)$ crosses zero at the point $x_{pn} = x_g + (D/\pi)[1 + (|\rho_1|/\rho_2) + \ln(|\rho_1|/\rho_2)]$. Thus, for obvious physical reasons, the position x_{pn} of the p-n interface is gate-voltage dependent[3]. Taking the derivative of $\rho_{\rm cl}$ at $x = x_{pn}$ and substituting the result into Eq. (2.3), we obtain

$$R = \frac{0.7}{\alpha^{1/6}} \frac{h}{e^2} \left(1 - \frac{\rho_1}{\rho_2}\right)^{2/3} \left|\frac{D}{\rho_1}\right|^{1/3}, \quad |\rho_1| \gg \frac{1}{D^2}\,. \tag{2.4}$$

At fixed ρ_2, $R(\rho_1)$ has an asymmetric minimum at $\rho_1 = -\rho_2$. Away from this minimum, the more dramatic $R(\rho_1)$ dependence (of potential use in device applications) occurs at the $\rho_1 \to 0$ side where R diverges. The reason for this behavior of R is vanishing of the density gradient $\rho'_{\rm cl}(x)$ at far left (above the gate). Equation (2.4) becomes invalid at $|\rho_1| \lesssim 1/D^2$ where the gradual junction approximation breaks down. At this point $R \sim (h/e^2)D$.

Let us now turn to the derivation of the general formula (2.3). Our starting point is the basic principle of electrostatics, according to which we can replace the potential due to the external gates with that created by the fictitious in-plane charge density $\rho_{\rm cl}(x)$. Shifting the origin to $x = x_{pn}$, we have the expansion $\rho_{\rm cl}(x) \simeq \rho'_{\rm cl} x$ for $|x| \ll D$. The induced charge density $\rho(x)$ attempts to screen the external one to preserve charge neutrality; thus, a p-n interface forms at $x = 0$. We wish to compute the deviation from the perfect screening $\sigma(x) \equiv \rho_{\rm cl}(x) - \rho(x)$ caused by the quantum motion of the Dirac quasiparticles.

Thomas-Fermi domain.— Consider the region $|x| \gg x_s$,

$$x_s \equiv (1/\pi)(\alpha^2 \rho'_{\rm cl})^{-1/3}\,. \tag{2.5}$$

At such x the screening is still very effective, $|\sigma(x)| \ll |\rho_{\rm cl}(x)|$ because the local screening length $r_s(x)$ is smaller than the characteristic scale over which the

[3]One can manipulate x_{pn} by the backgate voltage, which shifts$\rho_{\rm cl}(x)$ by a constant affecting neither $\rho'_{\rm cl}(x)$ nor R.

background charge density $\rho_{\rm cl}(x)$ varies, in this case $\min\{|x|\,, D\}$. Indeed, the Thomas-Fermi (TF) screening length for graphene is [36] $r_s = (\kappa_0/\,2\pi e^2)(d\mu/\,d\rho) \sim 1/\,\alpha\sqrt{|\rho|}$, where μ is the chemical potential

$$\mu(\rho) = \mathrm{sign}(\rho)\sqrt{\pi}\hbar v|\rho|^{1/2} \tag{2.6}$$

appropriate for the two-dimensional Dirac spectrum. Substituting $\rho_{\rm cl}(x)$ for ρ, we obtain $r_s \sim |\alpha^2\rho'_{\rm cl}x|^{-1/2}$ at $|x| \ll D$. Therefore, at $|x| \gg x_s$ the condition $r_s \ll |x|$ that ensures the nearly perfect screening is satisfied.

The behavior of the screened potential $V(x)$ and the electric field $F(x) = -dV/\,dx$ at $|x| \gg x_s$ can now be easily calculated within the TF approximation,

$$\mu[\rho(x)] - eV(x) = 0\,. \tag{2.7}$$

It leads to the relation

$$eF(x) \simeq -\hbar v\sqrt{\pi/4}\,(\rho'_{\rm cl}/|x|)^{1/2}\,, \quad x_s \ll |x| \ll D\,, \tag{2.8}$$

which explicitly demonstrates the aforementioned enhancement of $|F(x)|$ near the junction. The TF approximation is valid if $k_F^{-1}(x) \ll \min\{|x|\,, D\}$. For $\alpha \sim 1$, this criterion is met if $|x| \gg x_s$. For $\alpha \ll 1$, the TF domain extends down to $|x| = x_{\rm TF} \sim \sqrt{\alpha}\,x_s$, see below.

A more formal derivation of the above results is as follows. From 2D electrostatics [38], we know that

$$\sigma(x) \equiv \rho_{\rm cl}(x) - \rho(x) = \frac{\kappa_0}{2\pi^2 e}\,\mathcal{P}\int \frac{dz}{z-x}F(z)\,. \tag{2.9}$$

Combined with Eqs. (2.6) and (2.7), this yields

$$\rho(x) - \rho'_{\rm cl}x = \sqrt{\rho'_{\rm cl}x_s^3}\;\mathcal{P}\int\limits_0^\infty \frac{xdz}{z^2-x^2}\frac{d}{dz}\sqrt{|\rho(z)|}\,. \tag{2.10}$$

Here the upper integration limit was extended to infinity, which is legitimate if $D \gg x_s$. The solution for $\rho(x)$ can now be developed as a series expansion in $1/x$. The leading correction to the perfect screening is obtained by substituting $\rho(x) = \rho'_{\rm cl}x$ into the integral, yielding $\sigma(x)/\rho(x) \simeq (\pi/4)\,|x_s/x|^{3/2}$. In accord with

the arguments above, this correction is small at $|x| \gg x_s$. Furthermore, it falls off sufficiently fast with x to ensure that to the order $\mathcal{O}(x_s/D)$ the results for $V(x)$ and $\rho(x)$ at the origin are insensitive to the large-x behavior. In the opposite limit, $|x| \ll x_s$, one can show that

$$\rho_{\rm TF}(x) \simeq c^2 \rho'_{\rm cl} \frac{x^2}{x_s}\,, \quad e|F_{\rm TF}| \simeq c\pi\hbar v\, \alpha^{1/3} (\rho'_{\rm cl})^{2/3}\,, \tag{2.11}$$

where $c \sim 1$ is a numerical coefficient. (The subscripts serve as a reminder that these results are obtained within the TF approximation.)

Unsuccessful in finding c analytically, we turned to numerical simulations. To this end we reformulated the problem as the minimization of the TF energy functional

$$E[V(x)] = E_0 + \int eV(x) \left[\frac{1}{2}\sigma(x) - \rho_{\rm cl}(x)\right] dx\,, \tag{2.12}$$

$$E_0 = \frac{e^3}{3\pi\hbar^2 v^2} \int |V(x)|^3 dx\,, \tag{2.13}$$

where $\sigma(x)$ is defined by Eq. (2.9). The convolution integral in that equation was implemented by means of a discrete Fourier transform (FT) over a finite interval $-D \le x < D$. Similarly, the integral in Eq. (2.12) was implemented as a discrete sum. Since the FT effectively imposes the periodic boundary conditions on the system, we chose the background charge density in the form

$$\rho_{\rm cl}(x) = \rho_0 \sin(\pi x/D)\,, \tag{2.14}$$

so that the p-n interfaces occur at all $x = nD$, where n is an integer. Starting from the initial guess $\sigma \equiv 0$, the solution for $\rho(x)$ and $V(x)$ within a unit cell $-D \le x < D$ was found by a standard iterative algorithm[4]. As shown in Fig. 2.2, at large x the TF density profile is close to Eq. (2.14). At small x, it is consistent with Eq. (2.11) using $c = 0.8 \pm 0.05$, cf. Fig. 2.4.

Dirac domain.— Let us now discuss the immediate vicinity of the p-n interface, $|x| < x_{\rm TF} \sim \sqrt{\alpha}\, x_s$ (the precise definition of $x_{\rm TF}$ is given below). At such x the TF approximation is invalid and instead we have to use the true quasiparticle wavefunctions to compute ρ and V. For a gradual junction the two inequivalent

[4]Function `fminunc` of MATLAB, ©MathWorks, Inc.

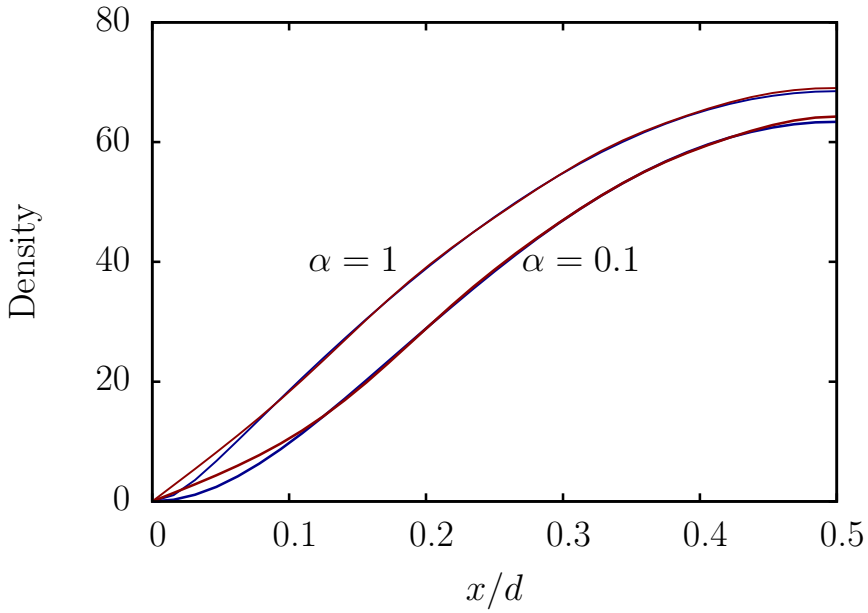

Figure 2.2: Electron density in units of $4/D^2$ for $\alpha = 1$, $\rho_0 = 75$ and $\alpha = 0.1$, $\rho_0 = 100$. Thicker blue curves are from minimizing the TF functional, Eqs. (2.12)–(2.14); thinner red lines are from replacing E_0 in this functional by the ground-state energy of Hamiltonian (2.15). The p-n interface is at $x = 0$.

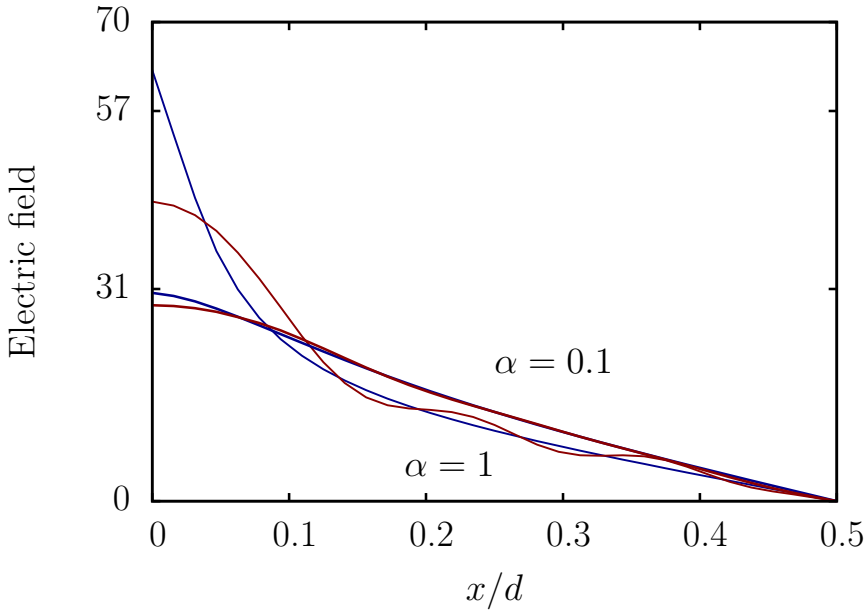

Figure 2.3: Magnitude of the electric field in units of $4\hbar v/eD^2$ for the same parameters. Numerical values "34" and "60" are the predictions of Eq. (2.2) for the nearby TF (thick blue) curves.

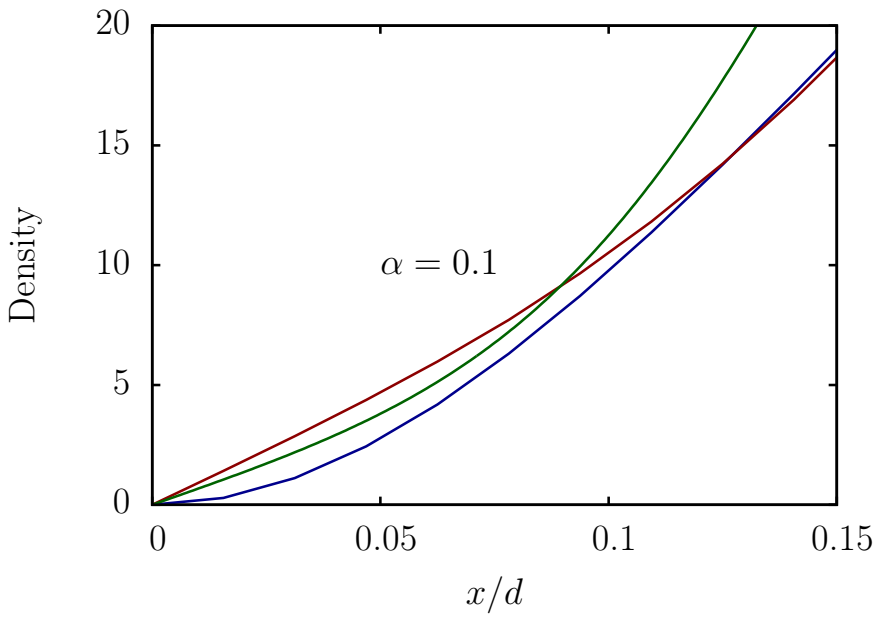

Figure 2.4: Enlarged view of the $\alpha = 0.1$ data from Fig. 2.2 and the numerically evaluated Eq. (2.17).

Dirac points ("valleys") of graphene [5] are decoupled and the wavefunctions can be chosen to be two-component spinors $\exp(ik_y y)\,[\psi_1(x)\ \psi_2(x)]^T$ (their two elements represent the amplitudes of the wavefunction on the two sublattices of graphene). Here we already took advantage of the translational invariance in the y-direction and introduced the conserved momentum k_y. The effective Hamiltonian we need to diagonalize has the Dirac form

$$H = \hbar v(-i\tau_1\partial_x + \tau_2 k_y) - eV(x)\,, \tag{2.15}$$

where τ_1 and τ_2 are the Pauli matrices. At the end of the calculation we will need to multiply the results for $\rho(x)$ by the total spin-valley degeneracy factor $g = 4$.

The solution of this problem can be obtained analytically under the condition $\alpha \ll 1$. This is possible ultimately because for such α the electric field is nearly uniform, $|F_{pn} - F(x)| \ll |F_{pn}|$, inside the strip $|x| \ll x_s$. The reason is this strip in almost empty of charge. Let us elaborate. Since the potential $V(x)$ is small near the interface and the spectrum is gapless, $\rho(x)$ must be smooth and have a regular Taylor expansion at $x \to 0$,

$$\rho(x) = a_1 x + a_3 x^3 + \ldots \tag{2.16}$$

Requiring the leading term to match with the TF Eq. (2.11) at the common boundary $x = x_{\rm TF} \sim \sqrt{\alpha}\, x_s$ of their validity, we get $a_1 \sim \sqrt{\alpha}\, \rho'_{\rm cl}$. This means that the net charge per unit length of the interface on the n-side of the junction is somewhat smaller than the TF approximation predicts, by the amount of $\Delta Q = e \int_0^\infty [\rho(x) - \rho_{\rm TF}(x)] dx \sim \sqrt{\alpha} \rho'_{\rm cl} x_{\rm TF}^2$. In turn, the true $|F_{pn}|$ is lower than $|F_{\rm TF}|$ by $\sim \Delta Q / \kappa_0 x_{\rm TF}$. nowever for $\alpha \ll 1$ this is only a small, $\mathcal{O}(\alpha)$ relative correction.

As soon the legitimacy of the linearization $V(x) \simeq -F_{pn} x$ is established, wavefunctions ψ_1 and ψ_2 for arbitraty energy ϵ are readily found. Since ϵ enters the Dirac equation only in the combination $-eV(x) - \epsilon = eF_{pn}(x - x_\epsilon)$, the energy-$\epsilon$ eigenfunctions are the $\epsilon = 0$ eigenfunctions shifted by $x_\epsilon \equiv \epsilon/(eF_{pn})$ in x. In turn, these are known from the literature: they are expressed in terms of confluent hypergeometric functions $\Phi(a; b; z)$ [39]. These solutions were rediscovered multiple times in the past, both in solid-state and in particle physics. The earliest instance known to us is Ref. [34]; the latest examples are Refs. [30] and [40]. The sought electron density $\rho(x)$ can now be obtained by a straightforward summation over the occupied states ($\epsilon \leq 0$), which leads us to[5]

$$\rho = \frac{g}{x_{\rm TF}^2} \int \frac{dk_y}{2\pi} \int_0^x \frac{dz}{\pi e^{2\pi\nu}} \left[\left| \Phi\left(i\nu; \frac{1}{2}; -\frac{iz^2}{x_{\rm TF}^2} \right) \right|^2 - \frac{1}{2} \right] , \tag{2.17}$$

where $\nu = k_y^2 x_{\rm TF}^2/4$ and $x_{\rm TF} \equiv \sqrt{\hbar v / |F_{pn}|} \sim \sqrt{\alpha}\, x_s$. This formula is fully consistent with Eq. (2.16): the Taylor expansion of the integrand yields, after a simple algebra, $a_1 = g/(\sqrt{2}\pi^2 x_{\rm TF}^3)$, $a_3 = g\sqrt{2}/(3\pi^3 x_{\rm TF}^5)$, *etc.* Using the known integral representations of the function Φ [39], one can also deduce the behavior of $\rho(x)$ at $x \gg x_{\rm TF}$. The leading term is precisely the TF result $\rho_{\rm TF}(x) = g x^2 / 4\pi x_{\rm TF}^4$. Therefore, Eq. (2.17) seamlessly connects to Eq. (2.11) at $x \sim x_s$. (At such x corrections to $\rho_{\rm TF}(x)$, including Friedel-type oscillations[6], are suppressed by extra powers of parameter α.) We conclude that for $\alpha \ll 1$ we have obtained the complete and rigorous solution for $\rho(x)$, $V(x)$, and F_{pn} [Eq. (2.2)], in particular. As discussed

[5] A similar expression was derived in Ref. [40] in the context of carbon nanotube p-n junctions. The only difference is that no integration over k_y is present there.

[6] The undulations of $F(x)$ seen on the $\alpha = 1$ curves in Fig. 2.3 may be the aforementioned Friedel oscillations but we cannot exclude numerical artifacts either.

in the beginning, it immediately justifies the validity of Eq. (2.1) and leads to our result for the ballistic resistance, Eq. (2.3). However, in current experiments $\alpha \sim 1$ and in the remainder of this Letter we offer a preliminary discussion of what can be expected there.

Since it is the strip $|x| < x_{\rm TF}$ that controls the ballistic transport across the junction [30], the constancy of the electric field in this strip is crucial for the accuracy of Eq. (2.1). This is assured if $\alpha \ll 1$ but at $\alpha \sim 1$ the buffer zone between $x_{\rm TF}$ and x_s vanishes, and so we expect $F(x_{\rm TF})$ and $F(0) = F_{pn}$ to differ by some numerical factor.

To investigate this question we again turned to numerical simulations. We implemented a lattice version of the Dirac Hamiltonian by replacing $-i\partial_x$ in Eq. (2.15) with a finite difference on a uniform grid. We also replaced E_0 in Eq. (2.13) by the ground-state energy of H, taken with the negative sign: $E_0 = -L_y^{-1} \sum_j \epsilon_j / \left[1 + \exp(\beta\epsilon_j)\right]$. Here ϵ_j are the eigenvalues of H (computed numerically) and the β is a computational parameter (typically, four orders of magnitude larger than $1/\max e|V|$). We have minimized thus modified functional E by the same algorithm[7], which produced the results shown in Fig. 2.2-2.4. As one can see, for $\alpha = 0.1$ the agreement between analytical theory and simulations is very good. However for $\alpha = 1$ we find that $|F_{pn}|$ is approximately 25% smaller than given by Eq. (2.2). Note also that for $\alpha = 1$ the electric field is noticeably nonuniform near the junction, in agreement with the above discussion . Therefore, Eq. (2.1) should also acquire some corrections. In principle, we could compute numerically the transmission coefficients $T(k_y)$ for this more complicated profile of $F(x)$. However this would not be the ultimate answer to this problem. Indeed, at $\alpha \sim 1$ electron interactions are not weak, and so exchange and correlation effects are likely to produce further corrections to the self-consistent single-particle scheme we employed thus far, which may be quite nontrivial inside the Dirac strip $|x| < x_{\rm TF}$. We leave this issue for future investigation.

[7]Function `fminunc` of MATLAB, ©MathWorks, Inc.

2.1 Acknowledgements

Chapter 2, almost in full, is a reprint of the materials as it appears in L. M. Zhang and M. M. Fogler. Nonlinear screening and ballistic transport in a graphene p-n junction. *Phys. Rev. Lett.*, 100(11):116804, 2008. The dissertation author was the primary investigator and author of this paper.

Chapter 3

Electronic structure of bilayer graphene from infrared spectroscopy

3.1 Introduction

As discussed in the introduction chapter, graphene is the basic building block of other types of carbon materials. Indeed, the first calculation of its band structure by Wallace [8] was motivated by his studies of graphite. Extending that work, Slonczewski and Weiss, [10] McClure, [9, 10] and others [41] have developed the now commonly used Slonczewski-Weiss-McClure (SWMc) model for the low-energy electron properties of graphite. This model, which is equivalent to a tight-binding model with seven parameters, [42] has proven to be a very useful analytical tool. It permitted theoretical calculations of a vast number of properties of graphite, including its diamagnetic susceptibility, de Haas-van Alfven effect, magnetooptical response, cyclotron resonance, and so on. These properties were actively studied experimentally until the late 70's and lead to accurate estimates of the principal SWMc parameters, γ_0 through γ_3. Still, it proved challenging to unambiguously determine the remaining three SWMc constants γ_4, γ_5, and Δ, which are measured in tens of meV. For illustration, in Table 3.1 we list inequivalent pa-

rameter sets from the latest original sources, Refs. [43] (reprinted as Ref. [44]) and [15]. Subsequently, the issue was further confounded by numerous misprints in reference books and reviews [1]. The density-functional theory calculations, [48, 17, 49] which normally have accuracy of $\sim 0.1\,\mathrm{eV}$ for quasiparticle dispersion, have not yet settled this discrepancy.

In view of the reinvigorated interest to graphene, it has become an important question to obtain the SWMc constants for a few layer graphene and also to compare them with those for bulk graphite. Thus, some difference between the graphite and a graphene bilayer was recently reported, based on the analysis of Raman scattering. [45] Several *ab initio* calculations of these parameters for the bilayer have also been done. [50, 51, 52, 53, 54] Unfortunately, they have not explicitly discussed the less accurately known SWMc parameters.

The bilayer is a system intermediate between graphene and bulk graphite. Its lattice structure (for the case of the Bernal or AB stacking) is illustrated in Fig. 3.1(a). The corresponding band structure, [26, 56, 27] shown in Fig. 3.1(b), consists of four bands. These bands arise from splitting and hybridization of the Dirac cones of the individual layers by the interlayer hopping matrix element γ_1 and by the electrostatic potential difference $V_\mathrm{b} = 2U$ between the two layers. [26, 57] The latter can be controlled experimentally by varying the voltage V_g of a nearby metallic gate [58, 59] or by doping. [60] This degree of tunability makes the bilayer graphene an extremely interesting material for both fundamental study and applications.

In this paper we show that γ_1, $v_4 \equiv \gamma_4/\gamma_0$, and Δ can be *directly* extracted from the dynamical conductivity measured in zero magnetic field. This is in contrast to the bulk graphite where determination of the SWMc constants was never straightforward and almost invariably required the use of strong magnetic fields.

The dynamical conductivity $\sigma(\Omega)$ is determined by the six possible transitions among the four bands, see Fig. 3.1(c). They have energies of the order

[1] For example, in the often cited [27, 45] book of Brandt *et al.* [16] the sign of Δ is shown as positive whereas the original source [46, 44] is very clear on it being negative. Another recent review [47], which is otherwise fairly up-to-date, chose nevertheless to cite an early [14] (later revised [44]) parameter determination from the MIT group.

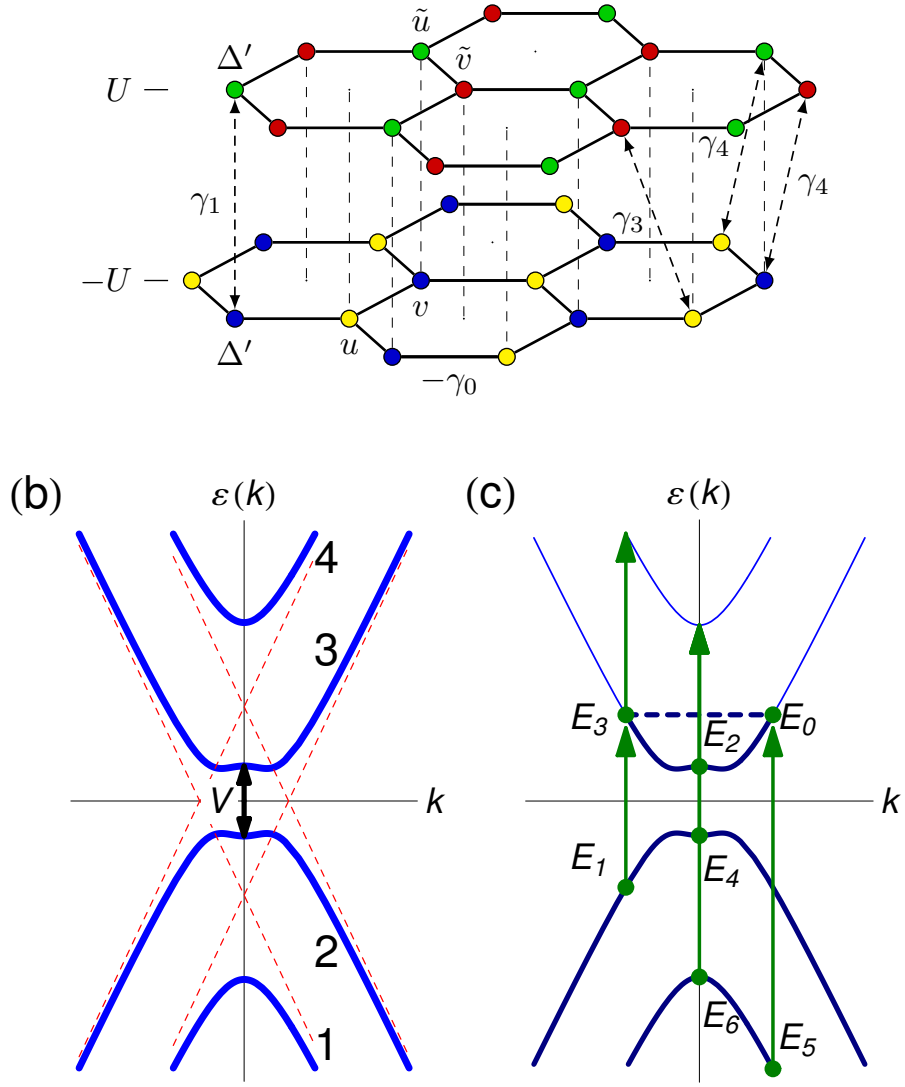

Figure 3.1: (a) Crystal structure of the graphene bilayer with the relevant SWMc hopping parameters shown. (b) Band structure of a biased bilayer (lines), which can be considered as hybridization of two shifted Dirac cones (dots). Numbers on the right label the four bands. (c) Examples of the allowed optical transitions for the chemical potential indicated by the dashed line. Occupied states are shown by the thicker lines. The dots and the arrows mark the initial and the final states, respectively, of the transitions that produce features at frequencies E_j, $j = 1, 2, \ldots, 6$ in Fig. 3.2(a) below. E_0 is the intraband transition (Drude peak).

Table 3.1: The SWMc parameters (in eV) according to previous and present work. The numbers in parentheses are the reported accuracy of the trailing decimals. The "Exp" and "DFT" stand for experiment and density functional theory, respectively.

SWMc	Graphene bilayer			Graphite, early work				Graphite, recent work	
parameter	Pres. work	Exp[2]	DFT[3]	Exp[4]	Exp[5]	DFT[6]	DFT[7]	Exp[8]	DFT[9]
γ_0	3.0[10]	2.9	2.6	3.16(5)	3.11	2.92	2.598(15)		
γ_1	0.40(1)	0.30	0.3	0.39(1)	0.392	0.27	0.364(20)		
γ_2	0.0[11]	0.0[11]	0.0[11]	-0.020(2)	-0.0201	-0.022	-0.014(8)		
γ_3	0.3[10]	0.10	0.3	0.315(15)	0.29	0.15	0.319(20)		
γ_4	0.15(4)	0.12		0.044(24)	0.124	0.10	0.177(25)		
γ_5	0.0[11]	0.0[11]	0.0[11]	0.038(5)	0.0234	0.0063	0.036(13)		
Δ	0.018(3)		0.01[12]	-0.008(2)	-0.0049	0.0079	-0.026(10)	<0.01[13]	-0.037[14]
$\Delta' = \Delta - \gamma_2 + \gamma_5$	0.018(3)		0.01[12]	0.037(5)	0.0386	0.0362	0.024(18)		

[2] [45]
[3] [53]
[4] [44]
[5] [15]
[6] [48]
[7] [17]
[8] [55]
[9] [49]
[10] This value cannot be very accurately found from our analysis and is instead adopted from the literature.
[11] Physically irrelevant in the bilayer but should be set to zero for calculating Δ' from Δ.
[12] Our estimate based on digitizing band dispersion graphs published in Refs. [53, 51, 52, 54].
[13] Absolute value only.
[14] The negative sign (omitted in Ref. [49]) is required for consistency with the conventional definition [9] of Δ.

of a few 10^{-1} eV, which is in the infrared optical range. Recently, experimental measurements of the infrared response of the bilayers have been carried out by our [61] and other [62, 63] groups. Below we identify and explain the key findings of these experiments based on how different combinations of the interband transitions are either activated or suppressed by the Pauli exclusion principle. Our theory enables us to reach a quantitative agreement with the experiment using SWMc γ_0, γ_1, γ_4, and Δ, and also the phenomenological broadening constant Γ as adjustable parameters. The values of the SWMc parameters that give the best fit are given in the second column of Table 3.1. Note that the next-nearest layer hopping parameters γ_2 and γ_5 are irrelevant for the bilayer. The parameter γ_3 cannot be reliably estimated from these particular experiments because it has an effect similar to the simple broadening (Γ) in the range of carrier concentrations suitable for our analysis.

Previous theoretical studies of the optical conductivity of bilayer graphene [56, 64, 27, 65, 66] used a simplified model in which only γ_0 and γ_1 were taken into account. This model successfully explains the major features of $\sigma(\Omega)$ as well as its dependence on the gate voltage $V_{\rm g}$, and we qualitatively summarize it as follows. Conduction and valence bands are symmetric. In the absence of the electrostatic potential difference $V_{\rm b}$ between the layers the two conduction (valence) bands have the same shape and are shifted by γ_1. Except the range of very small momenta k, their shape remain nearly identical even in the presence of a finite $V_{\rm b}$. As a result, there is a high optical density of states for transitions between the two pairs of bands at frequency $\gamma_1/\hbar$, which gives rise to a sharp peak in the real part of the conductivity $\mathrm{Re}\,\sigma(\Omega)$ at $\Omega = \gamma_1/\hbar \approx 3200\,\mathrm{cm}^{-1}$ (using $\gamma_1 = 0.40\,\mathrm{eV}$). Other transitions give more gradually varying contributions to $\mathrm{Re}\,\sigma(\Omega)$, eventually leading to the asymptotic "universal" value [67, 56, 64, 27, 65, 66, 68] $\sigma = e^2/2\hbar$ at high frequency (which is twice the value for the monolayer [69]). Finally, in real graphene systems the conductivity features are never sharp because of a finite lifetime due to, e.g., disorder scattering. This broadens the peaks and can also merge together several features that are close in energy, see Fig. 3.2.

Our recent infrared experiments [61] as well as measurements by another

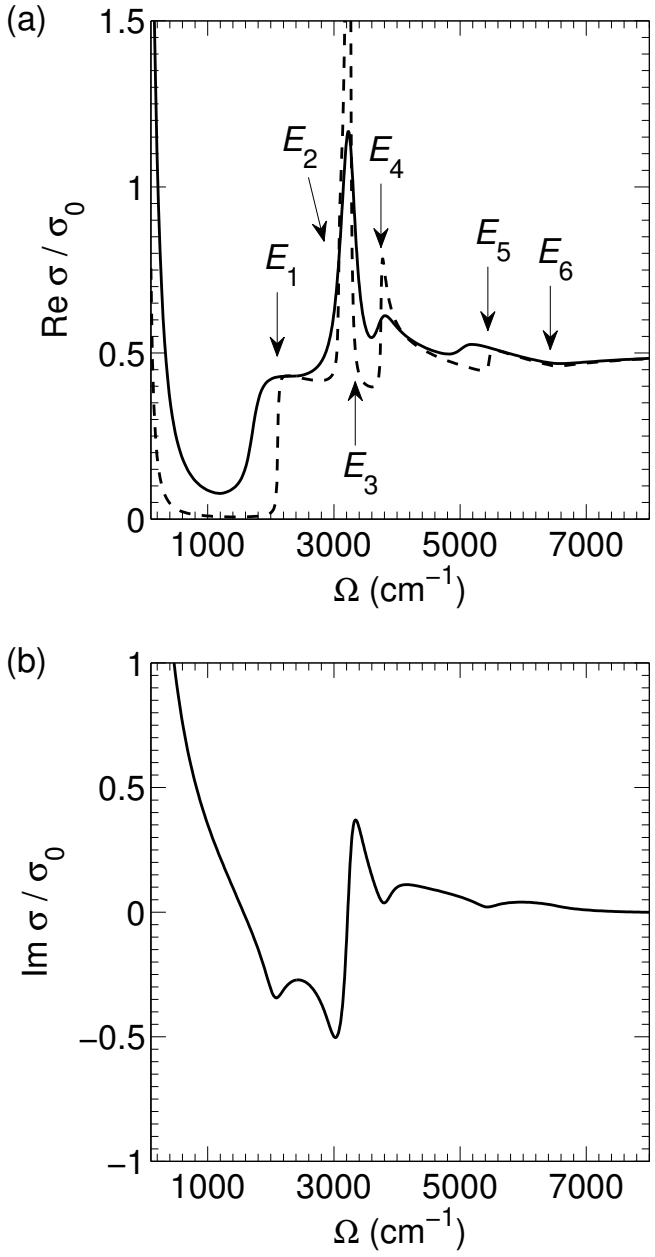

Figure 3.2: (a) Real and (b) imaginary part of conductivity in units of $\sigma_0 = e^2/\hbar$ for the gate voltage $\delta V = -100\,\mathrm{V}$. The solid curves are for broadening $\Gamma = 0.02\gamma_1$. The dashed curve is for $\Gamma = 0.002\gamma_1$.

group [63] have largely confirmed this picture but also found features that cannot be explained within this simple model. In particular, the conductivity peaks on the electron and the hole sides are displaced in energy from γ_1 by about 10% in opposite directions. [Electron and hole doping is identified with, respectively, positive and negative $\delta V = V_{\rm g} - V_{\rm CN}$, where $V_{\rm CN}$ is the gate voltage at which the bilayer is tuned to the charge-neutrality (CN) point.]

In order to investigate the origin of these features in this paper we carry out a combined experimental-theoretical study of the infrared response of a bilayer graphene. We attribute the observed electron-hole asymmetry to the effect of γ_4 and Δ. We find that including these parameters is essential for a more accurate discussion of $\sigma(\Omega)$ of the bilayer. Besides differences in the optical response, γ_4 and Δ also make effective masses for electrons and holes unequal [15], in agreement with the findings from the Raman scattering. [45]

In our experiments, we have measured the optical reflection $R(\Omega, V_{\rm g})$ and transmission $T(\Omega, V_{\rm g})$ as a function of the frequency Ω and the gate voltage $V_{\rm g}$. From R and T we extracted the real and imaginary part of the conductivity using a commercial software package. Some of these experimental results were reported previously. [61]

In this paper we present more extensive experimental data and we also compute the same three quantities — σ, R, and T — theoretically. The calculation requires accounting for the interplay of several physical phenomena: (a) electrostatic charging of the layers (b) their dynamical conductivity, (c) disorder, and (d) the optical properties of the environment (sample, substrate, and the gate). Each of these ingredients has been studied in the past. [70, 56, 64, 27, 65, 66, 58, 71] Here we carry out all these calculations in a single paper albeit we include disorder broadening in a very simple way. This enables us to directly compare our theoretical results with the measurements.

The remainder of the paper is organized as follows. In Sec. 3.2 we summarize our results. Theoretical derivation is outlined in Sec. 3.3. Section 3.4 contains

[15] Another important source for the effective mass asymmetry is the in-plane next-nearest neighbor hopping [8] $\gamma_0' \sim 0.1\gamma_1$. However, it does not change the optical transition energies, and so has virtually no effect on $\sigma(\Omega)$.

comparison of the theory and experiment, discussion, and conclusions. Some calculational details are relegated to the Appendix.

3.2 Results

To measure the optical response of the bilayer we employed synchrotron infrared radiation, as described previously. [72, 61] Understandably, the two-atom thick sample has a rather small optical signal. The quantity which can be extracted most reliably from the current experiments is the relative transmission $T(\Omega, V_{\rm g})/T(\Omega, V_{\rm CN})$ and reflection $R(\Omega, V_{\rm g})/R(\Omega, V_{\rm CN})$. All measurements were done at the temperature of 45 K. The data for the largest $|\delta V| = |V_{\rm g} - V_{\rm CN}|$ are depicted in Fig. 3.3. The main feature in the relative transmission spectra is a small but clearly visible dip around $\Omega = 3200\,{\rm cm}^{-1}$. Away from the dip, the relative transmission is slightly higher than unity. The relative reflection spectra are characterized by a dip-peak structure. Transmission and reflection spectra are asymmetric between positive and negative δV, which correspond, respectively, to doping of electrons and holes in bilayer graphene.

From the transmission and reflection data, we extracted the optical conductivity. [73, 72, 61] The dominant feature in the conductivity spectra is a strong peak at $\Omega \approx 3200\,{\rm cm}^{-1}$, see Fig. 3.4(c). Below the main peak, we observed a broadened threshold feature, which shifts systematically with δV. The most intriguing observation is again the electron-hole asymmetry in the optical conductivity. For instance, the frequencies of the main peak in ${\rm Re}\,\sigma(\Omega)$ and its voltage dependence are noticeably different for electrons and holes, see Fig. 3.4(c). Also, while the peak is quite symmetric at large positive voltages, at high negative δV, it is not. The most probable reason is the existence of a secondary peak at a slightly larger Ω, see below.

On the theory side, we calculated σ, T, and R, using the SWMc constants and Γ as adjustable parameters. Results for the conductivity are shown in Fig. 3.4(b). The reflection and transmission are plotted in Fig. 3.3. The calculational parameters were adjusted to reproduce the frequency positions and widths

of the main features of the experimental data. Interestingly, in this way of fitting, it was not possible to achieve an equally good agreement for the vertical scale of the observed features. Still their qualitative trend as a function of δV is reproduced well.

Both in experiment and in calculations the carrier concentrations are always smaller than the characteristic value n_0 given by

$$n_0 = \frac{\gamma_1^2}{\hbar^2 v^2} = 3.7 \times 10^{13}\,\mathrm{cm}^{-2}\,. \tag{3.1}$$

Here and below we assume that $\gamma_0 = 3.0\,\mathrm{eV}$, which corresponds to $v = (3/2)\gamma_0 a/\hbar = 1.0 \times 10^8\,\mathrm{cm}/s$. (Based on other results in the literature, this value should be accurate to about 10%.) At concentrations $|n| < n_0$ the high energy bands 1 and 4 have no free carriers and $\mathrm{Re}\,\sigma(\Omega)$ has a pronounced peak at $\Omega \approx 3200\,\mathrm{cm}^{-1}$. As explained above, this feature corresponds to transition between band pairs that are nearly parallel: bands 3 and 4 for $\mu > 0$ or bands 1 and 2 for $\mu < 0$, see Fig. 3.1.

The evolution of the infrared response with V_g can be understood as follows. As the gate voltage deviates further away from V_CN, the electron concentration

$$n = C_b \delta V / e \tag{3.2}$$

and the chemical potential μ increase by the absolute value. Here C_b is the capacitance between the bilayer and the gate. As a result of an increased $|n|$, the peak become more pronounced. Simultaneously, near the higher frequency side of the peak a depletion of conductivity develops. One can say that the optical weight is increasingly transfered from the high frequencies to the γ_1 peak. Larger conductivity is directly associated with decreased optical transmission. Therefore one observes an increasing dip in the transmission near γ_1 and a higher transmission at higher Ω, see Fig. 3.3. Similar features appear in the reflection but they are more difficult to interpret as they are also affected by $\mathrm{Im}\,\sigma(\Omega)$.

Very important for our analysis are the aforementioned small shifts in the position of the γ_1 peak as a function of δV. Within the SWMc model, their origin is as follows. In the absence of broadening, the peak arises from the absorption in the range of frequencies, $E_2 < \hbar\Omega < E_3$, see Figs. 3.1 and 3.2. Since the optical weight at E_3 is higher, the conductivity peak occurs at energy E_3. However, if the

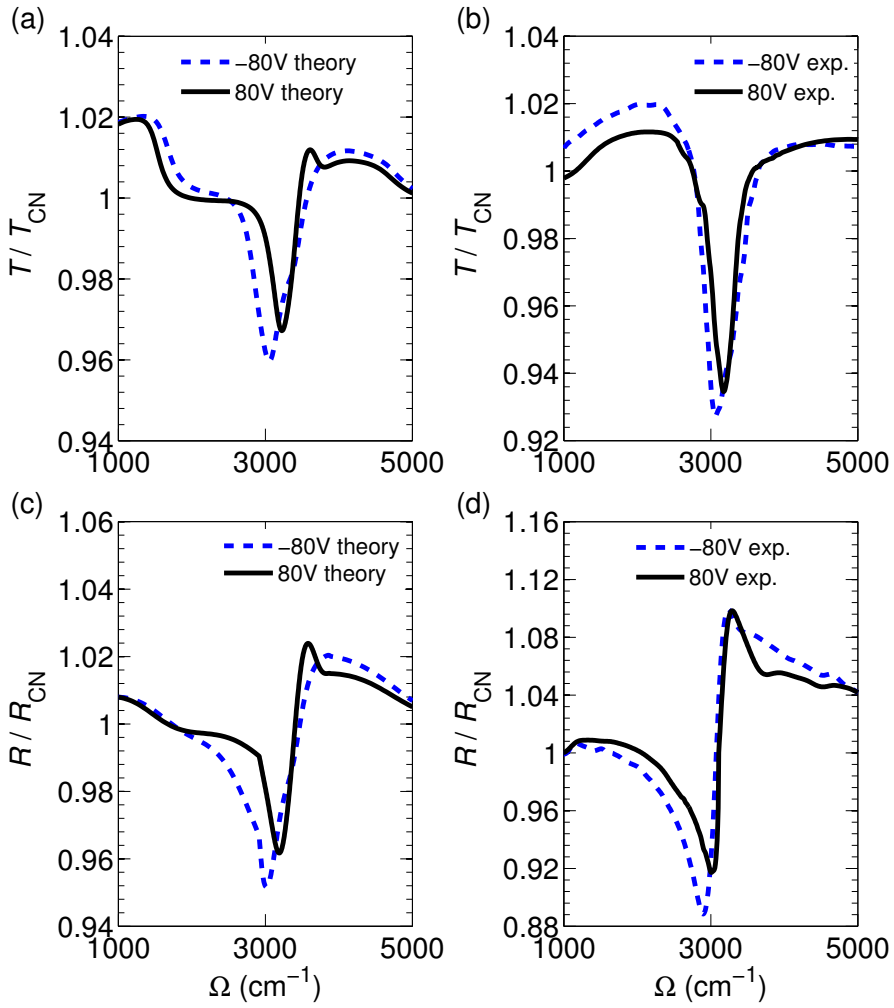

Figure 3.3: Relative transmission: (a) theory (b) experiment. Relative reflection: (c) theory (d) experiment. The solid line is for electrons, $\delta V \approx +80\,\mathrm{V}$. The dashed line is for holes, $\delta V \approx -80\,\mathrm{V}$. The experimental uncertainties are ~ 0.002 (0.2%) at Ω near $3000\,\mathrm{cm}^{-1}$ and $\sim 0.5\%$ at high frequency.

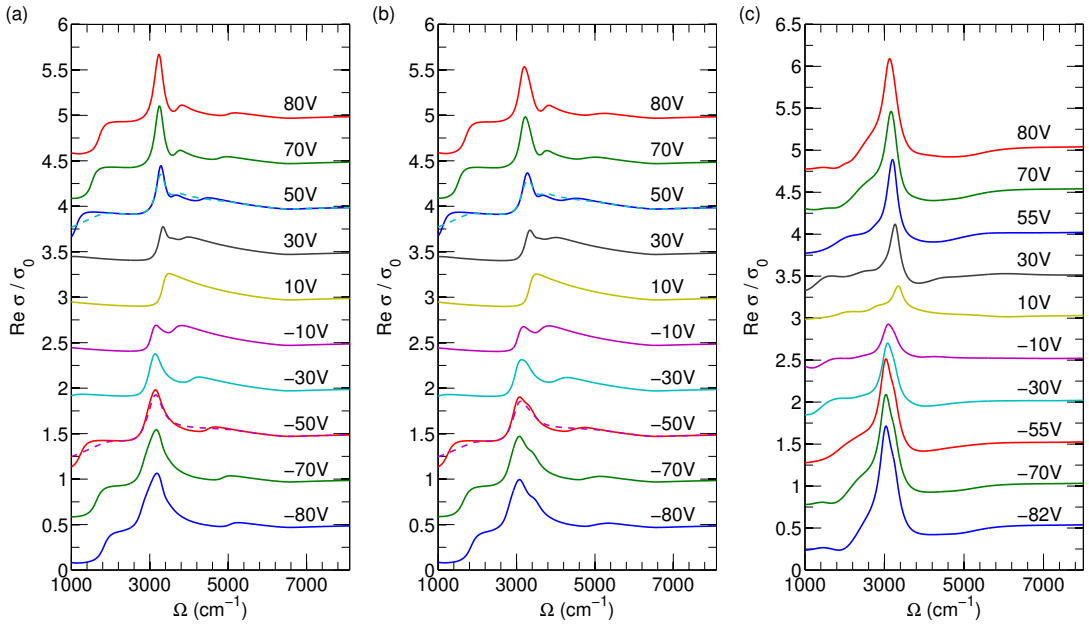

Figure 3.4: (a), (b) Theoretical and (c) experimental results for the conductivity $\mathrm{Re}\,\sigma$, in units of $\sigma_0 = 4e^2/\hbar$, as a function of frequency Ω. The deviation δV of the gate voltage from the charge neutrality point is indicated next to each curve. For clarity, the curves are offset vertically by $0.5\sigma_0$ from one another. The SWMc parameters for plot (b) are given in Table 3.1. In (a) they are the same, except γ_3 is set to zero. The dashed curves superimposed on the $\delta V = +50\,\mathrm{V}$ $(-50\,\mathrm{V})$ traces in (a) and (b) are the arithmetic means of all the positive (negative) δV curves. Their significance is discussed in Sec. 3.4. The estimated uncertainty of the measured $\mathrm{Re}\,\sigma$ is $0.125\sigma_0$ at $\Omega \sim 8000\,\mathrm{cm}^{-1}$ and $0.0625\sigma_0$ at $\Omega \sim 3000\,\mathrm{cm}^{-1}$.

broadening is large enough, the optical weight becomes distributed more uniformly, and the peak position moves to the midpoint of E_2 and E_3, see Fig. 3.5. Energies E_2 and E_3 themselves vary with the gate voltage (or n). For positive δV (positive n), $E_2 \equiv E_2^+$ is the energy difference between the bands 3 and 4 at $k = 0$. The energy $E_3 \equiv E_3^+$ is the corresponding difference at $k = k_F$, where

$$k_F = \mathrm{sign}\,(n)\sqrt{\pi|n|} \tag{3.3}$$

is the Fermi momentum. For $\delta V < 0$ we denote E_2 and E_3 by, respectively, E_2^- and E_3^- and they are computed using the bands 1 and 2 instead of 3 and 4.

From the band structure, [56, 27] we can find the following approximate expressions valid for $n \ll n_0$:

$$E_2^{\pm} \simeq \gamma_1 - \frac{V_\mathrm{b}}{2} \pm \Delta\,, \tag{3.4}$$

$$E_3^{\pm} \simeq \gamma_1\sqrt{1 + \frac{2\pi|n|}{n_0}} - \sqrt{\frac{{V_\mathrm{b}}^2}{4} + \left(\frac{\pi\gamma_1 n}{n_0}\right)^2} \pm \Delta \mp 2\,(2v_4\gamma_1 + \Delta)\,\frac{\pi|n|}{n_0}\,. \tag{3.5}$$

Here $V_\mathrm{b} = V_\mathrm{b}(n)$ as well as the chemical potential $\mu = \mu(n)$ are determined self-consistently by the electrostatics of the system, [70] see Sec. 3.3. These equations indicate that the parameters primarily responsible for electron-hole asymmetry are γ_4 and Δ.

Parameter Δ is the difference of the on-site electron energies of the A and the B sites [41, 42] [the stacked and unstacked sublattices, respectively, see Fig. 3.1(a)]. It has two effects: first, it lifts the $k = 0$ energy for bands 1 and 4; second, it adds a k dependent perturbation to the two band dispersion. Parameter $v_4 = v\gamma_4/\gamma_0$ of dimension of velocity characterizes hopping between a stacked atom and its the three unstacked neighbors of its stacking partner. It also introduces difference between the valence and conduction bands. To the leading order in k, this hopping shifts the two middle bands (2 and 3) upward by a term proportional to v_4k^2 and shifts the two outer bands (1 and 4) downward by the same amount. These effects of Δ and v_4 are illustrated in Fig. 3.6.

Additional electron-hole asymmetry can in principle come from extrinsic sources, e.g., charged impurities that can be present on or between the layers.

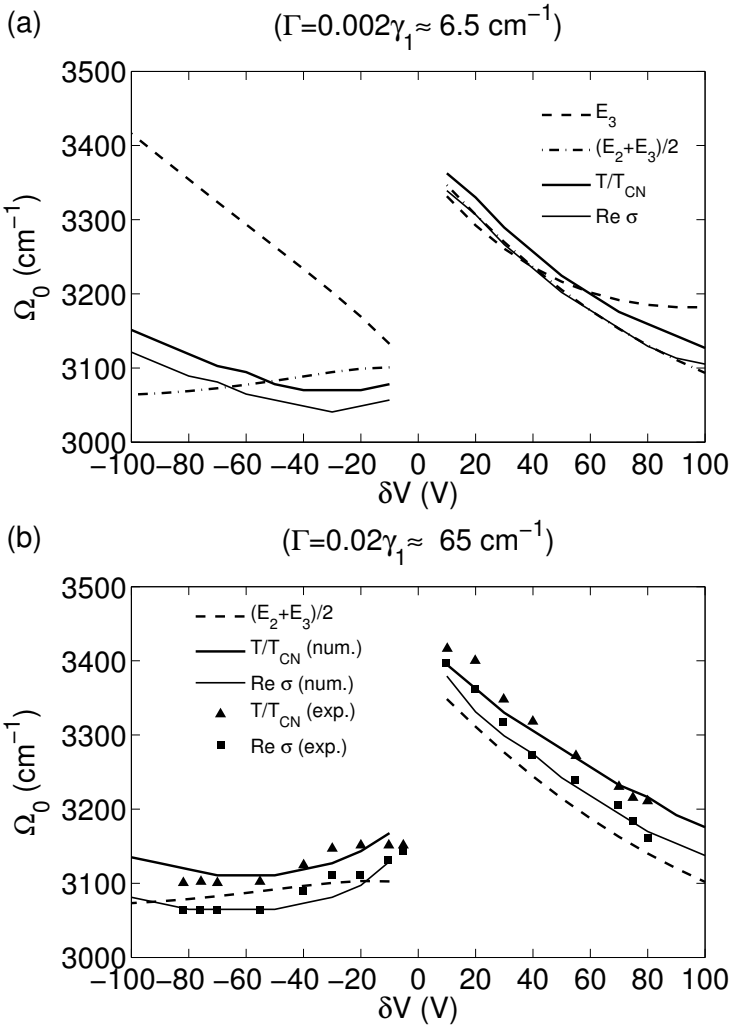

Figure 3.5: Position of the γ_1 peak *vs.* gate voltage for the two values of the broadening: (a) $\Gamma = 0.02\gamma_1$ and (b) $\Gamma = 0.002\gamma_1$. The solid lines are our numerical results from the conductivity; the thick lines are from the relative transmission. The dashed lines show E_3 and $(E_2 + E_3)/2$ in the cases (a) and (b), respectively. The SWMc parameters used in the calculation are listed in the first column of Table 3.1, except in (a) γ_3 is set to zero. The symbols are the peak positions determined from the measured conductivity (squares) and transmission (triangles).

Besides creating a finite $V_{\rm CN}$, these charges also move $V_{\rm b} = 0$ point away from the charge neutrality point $n = 0$. To the first approximation, [70] this introduces an offset of the interlayer bias: $V_{\rm b}(n) \to V_{\rm b}(n) + V_0$. However, our calculations suggest that for reasonable V_0 this effect has a smaller influence on the electron-hole asymmetry of the optical response than Δ and γ_4.

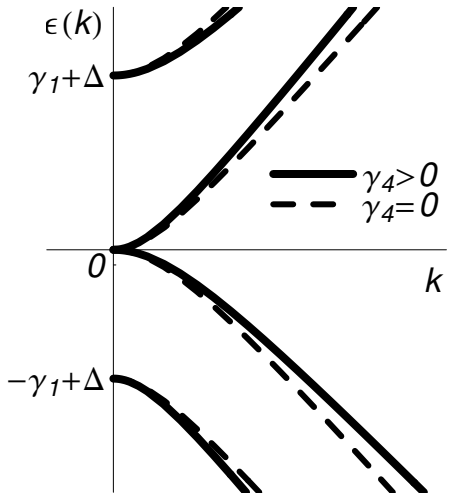

Figure 3.6: The effect of γ_4 and Δ on the band structure. Parameter Δ raises the bands 1 and 4. The interlayer neighbor hopping term γ_4 gives a contribution quadratic in k opposite in sign for the conduction and the valence bands. The solid (dashed) lines are the bands with positive (zero) value of γ_4.

Based on the above discussion, we can predict qualitatively how the position of the main conductivity peak should vary as a function of δV. For example, on the electron side, and for $v_4 > 0$, the peak should move to lower frequencies as δV increases. Alternatively, this can be seen from Fig. 3.6: the top two bands move closer to each other as $k = k_F$ increases.

For the quantitative analysis, we use a full numerical calculation of σ and T, which is discussed in Sec. 3.3 below. It demonstrates that for the case of small Γ the energy E_3 is indeed in a good agreement with the computed peak position Ω_0. However, the broadening observed in experiments [61, 62, 63] is appreciable, in which case the formula $\Omega_0 = (E_2 + E_3)/2$ is more accurate. Of course, for fairly large Γ other nearby transitions, E_1 and E_4, start to influence the lineshape

of the main peak. This is especially noticeable on the hole side, where the E_4-peak is right next to the main one. In the calculations this two-peak structure is unmistakable, see Fig. 3.4(b). In the experiment, where the main peak is for some reason strongly enhanced compared to the calculation, the E_4 peak is somewhat disguised. As pointed out by Kuzmenko, [63] the difference between E_4 and E_2 can in principle provide a direct spectroscopic measurement of the energy gap $V_{\rm b}$.

For detailed comparison with experiment we use our numerical results rather than Eqs. (3.4) and (3.5). Fitting them to the data, see Fig. 3.5, we have obtained estimates of γ_1, γ_4, and Δ listed in Table 3.1. This fitting procedure proved to be very straightforward. For example, Δ is determined mostly by the splitting of the peak positions on the electron and the holes sides of the charge neutrality point. Parameter γ_1 is essentially the average of the two. Finally, γ_4 controls the slope of the $\Omega_0(V_{\rm g})$ curves away from $V_{\rm CN}$. Therefore, all these parameters can be uniquely determined.

In Table 3.1 we also list SWMc values suggested in prior literature. They mainly agree with ours for the principal SWMc parameters γ_0 and γ_1 but show some deviations for the more subtle quantities γ_4 and Δ we have been discussing here. Possible reasons for these differences are given in Sec. 3.4.

3.3 Derivation

3.3.1 Band structure

The bilayer is two monolayers stacked together, see Fig. 3.1(a). In the bulk graphite the preferential stacking is the AB (Bernal) one, such that only one sublattice of each layer is bonded to each other. In order to achieve agreement with experiments, [61] we have to assume that in the bilayer the stacking is the same. We use the basis $\{\Psi_u, \Psi_v, \Psi_{\tilde{u}}, \Psi_{\tilde{v}}\}$, where the letter stands for the sublattice label and the number represents the layer index. In this basis the SWMc tight-binding

Hamiltonian for the bilayer becomes [27]

$$\mathbf{H} = \begin{pmatrix} -\frac{V_\mathrm{b}}{2} + \Delta & \phi & \gamma_1 & -v_4\phi^* \\ \phi^* & -\frac{V_\mathrm{b}}{2} & -v_4\phi^* & v_3\phi \\ \gamma_1 & -v_4\phi & \frac{V_\mathrm{b}}{2} + \Delta & \phi^* \\ -v_4\phi & v_3\phi^* & \phi & \frac{V_\mathrm{b}}{2} \end{pmatrix}, \tag{3.6}$$

where $\phi = -i(k_x + ik_y)$ and (k_x, k_y) is the deviation of the quasimomentum from the K point.

Given V_b, it is easy to obtain the four band energies $\varepsilon_\alpha(k)$ and the corresponding eigenstates $|\alpha, \mathbf{k}\rangle$ numerically. However, as mentioned in Sec. 3.2, V_b should be determined self-consistently as a function of V_g, or equivalently, the total carrier concentration n. The algorithm for doing so is given next.

3.3.2 Electrostatics

As discussed in the literature, [70, 27] the electric field of the gate has two major effects on the bilayer graphene. First, it modifies the bands by introducing a potential difference between the layers and as a consequence opens up the energy gap. Second, it induces charge carriers. Electric field of the charged impurities can play a similar role: it creates a layer asymmetry V_0 and opens a gap at the charge neutral point much like an external gate. But the more important effect of the impurities is presumably the broadening of the electron energy states, which we describe by a phenomenological constant Γ. For example, if the impurities are distributed symmetrically between the two layers, then V_0 is zero but Γ is still finite. We assume Γ to be real and independent of energy, momentum, or a band index. This is certainly a very rudimentary treatment of disorder compared to, e.g., self-consistent schemes. [67, 27, 74] However, since the source of disorder in graphene is still debated, we think that this simple approach is adequate for our purposes as long as Γ is treated as another adjustable parameter.

To compute $V(n)$ and $\mu(n)$ we set up a system of equations similar to those in Refs. [70] and [56]. These equations capture the dominant Hartree term of the interaction but neglect exchange and correlation energies. [53] The first equation

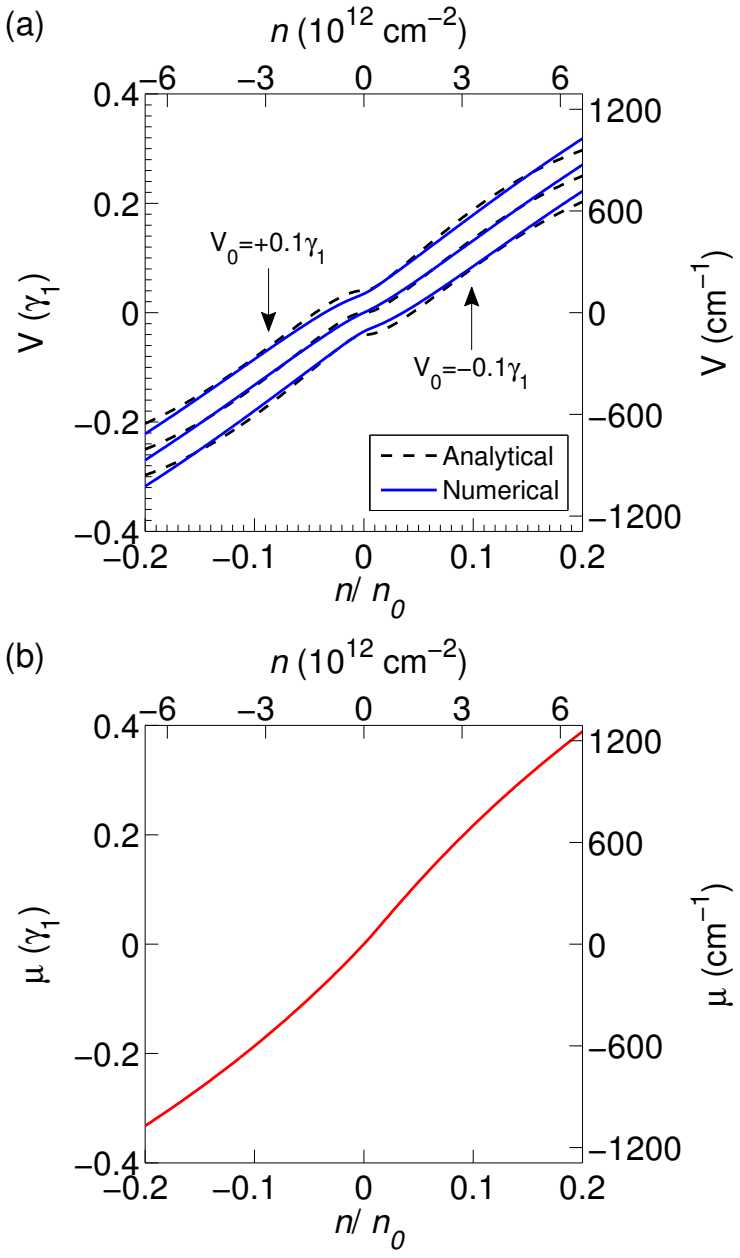

Figure 3.7: (a) Interlayer bias V_b as a function of total density n. Three sets of curves correspond to (from top to bottom) $V_0 = 0.1\gamma_1$, 0, and $-0.1\gamma_1$. The dashed lines are computed from Eq. (3.12). (b) Chemical potential *vs.* n for $V_0 = -0.1\gamma_1$.

is [cf. Eq. (3.2)]

$$n = n_t + n_b = C_b \delta V / e \,, \tag{3.7}$$

where n_t and n_b are the carrier concentrations of the top and bottom layers, and C_b is the capacitance to the gate. Second, the electrostatic potential difference between the two layers V_b is given by

$$V_\mathrm{b} = \frac{4\pi e^2}{\kappa}(n_t - n_b)c_0 \,, \tag{3.8}$$

where κ is the dielectric constant and c_0 is the distance between the layers. Next, the Hamiltonian and hence the wavefunction and the layer density n_t and n_b depend on V_b. Therefore the quantities V_b, n_t, and n_b must be solved for self-consistently. If the broadening Γ is neglected, this can be done analytically in the limit $V_\mathrm{b}, \mu \ll \gamma_1$, which gives $V \simeq \mathcal{V}(n, V_0)$, where [70, 56]

$$\mathcal{V}(n, V_0) = \frac{X\gamma_1 + V_0}{\Lambda^{-1} + |X| - \frac{1}{2}\ln|X|} \,, \quad X = \frac{\pi n}{n_0} \,, \tag{3.9}$$

n_0 is defined by Eq. (3.1), and $\Lambda \equiv e^2 c_0 n_0/(\pi\kappa\gamma_1)$ is the dimensionless strength of the interlayer screening. Using the typical parameter values, one estimates [70] $\Lambda \sim 1$, and so the interlayer screening is significant. [70, 53]

For experimentally relevant broadening $\Gamma \sim 0.02\gamma_1$, the approximation leading to Eq. (3.9) is no longer accurate. Therefore, we computed the dependence of n_t and n_b on V_b numerically as follows. We first define the retarded Green's function $\mathbf{G}^R$ by the analytic continuation $\mathbf{G}^R(\varepsilon) = \mathbf{G}(\varepsilon \to \varepsilon + i\Gamma)$ of the following expression

$$\mathbf{G}(\varepsilon) = \sum_{\alpha=1}^{4} \frac{1}{\varepsilon - \varepsilon_\alpha(k)} |\alpha, \mathbf{k}\rangle \langle \alpha, \mathbf{k}| \,. \tag{3.10}$$

Then we compute n_t from

$$n_t = -\int \frac{d^2k}{(2\pi)^2} \int_{-\infty}^{\mu} \frac{d\varepsilon}{\pi} \mathrm{Im}[G^R_{11}(\mathbf{k}, \varepsilon) + G^R_{22}(\mathbf{k}, \varepsilon)] \,, \tag{3.11}$$

using numerical quadrature. Similarly, the formula for n_b is obtained by replacing $G_{11} + G_{22}$ with $G_{33} + G_{44}$.

The system of nonlinear equations (3.7), (3.8), and (3.11) is solved by an iterative procedure. For a given chemical potential μ we start from some initial

guess on V_b. Then we diagonalize the Hamiltonian and compute $\mathbf{G}^R$, n_t, and n_b. Substituting them into Eq. (3.8), we get the value of V_b for the next iteration. (Actually, we use not this value directly but a certain linear combination of the new and old V_b to achieve convergence.) The iterations terminate when the values of V_b changes by less than a desired relative accuracy (typically, 10^{-5}). The results of these calculations are in a good agreement with Eq. (3.9) for $\Gamma = 0$, and so are not shown. On the other hand, the results for $\Gamma = 0.02\gamma_1$, which are plotted in Fig. 3.7, appreciably deviate from Eq. (3.9). The agreement greatly improves (see Fig. 3.7) if instead of Eq. (3.9) we use, on heuristic grounds, the following formula:

$$V(n) = \mathcal{V}(n_*, V_0) - \mathcal{V}(n_\Gamma, 0)\,, \tag{3.12}$$

$$n_* = \mathrm{sign}(n)\sqrt{n^2 + n_\Gamma^2}\;, \quad n_\Gamma = \mathrm{sign}(n)\frac{2\Gamma n_0}{\pi\gamma_1}\,. \tag{3.13}$$

3.3.3 Dynamical conductivity

The above procedure enables us to compute V_b and n for a given chemical potential μ. With the former determining the Hamiltonian and therefore its eigenstates, and the latter determining their occupancy, we can now compute the dynamical conductivity by the Kubo formula [75]

$$\sigma_{xx}\left(\Omega\right) = i\,\frac{\Pi^R_{xx}(\Omega) - \Pi^R_{xx}(0)}{\Omega + i0}\,, \tag{3.14}$$

where the polarization operator $\Pi^R_{xx}(\Omega)$ is given by

$$\begin{aligned}\Pi^R_{xx}(\Omega) = ig\frac{e^2}{\hbar^2}\int\frac{d^2k}{(2\pi)^2}\int\limits_{-\infty}^{\mu}\frac{d\varepsilon}{2\pi}\mathrm{Tr}\left\{\mathbf{v}_x\left[\mathbf{G}^R\left(\mathbf{k},\varepsilon\right) - \mathbf{G}^A\left(\mathbf{k},\varepsilon\right)\right]\right.\\ \left.\cdot\mathbf{v}_x\left[\mathbf{G}^R\left(\mathbf{k},\varepsilon+\Omega\right) + \mathbf{G}^A\left(\mathbf{k},\varepsilon-\Omega\right)\right]\right\}\,.\end{aligned} \tag{3.15}$$

In this equation $g = 4$ is the spin-valley degeneracy of graphene, $\mathbf{v}_x = \hbar^{-1}\partial\mathbf{H}/\partial k_x$ is the velocity operator, and $\mathbf{G}^{R,A}$ at the retarded and the advanced Green's functions. Assuming again that the broadening is momentum and energy independent, these functions are obtained by the analytic continuation of $\mathbf{G}$ in Eq. (3.10): $\mathbf{G}^{R,A}\left(\varepsilon\right) = \mathbf{G}\left(\varepsilon \to \varepsilon \pm i\Gamma\right)$. After some algebra, we find

$$\Pi^R_{xx}\left(\Omega\right) = ig\left(\frac{e}{\hbar}\right)^2\int\frac{d^2k}{\left(2\pi\right)^2}\sum_{\alpha,\beta}\left|M_{\alpha\beta}(\mathbf{k})\right|^2\sum_{\xi,\zeta=\pm1}\xi K\left[\varepsilon_\beta\left(k\right) - i\Gamma\xi,\ \varepsilon_\alpha\left(k\right) - \left(i\Gamma + \Omega\right)\zeta\right]\,, \tag{3.16}$$

where $M_{\alpha\beta}(\mathbf{k}) = \langle \alpha, \mathbf{k} | \mathbf{v}_x | \beta, \mathbf{k} \rangle$ are the transition matrix elements and function K is defined by

$$K(z_1, z_2) = \frac{\ln(\mu - z_1) - \ln(\mu - z_2)}{2\pi(z_1 - z_2)} \tag{3.17}$$

with the branch cut for $\ln z$ taken to be $(-\infty, 0]$.

For vanishing V_b and Γ the conductivity can be computed in the closed form, see Appendix 3.5.2. For other cases, we evaluated it numerically. The results are shown in Figs. 3.2 and 3.4. To demonstrate agreement with previous theoretical calculations, [64, 27, 66, 56] we present $\sigma(\Omega)$ computed for a very small broadening Γ in Fig. 3.2. In this case one can easily identify all six transitions. As explained above, the sharp features at $\Omega \approx 3200\,\mathrm{cm}^{-1}$ are due to the high optical density of states at energies $E_2 < \hbar\Omega < E_3$. The other prominent feature at $\Omega = 0$ is the intraband Drude peak. (Its height is related to the transport mobility.) In Fig. 3.4 the calculation is done for much larger Γ to match the experimental data. This Figure has been discussed in detail in Sec. 3.2.

3.4 Discussion

In this paper we presented a joint experimental and theoretical study of the infrared response of a bilayer graphene. Our results demonstrate a complex interplay among various interband transitions and their disorder-induced broadening. Nevertheless, by means of a careful analysis, we have been able to explain the majority of the observed features within the conventional SWMc model. The corresponding SWMc parameters are given in Table 3.1, together with their estimated uncertainties. In particular, our γ_1 should have a very high accuracy: about $100\,\mathrm{cm}^{-1}$, i.e., 3%. The uncertainty in γ_1 comes predominantly from an unknown systematic error that we make by neglecting the renormalization of the spectrum by scattering processes. Since we assume that the imaginary part $\Gamma \approx 65\,\mathrm{cm}^{-1}$ of the electron self-energy due to scattering is constant, its real part has to vanish by the Kramers-Krönig relations. In fact, this real part, which is generally finite, [27] can shift the observed transition frequencies by an amount that scales with Γ.

Let us now compare our SWMc parameters with those found in previous work on bilayers and bulk graphite. For the bilayer case there is at present only one other experimental determination [45] of γ_j's. From Table 3.1 we see that the difference between our and their values is primarily in γ_1. Actually, our SWMc parameters can describe the Raman data equally well [16] as those given in Ref. [45]. Our parameter values have smaller estimated errors and should be considered more accurate.

In comparison with bulk graphite, the strongest discrepancy is in the value of Δ. The difference is significantly larger than the uncertainty of $\Delta_{\rm graphite}$ quoted in the early [15, 44] and the recent experimental work, [55] which makes a strong case that $\Delta_{\rm bilayer}$ differs from $\Delta_{\rm graphite}$ both in sign and in magnitude. To judge the true significance of this result, one should recall that the physical meaning of $\Delta_{\rm bilayer}$ is the difference in the onsite energies of the A and B sublattices. [41] However, in graphite the role of the same quantity is played not by Δ but by the linear combination [42]

$$\Delta'_{\rm graphite} \equiv \Delta_{\rm graphite} - \gamma_2 + \gamma_5 \,. \tag{3.18}$$

For the sake of convenience, let us set $\gamma_2 = \gamma_5 = 0$ in the bilayer, so that the A-B energy difference is equal to Δ' in both materials. Taking the most commonly used [44] parameter values for graphite, we arrive at the remarkable empirical relation

$$\Delta'_{\rm graphite} \approx 37\,{\rm meV} \approx 2\Delta'_{\rm bilayer} \,, \tag{3.19}$$

which is much easier to interpret. Indeed, the physical origin of Δ' is the short-range (exponentially decaying with distance) repulsion due to exchange and correlation effects between the electron states of the stacked atoms. (Neither Coulomb nor even the van der Waals interaction have short enough range to effectively discriminate between the two sublattices, [76, 77] given the relatively large interlayer distance.) Since in the bilayer each A atom has a single stacking partner while in the Bernal graphite it has two of them, Eq. (3.19) is exactly what one would expect. More precisely, it is expected if the interlayer distance in the bilayer and

[16] J. Nilsson, private communication.

in the graphite are nearly the same. The validity of Eq. (3.19) can be considered an experimental evidence that this is indeed so.

Another SWMc constant, which may seem to be different in the bilayer and the bulk graphite is γ_4. As mentioned in Sec. 3.1, this is one of the parameters that in the past have been difficult to determine very accurately. Our estimate of γ_4 can be defended on the grounds that (i) it agrees with the Raman experiments [45] and (ii) it is comparable to the accepted value of γ_3. These two parameters describe hopping between pairs of atoms at equal distances in the lattice, see Fig. 3.1(a), and theoretically are not expected to be vastly different from each other. Large difference of γ_4 between the bilayer and the bulk graphite is not expected either. Indeed, even when they disagree about the order of magnitude (or sign) of Δ, all electronic structure calculations to date find that $\gamma_4 \sim \gamma_3$ and are of the same order of magnitude in the two systems, see Table 3.1.

SWMc Parameter γ_3 itself cannot be reliably extracted from the experimental data [61] we analyzed here. At the relevant carrier concentrations the main effect of γ_3 is to produce a weak trigonal warping of the band dispersion. [44] This warping averages out over the Fermi surface, and so has an effect similar to the broadening Γ: it makes the γ_1 conductivity peak more symmetric and shifts it towards the midpoint of E_2 and E_3, i.e., to slightly lower frequencies, cf. Figs. 3.4(a) and (b). Thus, it is difficult to separate the effect of γ_3 from the broadening due to disorder.

Regarding the latter, the dc mobility that we find from our numerically computed $\sigma(0)$ using $\Gamma = 0.02\gamma_1 \approx 8\,\mathrm{meV}$ is $\mu \approx 3900\,\mathrm{cm}^2\,/\,\mathrm{Vs}$. This is close to the transport mobility typical for bilayer graphene, supporting our interpretation that Γ arises mainly due to disorder.

Concluding the paper, we wish to draw attention to several features of the experimental data that are not accounted for by our model. One of them is an unexpectedly large amount of the optical weight in a range of frequencies below the γ_1 peak. It is present between the Drude peak and 2μ, i.e., twice the chemical potential. For the chosen Γ, our calculation predicts $\mathrm{Re}\,\sigma(\Omega) \sim 0.02e^2/\hbar$ at such Ω, see Fig. 3.3, whereas the measured value is several times larger. [61]

This extra weight is present also in the monolayer graphene, in the same range of frequencies. [72] A related issue is a very gradual rise of $\mathrm{Re}\,\sigma(\Omega)$ around the point $\Omega = 2\mu$ compared to a sharp threshold expected theoretically. These features can be in part due to electron-phonon interaction [74] or midgap states [74, 78] but other effects seem to be involved as well.

One very simple explanation would be to attribute both the broadening of the $\Omega = 2\mu$ threshold and the extra weight at $\Omega < 2\mu$ to long-range density inhomogeneities in the sample. They can be caused by charge impurities and remnants of the photoresist used in the sample processing. The presence of such inhomogeneities would modulate the local chemical potential, and so in the infrared response one would see a certain average of the $\sigma\,(\Omega)$ taken at different δV. We illustrate this argument by calculating the arithmetic mean of $\sigma\,(\Omega)$'s for positive (negative) δV and superimposing the results (shown by the dashed lines) on the $\sigma\,(\Omega)$ traces for $\delta V = +50\,\mathrm{V}$ $(-50\,\mathrm{V})$ in Fig. 3.4(b). Such averaged conductivities indeed resemble the experimental data [Fig. 3.4(b)] more faithfully.

Another discrepancy between the experiment and the present theory is the lineshape of the γ_1-peak. By varying Γ, we can fit either the width or the height of the peak but not both. For example, in Fig. 3.4, where we chose to fit the width, the measured height of the peak is sometimes nearly twice larger than the theory predicts. The extra optical weight of the peaks appears to have been transferred from their high-frequency sides, which are suppressed in experiment compared to the calculations. These lineshape differences are significant enough to make us think that some essential physics is still missing in the simple single-particle picture presented in this paper. We speculate that including many-body effects may be truly necessary for bringing theory and experiment to better agreement.

3.5 Appendix

3.5.1 Reflection and Transmission

To compute the transmission coefficient T and the reflection coefficient R we follow the standard procedure. [79] In general, the result depends on the angle

of incidence and on the polarization of light. Abergel and Fal'ko [7] derived the formulas for R and T for the S-polarization where the electric field is perpendicular to the plane of incidence (and parallel to the sample surface). We reproduce them here with a slight change in notation:

$$\begin{aligned} R &= \left| -\frac{C\, n_1 \cos\theta_1 - D\,[\cos\theta_0 - 4\pi\sigma]}{C\, n_1 \cos\theta_1 + D\,[\cos\theta_0 + 4\pi\sigma]} \right|^2 , \\ T &= \left| -\frac{2\cos\theta_0\; n_1 \cos\theta_1\; n_2 \cos\theta_2}{C\, n_1 \cos\theta_1 + D\,[\cos\theta_0 + 4\pi\sigma]} \right|^2 , \end{aligned} \tag{3.20}$$

where A, B, C, and D are given by

$$\begin{aligned} A &= \cos\theta_2 \sin\delta_2 + i n_2 \cos\theta_0 \cos\delta_2 \,, \\ B &= i \cos\theta_2 \cos\delta_2 + n_2 \cos\theta_0 \sin\delta_2 \,, \\ C &= A\, n_1 \cos\theta_2 \sin\delta_1 + iB\, n_2 \cos\theta_1 \cos\delta_1 \,, \\ D &= iA\, n_1 \cos\theta_2 \cos\delta_1 + B\, n_2 \cos\theta_1 \sin\delta_1 \,. \end{aligned} \tag{3.21}$$

In Eqs. (3.20) and (3.21), the index $j = 0, 1, 2$ represents vacuum, SiO_2, and Si layers respectively, n_j are the index of refraction of each layer, and θ_j are the angles the light ray makes with the surface normal in each layer. They satisfy Snell's law $n_j \sin\theta_j = \text{const}$. Finally, $\delta_j = kL_j n_j \cos\theta_j$ is the phase the light picks up as it makes one pass across the layer of thickness L_j.

For the other, P-polarization, where the electric field is not exactly parallel to the surface of the sample, we find a different expression:

$$\begin{aligned} R &= \left| \frac{C\, n_1 \cos\theta_0 - D\, \cos\theta_1\,(1 - 4\pi\sigma\cos\theta_0)}{C\, n_1 \cos\theta_0 + D\, \cos\theta_1\,[1 + 4\pi\sigma\cos\theta_0]} \right|^2 , \\ T &= \left| \frac{-2\cos\theta_0\, n_1 \cos\theta_1\, n_2 \cos\theta_2}{C\, n_1 \cos\theta_0 + D\, \cos\theta_1\,[1 + 4\pi\sigma\cos\theta_0]} \right|^2 . \end{aligned} \tag{3.22}$$

For this polarization the conductivity enters R and T multiplied by the cosine of the angle of incidence, i.e., its effect is reduced. In our experiments, we typically have $\theta_0 \sim 30^\circ$, and so this reduction is quite small. Its role is further diminished by the presence of both polarizations in the infrared beam. Thus, we decided not to include it in the analysis and do all the calculation assuming the S-polarization only.

3.5.2 Conductivity of an unbiased bilayer at vanishing broadening

The conductivity for the case $\Gamma = V_{\rm b} = 0$ was computed previously in Refs. [64] and [7]. In our attempt to reproduce their formula we discovered that it contains a typographical sign error [17]. For future reference, we give the corrected expression below.

In the limit of zero broadening, $\Gamma \to 0$, Eqs. (3.14)–(3.17) reduce to the following expression for the conductivity:

$$\sigma(\Omega) = \frac{ge^2v^2}{2i\pi\hbar} P\int_0^\infty \frac{d\omega}{\omega} \frac{\Omega |M_{\alpha\beta}|^2}{\omega^2 - (\Omega + i0)^2} \sum_j k_j(\omega) k_j'(\omega)\,, \tag{3.23}$$

where P means principal value and the integration variable $\omega = |\varepsilon_\alpha - \varepsilon_\beta|$ is the energy difference between two states. The sum in Eq. (3.23) is over all values of momentum $k_j(\omega)$ of which two states differing in energy ω exist. For $V = 0$ where the the matrix elements $M_{\alpha\beta}$ take a simple form, the integration over ω in Eq. (3.23) can be done analytically. The result can be written as a sum of three terms:

$$\frac{\sigma(\Omega)}{\sigma_0} = \tilde\sigma_0(\Omega) + \tilde\sigma_{\gamma_1}(\Omega) + \tilde\sigma_{2\gamma_1}(\Omega)\,, \tag{3.24}$$

where $\sigma_0 = e^2/\hbar$ is the unit of conductivity, $\tilde\sigma_0$ is contribution from transitions between bands 2 and 3 that turn on at $\Omega = 0$, $\tilde\sigma_{\gamma_1}$ is contribution from transitions between bands 1 and 3 and bands 2 and 4 that turn on at $\Omega = \gamma_1$, $\tilde\sigma_{2\gamma_1}$ is contribution from transition between bands 1 and 4 that turn on at $\Omega = 2\gamma_1$. They are given by

$$\tilde\sigma_0 = \frac{g}{8}\left[\frac{1}{2}\frac{\Omega + 2\gamma_1}{\Omega + \gamma_1} - \frac{i}{\pi}\frac{\Omega\gamma_1}{\gamma_1^2 - \Omega^2}\ln\left|\frac{\Omega}{\gamma_1}\right|\right]\,, \tag{3.25a}$$

$$\tilde\sigma_{\gamma_1} = \frac{g}{8}\left[\frac{\gamma_1^2}{\Omega^2}\Theta(\Omega - \gamma_1) + \frac{i}{\pi}\left(\frac{2\gamma_1}{\Omega} - \frac{\gamma_1^2}{\Omega^2}\ln\left|\frac{\gamma_1 + \Omega}{\gamma_1 - \Omega}\right|\right)\right]\,, \tag{3.25b}$$

$$\begin{aligned}\tilde\sigma_{2\gamma_1} = \frac{g}{8}\Bigg[&\frac{1}{2}\frac{\Omega - 2\gamma_1}{\Omega - \gamma_1}\Theta(\Omega - 2\gamma_1) - \frac{i}{\pi}\Bigg(\frac{1}{2}\frac{\Omega^2 - 2\gamma_1^2}{\Omega^2 - \gamma_1^2} \\ &\times \ln\left|\frac{2\gamma_1 + \Omega}{2\gamma_1 - \Omega}\right| + \frac{1}{2}\frac{\Omega\gamma_1}{\Omega^2 - \gamma_1^2}\ln\left|\frac{4\gamma_1^2 - \Omega^2}{\gamma_1^2}\right|\Bigg)\Bigg]\,,\end{aligned} \tag{3.25c}$$

where, for ease of notation, Ω stands for $\hbar\Omega$ and $g = 4$.

[17] D. Abergel and V. I. Fal'ko, private communication.

3.6 Acknowledgment

Chapter 3, almost in full, is a reprint of material as it appears in L. M. Zhang, Z. Q. Li, D. N. Basov, M. M. Fogler, Z. Hao, and M. C. Martin. Determination of the electronic structure of bilayer graphene from infrared spectroscopy. *Phys. Rev. B*, 78(23):235408, 2008.The dissertation author was the primary investigator and author of this paper.

Chapter 4

Landau level dispersion, Berry phase, and magnetoelectric coupling in a biased bilayer graphene

4.1 Introduction

We have already seen that an unique feature of bilayer graphene (BLG) is its tunable band structure: the symmetric bilayer is gapless but when an interlayer potential difference U is induced, a band gap opens. The low-energy regions affected by the gap are situated at the Brillouin zone corners, e.g., points $\mathbf{K}^{\pm} = \pm\frac{4\pi}{3a_0}\,\hat{\mathbf{x}}$ henceforth referred to as $K^{\pm}$ valleys, near which the band dispersion acquires a "Mexican hat" shape [26, 80] (see Fig. 1.3), where $a_0 = 2.461\,\text{Å}$ is the lattice constant for the underlying triangular Bravais lattice.

Although there have been interesting theoretical predictions that electron interactions can spontaneously generate layer polarization and a band gap [81, 82, 83, 84, 85, 86], they have yet to be verified experimentally. [1] The proven ways

[1] Some encouraging results in this direction have been reported in Refs. [87]. However, the observed gap is comparable to that in the single-particle picture, see Fig. 4.4 in Sec. 4.2. The gaps measured in another experiment [88] are even smaller, possibly due to much stronger disorder.

of creating an interlayer bias U include doping and gating. The latter enables one to change U continuously, although the dependence of U on the gate voltage is nontrivial. [70, 58] In most of experimental studies of bilayer graphene a single gate electrode was used. [89, 90, 60, 58, 91, 72, 92, 63, 93, 94, 88] In such devices the interlayer bias U and the induced electron density n vary concomitantly with the gate voltage. Separate control of U and n can be achieved with two gates. [95, 96] Experiments with dual-gate devices [59, 95, 97, 87, 98] have been reported recently.

Another intriguing property of graphene is that its low-energy quasiparticles are endowed with a pseudospin-$\frac{1}{2}$ degree of freedom, associated with the sublattice structure of each monolayer, whose dynamics is linked to their orbital motion. [25] When a quasiparticle traces a closed-loop trajectory in momentum space, its pseudospin sweeps out a certain solid angle, just as in the canonical Berry phase setting. [99, 100] Such orbits naturally occur when an external magnetic field B is present — they are the cyclotron orbits. In monolayer graphene the corresponding Berry phase is equal to $\pi = \frac{1}{2} \times (2\pi)$ at all energies. [101] This property is the reason for the $\frac{1}{2}$-shift in the Landau level (LL) filling factor $\nu = 4 \times (N + \frac{1}{2})$ at which N^{th} magnetoconductance minimum occurs. [102, 103] Here the factor of four is the spin-valley degeneracy, assuming it is preserved.

Given the unusual band structure of BLG, it is interesting to consider the effects of the Berry phase and other pseudospin-related phenomena on the Landau levels and the magnetic response in this material. Indeed, it is known [104, 105] that the pseudospin generates a linear coupling to the transverse component B_z of the magnetic field, similar to a real spin.

Note that such a pseudo-Zeeman coupling does not violate the time reversal symmetry of the system at $B = 0$. Since this symmetry operation interchanges the valleys, it is only the sum $M_z^+ + M_z^-$ of the corresponding magnetic moments that must vanish. Further symmetry considerations require the pseudo-Zeeman shift of the energy eigenvalue $E_{\mathbf{q}}$ to be linear in both applied fields,

$$\Delta E_{\mathbf{q}} \propto -E_z B_z \cos 3\phi_{\mathbf{q}} \,, \tag{4.1}$$

where $\phi_{\mathbf{q}}$ is the polar angle in reciprocal space relative to the zone center $\mathbf{q} = 0$. This expression conforms to the following valley-interchanging operations: (i) a

reflection O_1 with respect to the y-z plane, and (ii) a composite operation O_2 consisting of a rotation through angle π around x-axis in the midplane, followed by time reversal. Both of these operations leave the crystal structure invariant (see Fig. 1.4). The first one keeps E_z the same but reverses the sign of B_z (because $\mathbf{B}$ is a pseudovector). The second changes the sign of E_z but keeps B_z the same.

Equation (4.1) constitutes a magnetoelectric effect in bilayer graphene. It implies that the valley symmetry cannot be broken solely by B_z or by E_z alone. Rather, both fields must be nonzero simultaneously. (It is also reminiscent of the Chern-Simons term which occurs in topological insulators. [106]) Below we study this kind of valley-symmetry breaking analytically, focusing on the question how it modifies the Landau level dispersion.

Prior theoretical studies [26] have already showed that Landau levels in bilayer graphene become valley split at finite U. This was explained by noting that the quasiparticle wavefunctions of the two valleys have different dipole moments in the z-direction. Equation (4.1) offers a complementary interpretation: the two valleys in a biased bilayer graphene have different magnetic moments. [104, 105]

The ratio of the pseudo-Zeeman term (4.1) and the Zeeman energy due to real spin determine the effective g-factor of bilayer graphene. We show below that g can be an order of magnitude higher than its bare value $g = 2$. This resembles the situation in Bi, another low band gap material. In fact, there is a mathematical similarity of the low-energy theories [107] of the two materials. (Of course, Bi is three-dimensional.)

The dependence of Landau level energies in bilayer graphene on B_z and U is known to be quite complicated (see, *e.g.*, Refs. [108, 109, 110]). We show that it can be understood if one applies quasiclassical quantization to the Mexican hat band structure. This procedure requires calculating the phase shifts Φ_c acquired by quasiparticles on their cyclotron orbits. Both the pseudo-Zeeman term and the Berry phase contribute to Φ_c. As a result, Φ_c generally is not an integer multiple of the monolayer value π. When it does become equal to π, at certain values of U, an interesting phenomenon occurs: adjacent Landau levels of opposite valleys become degenerate. Therefore, there are an infinite number of Landau level

crossings within the same band.

Landau level crossings in the two dimensional electron gas (2DEG) has previously attracted much theoretical [111, 112, 113, 114, 115, 116, 117] and experimental [118, 119, 120, 121, 122, 123, 124, 125, 126, 127, 128, 129] interest because the 2DEG then exhibits many of the properties found in ferromagnets. Therefore, BLG may be a promising system for studying quantum Hall ferromagnetism.

The remainder of this article is organized as follows. A brief summary of BLG band structure properties is given in Sec. 4.2. The quasiclassical approximation is discussed in Sec. 4.3. Illustrative Landau level spectra are presented in Sec. 4.4. The anomalous Hall conductivity of the BLG is computed in Sec. 4.5. Concluding remarks are given in Sec. 4.6. Technical notes are gathered in the Appendix.

4.2 Analytic results from prior work

4.2.1 Quantizing magnetic field

In the presence of a magnetic field $\mathbf{B} = B\hat{\mathbf{z}}$, the two components of the wavevector no longer commute. Near the zone corners, we invoke the Kohn-Luttinger substitution $k_i \to \pi_i$ such that $[\pi_x, \pi_y] = -i/\ell_B^2$, where $\ell_B = \sqrt{\hbar c/e|B|}$ is the magnetic length. We define the ladder operators,

$$a = -\frac{\ell_B}{\sqrt{2}}\left(\pi_x - i\pi_y\right), \quad a^\dagger = -\frac{\ell_B}{\sqrt{2}}\left(\pi_x + i\pi_y\right), \tag{4.2}$$

which satisfy the commutation relation

$$\left[a\,,\, a^\dagger\right] = \mathrm{sgn}(B)\,. \tag{4.3}$$

Using Eqs. (1.10) and (4.2), we find the Hamiltonian of K^+ valley to be

$$\mathcal{H}^+(U) = \begin{pmatrix} -U & -\omega_0\, a & \eta_4\,\omega_0\, a & \eta_3\,\omega_0\, a^\dagger \\ -\omega_0\, a^\dagger & -U + \Delta' & \gamma_1 & \eta_4\,\omega_0\, a \\ \eta_4\,\omega_0\, a^\dagger & \gamma_1 & U + \Delta' & -\omega_0\, a \\ \eta_3\,\omega_0\, a & \eta_4\,\omega_0\, a^\dagger & -\omega_0\, a^\dagger & U \end{pmatrix}, \tag{4.4}$$

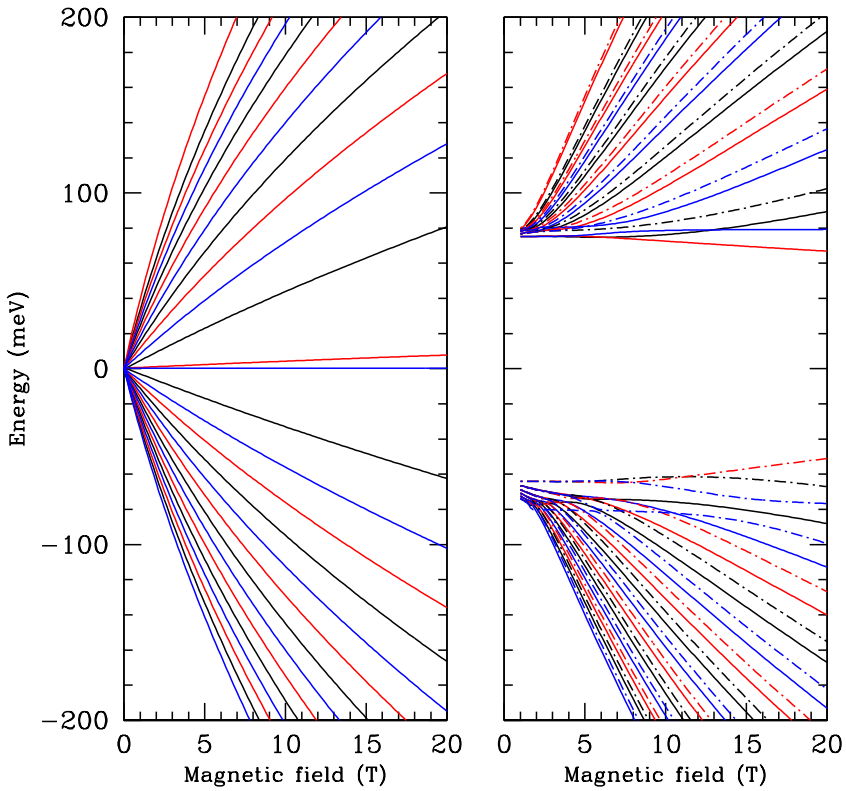

Figure 4.1: Landau level energies *vs.* magnetic field for $U = 0$ (left) and $U = 80\,\text{meV}$ (right). Solid lines correspond to the K^+ valley and broken lines to the K^- valley. The color distinguishes the spectra of $\mathcal{H}_\text{a}$ (black), $\mathcal{H}_\text{b}$ (red), and $\mathcal{H}_\text{c}$ (blue), where $\mathcal{H}_\text{a,b,c}$ are defined in Appendix B.

where $\eta_3 = \gamma_3/\gamma_0 = 0.1$, $\eta_4 = \gamma_4/\gamma_0 = 0.05$, and

$$\omega_0 = \sqrt{2}\,\frac{\hbar v_0}{\ell_B} \approx 35\,\text{meV}\sqrt{|B(\text{T})|}\,. \tag{4.5}$$

Throughout we shall ignore the effects of real Zeeman splitting, which are small due to the value of the Bohr magneton, $\mu_\text{B} = e\hbar/2m_\text{e}c = 57.9\,\mu\text{eV/T}$. At the highest fields in the relevant experiments ($B \approx 30\,\text{T}$) the real Zeeman splitting is on the order of a few millivolts, which is much smaller than even the smallest of the SWMc energy scales. (As we shall see, the pseudo-Zeeman effect can be significantly larger.)

The Hamiltonian $\mathcal{H}^-$ of K^- valley is obtained from $\mathcal{H}^+$ via the replacements

$$R: \quad a \to -a^\dagger\,, \quad a^\dagger \to -a\,, \tag{4.6}$$

which is the reflection in the y–z plane. The commutation relation (4.3) between a and $a^\dagger$ and therefore the energy spectrum is preserved if we additionally reverse the magnetic field,

$$R_B: \quad B \to -B\,. \tag{4.7}$$

Taken together, these replacements implement the symmetry operation $O_1 = RR_B$ discussed in Sec. 4.1. The other valley-interchanging operator O_2 is represented in terms of the unitary matrix

$$\mathcal{V} = \begin{pmatrix} 0 & \sigma_x \\ \sigma_x & 0 \end{pmatrix} \tag{4.8}$$

and the time-reversal operation $S_{\mathbf{q}} \to (S_{\mathbf{q}})^*$, i.e.,

$$R_T: \quad a \to -a\,, \quad a^\dagger \to -a^\dagger\,, \quad B \to -B\,. \tag{4.9}$$

It is easy to see that

$$\mathcal{H}^-(U) = R_T R_B \left[\mathcal{V}^\dagger\, \mathcal{H}^+(-U)\, \mathcal{V}\right]. \tag{4.10}$$

Since $R_T R_B$ does not change the commutation relation (4.3), the spectra of $\mathcal{H}^-(U)$ and $\mathcal{H}^+(-U)$ coincide. Thus, it suffices to discuss the spectrum of $\mathcal{H}^+$, from which one can obtain the spectrum of $\mathcal{H}^-$ by reversing the sign of either U or B.

These symmetries further imply that at $B = 0$ the two valleys are degenerate in energy and that additionally, each valley is symmetric under $U \to -U$. On the other hand, at finite B, the valleys are degenerate only if $U = 0$. Note also that the total spectrum, including both valleys, is particle-hole symmetric when $\Delta' = \gamma_4 = 0$.

Making use of the eigenvectors $|n\rangle$ of the number operator $a^\dagger a$, we write the general bilayer wavefunction as

$$|\Psi\rangle = \sum_{n=0}^{\infty} \begin{pmatrix} u_n\,|n\rangle \\ v_n\,|n\rangle \\ \tilde{u}_n\,|n\rangle \\ \tilde{v}_n\,|n\rangle \end{pmatrix}. \tag{4.11}$$

The structure of the resulting Hamiltonian is discussed in Appendix B. If all SWMc parameters are kept, it can be diagonalized only numerically. Some results are

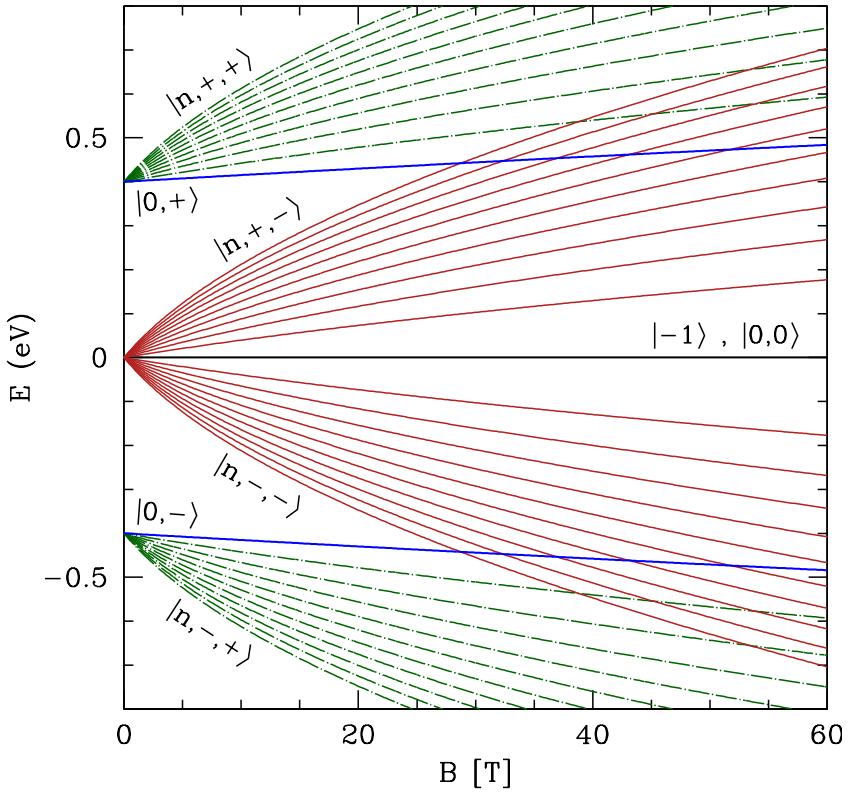

Figure 4.2: Landau level energies *vs.* magnetic field B for the case $\gamma_3 = \gamma_4 = U = 0$. The labeling of the states corresponds to that in the text.

shown in Figs. 4.1, 4.2, and 4.3, which illustrate that the spectrum can be rather complicated. In the remainder of this section we review certain limits where some analytical progress can also be made, which helps with physical understanding of these results.

$\gamma_3 = 0$ limit

It is simplest to consider the case where $\gamma_3 = 0$, which turns out to be an excellent approximation at large fields. When $\gamma_3 = 0$, the eigenstates of $\mathcal{H}^+$ fall

into one of three classes:

$$\left|\psi_{-1}\right\rangle = \begin{pmatrix} 0 \\ 0 \\ 0 \\ |0\rangle \end{pmatrix} \quad , \quad |\psi_0\rangle = \begin{pmatrix} 0 \\ v_0\,|0\rangle \\ \tilde{u}_0\,|0\rangle \\ \tilde{v}_1\,|1\rangle \end{pmatrix} , \tag{4.12}$$

and

$$|\psi_n\rangle = \begin{pmatrix} u_{n-1}\,|n-1\rangle \\ v_n\,|n\rangle \\ \tilde{u}_n\,|n\rangle \\ \tilde{v}_{n+1}\,|n+1\rangle \end{pmatrix} , \tag{4.13}$$

with $n \geq 1$. Clearly $\left|\psi_{-1}\right\rangle$ is an eigenstate with eigenvalue $E = U$. Applying $\mathcal{H}^+$ to $|\psi_0\rangle$, one obtains the 3×3 Hamiltonian for the ψ_0 sector,

$$H_0 = \begin{pmatrix} -U + \Delta' & \gamma_1 & \eta_4\,\omega_0 \\ \gamma_1 & U + \Delta' & -\omega_0 \\ \eta_4\,\omega_0 & -\omega_0 & U \end{pmatrix} . \tag{4.14}$$

Finally, the spectrum for the $|\psi_n\rangle$ states ($n \geq 1$) is given by the eigenvalues of the 4×4 Hamiltonian

$$H_n = \begin{pmatrix} -U & -W_n & \eta_4 W_n & 0 \\ -W_n & -U + \Delta' & \gamma_1 & \eta_4 W_{n+1} \\ \eta_4 W_n & \gamma_1 & U + \Delta' & -W_{n+1} \\ 0 & \eta_4 W_{n+1} & -W_{n+1} & U \end{pmatrix} , \tag{4.15}$$

where

$$W_n \equiv \sqrt{n}\,\omega_0\,. \tag{4.16}$$

To label the states, it is helpful to consider the case $\gamma_3 = \gamma_4 = \Delta' = U = 0$, corresponding to a pure nearest-neighbor hopping model with constant (zero) local site energies. One then finds the following (valley-degenerate) spectrum:

$$\mathcal{E}_{-1} = \mathcal{E}_0 = 0\,, \quad \mathcal{E}_{0,s_1,+} = s_1\gamma_1\sqrt{1+\beta}\,, \tag{4.17}$$

$$\mathcal{E}_{n,s_1,s_2} = s_1\gamma_1\sqrt{\frac{1}{2} + \left(n + \frac{1}{2}\right)\,\beta + s_2 C_n}\,, \tag{4.18}$$

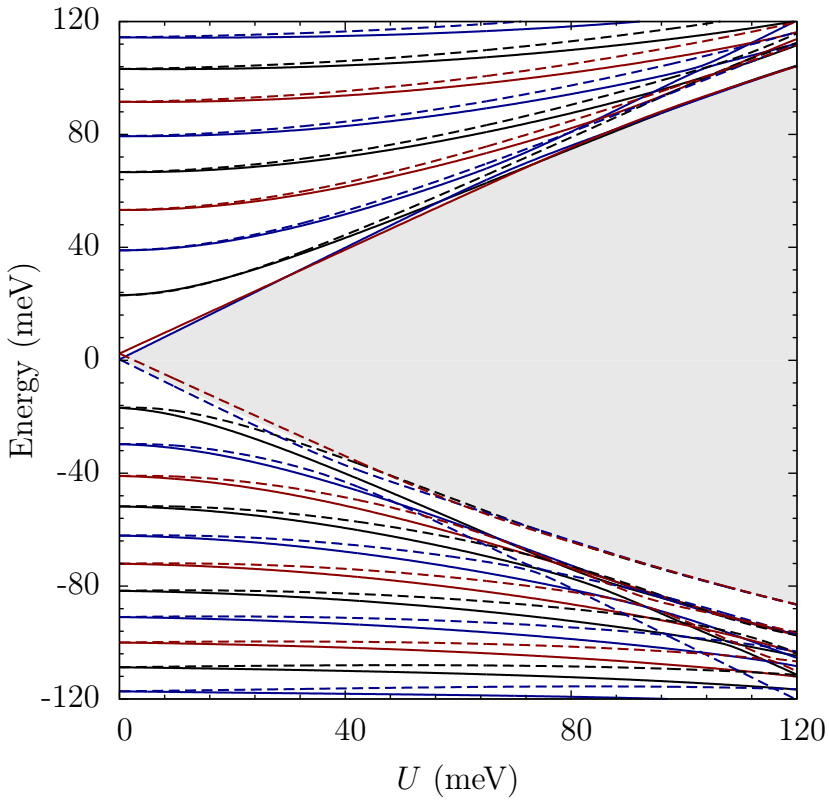

Figure 4.3: Landau level energies *vs.* interlayer bias U for a field value $B = 5\,\mathrm{T}$. Solid lines correspond to the K^+ valley and broken lines to the K^- valley. The color distinguishes the spectra of $\mathcal{H}_\mathrm{a}$ (black), $\mathcal{H}_\mathrm{b}$ (red), and $\mathcal{H}_\mathrm{c}$ (blue). At an accidental degeneracy (level crossing), the color and the line type cannot both be identical. The shaded area indicates the energy gap at $B = 0$.

where

$$\beta = \left(\frac{\omega_0}{\gamma_1}\right)^2 = \frac{B}{136\,\mathrm{T}} \tag{4.19}$$

and

$$C_n = \sqrt{\frac{1}{4} + \left(n + \frac{1}{2}\right)\,\beta + \frac{1}{4}\beta^2}\,. \tag{4.20}$$

Note that the $n = -1$ and $n = 0$ states require a separate labeling convention.

For the full model, with γ_3, γ_4, and Δ' restored, particle-hole symmetry is broken by the γ_4 and Δ' terms. These are relatively small however, so there remains an approximate particle-hole symmetry, as shown in Fig. 4.3. The state labels are then defined by adiabatic continuity with the $\gamma_3 = \gamma_4 = \Delta' = 0$ limit.

Low energy effective theory

As mentioned above, at low energies one can implement a unitary transformation, which decouples the inner ($s_2 = -1$) and outer ($s_2 = +1$) bands order by order in S, which vanishes at the zone corners. [26, 27] Here $S = \mp(\sqrt{3}/2)a_0(k_x \mp ik_y)$ and the upper (lower) sign denotes the K^+ (K^-) valley. To order S^2 one obtains

$$\widetilde{H} = \begin{pmatrix} \lambda\big(\widetilde{\Delta} + 2U\big)\, SS^\dagger - U & \gamma_3 S^\dagger - \dfrac{\gamma_0^2}{\gamma_1}\, S^2 \\ \\ \gamma_3 S - \dfrac{\gamma_0^2}{\gamma_1}\, S^{\dagger 2} & \lambda\big(\widetilde{\Delta} - 2U\big)\, S^\dagger S + U \end{pmatrix}, \tag{4.21}$$

where $\lambda = (\gamma_0/\gamma_1)^2 \approx 53.5$ and

$$\widetilde{\Delta} = \Delta' + \frac{2\gamma_1\gamma_4}{\gamma_0} \approx 59\,\mathrm{meV} \tag{4.22}$$

is a composite parameter describing electron-hole symmetry breaking effects of Δ' and γ_4. Anticipating the introduction of an external magnetic field, we have allowed for the possibility that S and $S^\dagger$ do not commute, cf. Appendix 4.7.1 for derivation.

The eigenvalues of $\widetilde{H}$ to leading order in γ_3 are [2]

$$\begin{aligned}\widetilde{E}^{\pm}_{s_1,-,\mathbf{k}} &= \frac{\varepsilon_k^2}{\gamma_1^2}\,\widetilde{\Delta} \\ &\quad + s_1\sqrt{\left(\frac{2\varepsilon_k^2}{\gamma_1^2}-1\right)^2 U^2 + \frac{\varepsilon_k^4}{\gamma_1^2} \pm \frac{2\gamma_3\,\varepsilon_k^3}{\gamma_0\gamma_1}\cos 3\varphi}\,,\end{aligned} \tag{4.23}$$

where φ is the polar angle of $\mathbf{k}$. This agrees with Eq. (1.14) in the appropriate limit.

The 2×2 form of matrix $\widetilde{H}$ in Eq. (4.21) naturally leads to the concept of a pseudospin-$\frac{1}{2}$ degree of freedom which simplifies calculations somewhat. We use this approach sparingly for the following reasons. First, in experiments U is not necessarily much smaller than γ_1, in which case the reduction to a two-band effective Hamiltonian is not valid. Second, the calculation of the pseudospin-related effects are not difficult even when all four bands are kept. Finally, the low-energy theory does not produce accurate results for the Berry phase. A brief discussion of this technical issue is also given in Appendix 4.7.1.

In a nonzero magnetic field, $\widetilde{H}^{+}$ becomes

$$\begin{pmatrix} \beta\big(\widetilde{\Delta}+2U\big)\,aa^\dagger - U & \dfrac{\gamma_3}{\gamma_0}\,\omega_0\,a^\dagger - \beta\gamma_1 a^2 \\ \dfrac{\gamma_3}{\gamma_0}\,\omega_0\,a - \beta\gamma_1 a^{\dagger 2} & \beta\big(\widetilde{\Delta}-2U\big)\,a^\dagger a + U \end{pmatrix}, \tag{4.24}$$

while $\widetilde{H}^{-}$ is obtained via substitutions (4.6). When $\gamma_3 = 0$, their eigenvalues are easily obtained by considering the basis of states

$$\left|\phi_n^+\right\rangle = \begin{pmatrix} u_n^+\,|n-1\rangle \\ v_n^+\,|n+1\rangle \end{pmatrix}. \tag{4.25}$$

In this basis the above Hamiltonian takes the form

$$\begin{pmatrix} \beta\,(\widetilde{\Delta}+2U)\,n - U & -\beta\gamma_1\sqrt{n(n+1)} \\ -\beta\gamma_1\sqrt{n(n+1)} & \beta\,(\widetilde{\Delta}-2U)(n+1)+U \end{pmatrix}. \tag{4.26}$$

[2] This is similar to Eq. (16) of Ref. [27] except in lieu of our $\cos 3\varphi$ they have $-\cos 3\phi = \sin 3\varphi$.

When $n = -1$, we have $u_{-1}^{+} = 0$ and the energy levels in the two valleys are $\mathcal{E}_{-1}^{\pm} = \pm U$. With $n = 0$ we again have $u_0^{+} = 0$, and

$$\widetilde{\mathcal{E}}_0^{\pm} = \beta\widetilde{\Delta} \pm (1 + 2\beta)U \,. \tag{4.27}$$

The splitting of the $n = -1$ and $n = 0$ levels and their valley-dependent slope as a function of U lead to a characteristic diamond-shaped crossing pattern, shown in Fig. 4.4. The largest energy gap occurs in the unbiased sample, $U = 0$, and its magnitude $\approx 0.5\,\mathrm{meV} \times B(\mathrm{T})$ is comparable to that measured in Ref. [87] in a suspended BLG. On the other hand, an order of magnitude smaller gaps (smaller than even the bare Zeeman gap) have been observed in a more disordered BLG on SiO_2 substrate. [88]

Finally, for $n > 0$ one has (similar to Ref. [110])

$$\begin{aligned}\widetilde{\mathcal{E}}_{n,s_1,-}^{\pm} = &\left(n + \frac{1}{2}\right)\beta\widetilde{\Delta} \mp \beta U \\ &+ s_1\sqrt{\left[(2n+1)\beta U \mp \frac{\beta\widetilde{\Delta}}{2} - U\right]^2 + n(n+1)\,\beta^2\gamma_1^2} \,.\end{aligned} \tag{4.28}$$

This completes our summary of the (mostly) known analytic results for the energy spectrum of BLG.

4.3 Quasiclassical approximation

4.3.1 Effective g-factor

Renormalization of the electron magnetic moment is a well-known phenomenon in the solid-state physics. Most often it comes from spin-orbit interaction; however, in crystals without inversion symmetry there is an additional contribution due to the orbital angular momentum:

$$\mathbf{M}_\alpha \equiv \langle\alpha\,|\mathbf{M}|\,\alpha\rangle = -\frac{e}{2c}\,\langle\alpha|\,\mathbf{r}\times\mathbf{v}\,|\alpha\rangle \,. \tag{4.29}$$

Here α is a given Bloch state and $\mathbf{r}$, $\mathbf{v}$ are the position and velocity operators, respectively. Since we are not interested in the center-of-mass motion, in evaluating

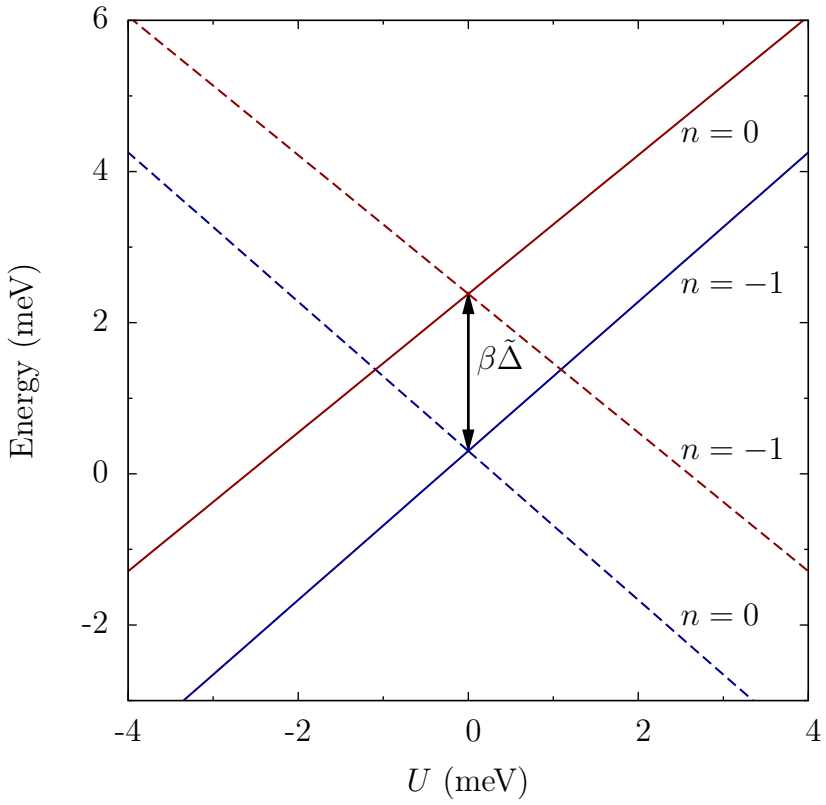

Figure 4.4: Landau levels -1 and 0 as a function of U at $B = 5\,\mathrm{T}$. The solid (dashed) lines correspond to K^+ (K^-) valley. The SWMc parameters are taken from Ref. [1].

$\mathbf{M}_\alpha$ we must assume that the expectation value of position vanishes, i.e., that $\mathbf{r}$ has only off-diagonal matrix elements [130]

$$\langle \alpha \left| \mathbf{r} \right| \alpha' \rangle = i \left\langle \alpha \left| \boldsymbol{\nabla}_k \right| \alpha' \right\rangle \,, \quad \alpha \neq \alpha' \,. \tag{4.30}$$

This leads to

$$\mathbf{M}_\alpha = \frac{e}{2ic} \sum_{\alpha' \neq \alpha} \left[\langle \alpha \left| \boldsymbol{\nabla}_k \right| \alpha' \rangle \times \langle \alpha' \left| \mathbf{v} \right| \alpha \rangle \right] \,. \tag{4.31}$$

A lucid derivation of Eq. (4.31) was given previously in Refs. [131, 132], which also contain references to much earlier work. [3]

Below we assume that $\mathbf{B}$ and $\mathbf{M}$ are both in the $\hat{\mathbf{z}}$-direction. The orbital contribution to the g-factor is $g = 2M_\alpha/\mu_\mathrm{B}$ where $\mu_\mathrm{B} = e\hbar/(2m_\mathrm{e}c)$ is the Bohr magneton and m_e is the bare electron mass. To calculate M_α, we can add and subtract the omitted diagonal term in Eq. (4.31), which gives

$$M_\alpha = \frac{e}{2c} \left(F_\alpha - D_\alpha \right) , \tag{4.32}$$

where

$$F_\alpha = -i \left\langle \alpha \left| \boldsymbol{\nabla}_k \times \mathbf{v} \right| \alpha \right\rangle \cdot \hat{\mathbf{z}} \,, \tag{4.33}$$

$$D_\alpha = -i \left[\langle \alpha | \, \boldsymbol{\nabla}_k \, | \alpha \rangle \times \mathbf{v}_\mathrm{g} \right] \cdot \hat{\mathbf{z}} \,, \tag{4.34}$$

(note that both F_α and D_α are real) and where

$$\mathbf{v}_\mathrm{g} \equiv \langle \alpha | \, \mathbf{v} \, | \alpha \rangle = \hbar^{-1} \boldsymbol{\nabla}_k \, E_\alpha \tag{4.35}$$

is the group velocity vector (the subscript α in $\mathbf{v}_\mathrm{g}$ is omitted for simplicity). Using these formulas we compute the energy dispersion

$$\widetilde{E}_\alpha = E_\alpha - B M_\alpha \,. \tag{4.36}$$

It is interesting to compare our formula with those in literature. A very close analogy is provided by Bi, whose effective Hamiltonian is also a 4×4 matrix linear in $\mathbf{k}$. In an early paper [107] where the calculation of the g-factor of Bi is

[3] Unfortunately, some of these sources also contain typographic mistakes. For example, Eq. (59.11) of Ref. [130] is off by the factor of $m\hbar$ and Eq. (3.6) of Ref. [132] is missing a factor of two.

discussed, the subtraction of the diagonal term D_α is lacking, so that the result is not gauge-invariant. Below we show that D_α is related to the Berry phase, which apparently has not been handled correctly in Ref. [107] (considering that it precedes Berry's work [99] by almost two decades, it is hardly surprising).

Let us now apply our general formula to BLG. For K^+ valley we can choose the eigenvectors of H^+ in the form

$$\left|\alpha^+\right\rangle = (u_\alpha e^{-i\varphi},\, v_\alpha\,,\, \tilde{u}_\alpha\,,\, \tilde{v}_\alpha\, e^{i\varphi})^{\mathsf{T}}, \tag{4.37}$$

where α now throughout this section stands for $\{s_1, s_2, k\}$. It is assumed that the imaginary parts and the entire dependence on φ — the polar angle of $\mathbf{k}$ — enter via the exponential factors only. A straightforward calculation yields:

$$D_\alpha^+ = v_{\mathrm{g}}\,\frac{u_\alpha^2 - \tilde{v}_\alpha^2}{k} = -\frac{v_{\mathrm{g}} U}{2kE_\alpha}\left(1 + \frac{4\varepsilon^2 - \gamma_1^2}{2s_2\Lambda^2(\varepsilon_k)}\right), \tag{4.38}$$

$$F_\alpha^+ = 2\,v_0\,\frac{u_\alpha v_\alpha - \tilde{u}_\alpha\tilde{v}_\alpha}{k} - D_\alpha^+ = -\frac{2\hbar\, v_0^2\, U}{s_2\Lambda^2(\varepsilon_k)} - D_\alpha^+\,, \tag{4.39}$$

where Λ is given by Eq. (1.15). The eigenvectors for K^+ valley can be obtained by replacing $e^{\pm i\varphi}$ in Eq. (4.37) with $-e^{\mp i\varphi}$ and so the signs of F_α and D_α are reversed.

The last term represents the pseudo-Zeeman effect due to the orbital magnetic moment. Algebraic manipulations with Eqs. (1.15), (4.32), (4.38), and (4.39), together with the relations

$$v_{\mathrm{g}} = \frac{1}{\hbar}\frac{dE}{dk} = v_0\,\frac{\varepsilon}{E}\,\frac{s_3\Gamma^2(E)}{s_2\Lambda^2(\varepsilon)} \tag{4.40}$$

and

$$s_3\Gamma^2(E_\alpha) - s_2\Lambda^2(\varepsilon_k) = \frac{1}{2}\gamma_1^2 + 2U^2\,, \tag{4.41}$$

yields

$$M_\alpha^+ = -\frac{e\hbar}{c}\,\frac{2v_0^2\gamma_1^2\, U}{\gamma_1^4 + 4(\gamma_1^2 + 4U^2)\,\varepsilon_k^2}\left(1 - \frac{\varepsilon_k^2}{E_\alpha^2}\right). \tag{4.42}$$

For the lower energy conduction band, on which we mostly focus later, $M_{+-,k}^+$ is plotted in Fig. 4.5. The modified spectrum $\widetilde{E}_\alpha$ is plotted alongside E_α in Fig. 1.3 for all four bands and in Fig. 4.6 for the lower conduction band only. At $k = 0$ we have a particularly simple result

$$g_{s_1,s_2,0}^{\pm} = \frac{2}{\mu_{\mathrm{B}}}\,M_{s_1,s_2,0}^{\pm} = \mp 8 m_{\mathrm{e}} v_0^2\,\frac{U}{\gamma_1^2}\,, \tag{4.43}$$

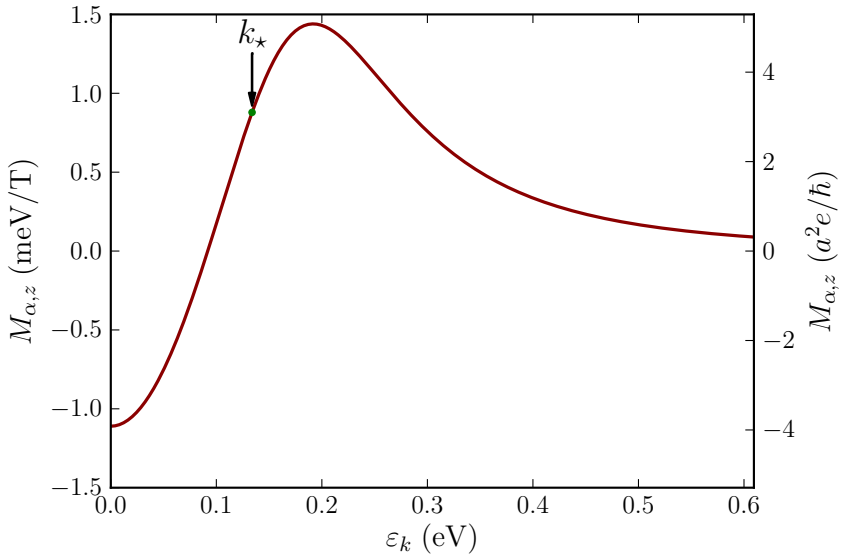

Figure 4.5: Orbital magnetization M^+_{+-} of K^+ valley as a function of $\varepsilon_k = \hbar v_0 k$ at $U = 0.1\,\mathrm{eV}$.

for all s_1 and s_2, in agreement with Eq. (54) of Ref. [105].

As one can see from Fig. 4.5, the g-factor has an intriguing energy dependence, which prompts the question of whether it can be verified experimentally. Unfortunately, this appears problematic. There is no optical transition between the energy levels split by the pseudo-Zeeman effect as they belong to different valleys, and so, methods analogous to the electron spin resonance would not work. Another conventional method of extracting the g-factor would be to measure the valley-splitting of the Shubnikov-de Haas effect. However, this splitting also includes the contribution of the Berry phase, discussed later in this Section. This contribution effectively compensates for nonmonotonic variation of the g-factor, making the valley-splitting of Landau levels only weakly dependent on the Fermi energy (or Landau level index).

The most easily observable manifestation of the pseudo-Zeeman effect appears to be the displacement of the band edges, e.g., the bottom of the Mexican hat of the conduction band. At this point, Eq. (4.42) yields (the superscript denotes

the valley, as usual):

$$g^{\pm}_{+-,k_\star} = \frac{2}{\mu_{\mathrm{B}}} M^{\pm}_{+-,k_\star} = \pm\frac{8m_{\mathrm{e}}v_0^2 U}{\gamma_1^2 + 4U^2}\,. \tag{4.44}$$

Thus, at $U = 100\,\mathrm{meV}$ we obtain $|g^{\pm}_{+-,k_\star}| \approx 22$. This is one order of magnitude higher than the bare value $g = 2$ and is about as large [107] as in Bi. (For this reason, we neglect the bare Zeeman coupling in this article.) For $U \ll \gamma_1$, the effective g-factor is proportional to U, as appropriate for the linear magnetoelectric coupling [Eq. (4.1)]. Therefore, a roughly linear variation of the band edge positions with B and U can be expected. This issue is addressed in more detail in Sec. 4.4.

4.3.2 Quantization rules

While numerical calculations of the Landau level spectrum is possible for any choice of parameters, in Sec. 4.4 we shall see that the result can be rather complicated. Therefore, both exact and approximate analytical methods remain valuable for this task in hand. So far, we have discussed two such methods. First, for $U = \gamma_4 = \Delta' = 0$, closed-form expressions for the Landau level energies [Eq. (1.15)] exist. Second, if these energies are much smaller than γ_1, then the approximate Eq. (4.28), valid for finite U, can be used. In this section we outline another approach — the quasiclassical quantization — which can be used for arbitrary relation between U and γ_1. Within this approximation, Landau level energies $\mathcal{E}^{\pm}_{n,s_1,s_2}$ are taken to be equal to the renormalized band energies (4.36) evaluated at certain quantized orbits in the reciprocal space:

$$\mathcal{E}^{\pm}_{n,s_1,s_2} = E^{\pm}_{s_1,s_2,k_n^{\pm}}\,. \tag{4.45}$$

The area of the nth orbit satisfies the Onsager condition [133]

$$\pi(k_n^{\pm}\ell_B)^2 = 2\pi(n + \delta_n^{\pm})\,, \tag{4.46}$$

where $k_n^{\pm}$ is the radius of the orbit and $\delta_n^{\pm}$ is a dimensionless number discussed below.

The quasiclassical approximation is accurate through the order $\mathcal{O}(\ell_B^{-2})$ or alternatively $\mathcal{O}(1/n)$. It turns out to be exact for parabolic dispersion (where $\delta = \frac{1}{2}$) and in monolayer graphene (where $\delta = 0$). The quasiclassical approximation for general matrix Hamiltonians was previously studied in Refs. [134, 135] and specifically in the context of graphene in Ref. [136]. However, we found it most instructive to follow Refs. [131, 137].

The physical picture is as follows. In a weak magnetic field, momentum $\mathbf{k}$ of a quasiparticle slowly rotates as a function of time t according to the equation of motion

$$\dot{\mathbf{k}} = \omega_{\rm c}\, \hat{\mathbf{z}} \times \mathbf{k} \quad , \quad \omega_{\rm c} \equiv \frac{2\pi}{T}\, \mathrm{sgn}(v_{\rm g})\,, \tag{4.47}$$

where $T = 2\pi k_n \ell_B^2/|v_{\rm g}(k_n)|$ is the cyclotron period. (For simplicity, the valley and band labels are temporarily omitted.) The rotation of $\mathbf{k}$ causes a slow evolution of the wavefunction $|\alpha\rangle$ in the pseudospin, i.e., sublattice space. This causes the accumulation of the Berry phase [99, 100]

$$\Phi_{\rm B} \equiv \mathrm{sgn}(v_{\rm g}) \int_0^T dt\ \langle \alpha\, |i\boldsymbol{\nabla}_k|\, \alpha\rangle \cdot \dot{\mathbf{k}}\,. \tag{4.48}$$

The quasiclassical quantization rule is [131]

$$\begin{aligned} \mathrm{sgn}(v_{\rm g}) \oint d\pi_y\, \ell_B^2\, \pi_x + \Phi_{\rm B} &= \pi (k_n \ell_B)^2 + \Phi_{\rm B} \\ &= (2n+1)\pi\,. \end{aligned} \tag{4.49}$$

It can be understood as a generalized Bohr-Sommerfeld rule: since $\ell_B^2\, \pi_x$ plays the role of "momentum" conjugate to the "coordinate" π_y, the top line represents the total phase shift acquired along the orbit, including the geometric phase. Equation (4.49) establishes the precise relation between the Onsager number δ and the Berry phase $\Phi_{\rm B}$:

$$\delta = \frac{1}{2} - \frac{\Phi_{\rm B}}{2\pi}\,, \tag{4.50}$$

Thus, in monolayer graphene where $\Phi_{\rm B} = \pi$, we get $\delta = 0$, which implies the existence of a level at zero energy. [25]

Comparing Eqs. (4.34) and (4.48) we see that for the isotropic spectrum (in BLG, for $\gamma_3 = 0$) we have

$$\Phi_{\rm B} = \frac{2\pi k}{v_{\rm g}}\, D_\alpha\,. \tag{4.51}$$

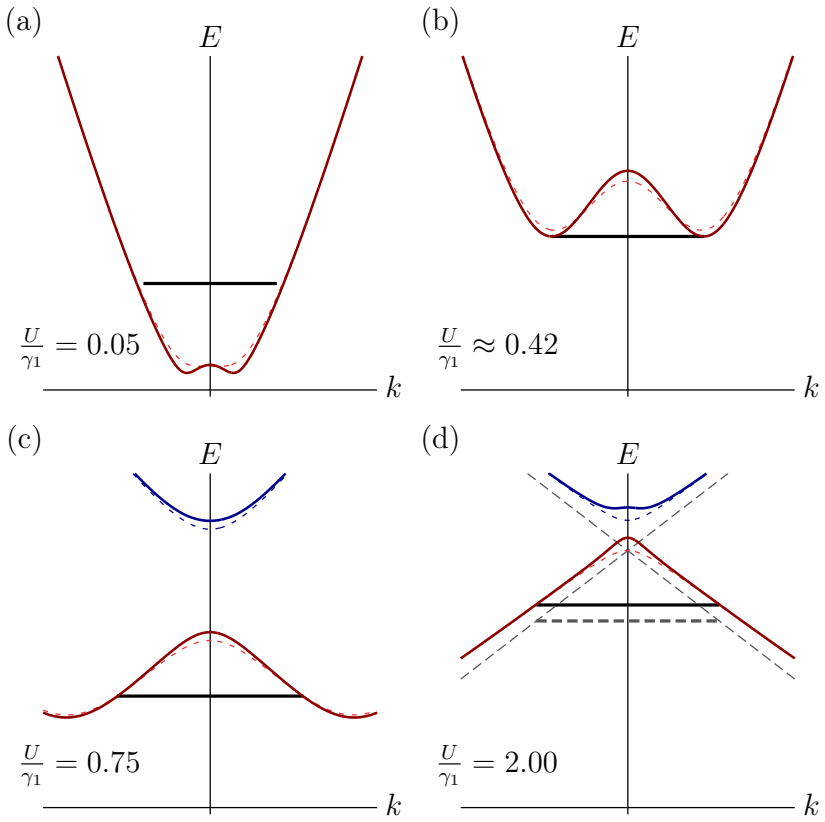

Figure 4.6: Evolution of a particular ($n = 5$) Landau level of the K^+ valley as a function of U. Superimposed are the spectra at zero field (thin traces) and that with pseudo-Zeeman correction in a magnetic field $B = 5\,\mathrm{T}$ (thick trace). (a) At small U, the quantized cyclotron orbit is outside the Mexican hat. (b) For certain U, the orbit goes inside the gap of the zero field spectrum. (c) At larger U, it moves underneath the Mexican hat where the direction of the group velocity is opposite to the momentum. (d) At very large U (not presently accessible in experiments), where the BLG spectrum consists of two copies of monolayer spectra shifted by $\pm U$, the n^{th} electron Landau level of BLG approaches the $(n+1)^{\mathrm{th}}$ hole Landau level of the higher energy monolayer.

Postponing the discussion of this equation for just a moment we note that for $v_{\rm g} \neq 0$, another version of the quantization rule can be established. [137] To this end one defines a modified orbit radius $\widetilde{k}_n$ such that

$$\mathcal{E}_{n,s_1,s_2} = E_{s_1,s_2,\widetilde{k}_n} \,. \tag{4.52}$$

To the leading order in B, the rule that determines $\widetilde{k}_n$ is similar to Eq. (4.49) except $\Phi_{\rm B}$ is replaced by a different phase shift $\Phi_{\rm c}$:

$$\pi\big(\widetilde{k}_n \ell_B\big)^2 = (2n+1)\,\pi - \Phi_{\rm c}\,, \tag{4.53}$$

$$\Phi_{\rm c} = \Phi_{\rm B} + \frac{MB}{\hbar}\,T = \frac{\pi k}{v_{\rm g}}\big(F_\alpha + D_\alpha\big)\,. \tag{4.54}$$

With further analysis it is possible to show that our $\Phi_{\rm c}$ coincides with the "semiclassical phase" defined in Ref. [136]. Therefore, the difference between $\Phi_{\rm c}$ and $\Phi_{\rm B}$ noted in that paper is entirely due to the pseudo-Zeeman shift rather than a violation of adiabaticity.

Applying the above formulas to BLG, we obtain

$$\frac{\Phi_{\rm B}^{\pm}}{2\pi} = \mp\,\frac{U}{2E_\alpha}\left(1 + s_2 \frac{4\varepsilon_k^2 - \gamma_1^2}{\sqrt{\gamma_1^4 + 4(\gamma_1^2 + 4U^2)\,\varepsilon_k^2}}\right). \tag{4.55}$$

At finite U the Berry phase is a nonmonotonic function of momentum, which is addressed in more detail in Sec. 4.5. Here we comment only on the simple case $U = 0$, where Eq. (4.55) gives $\Phi_{\rm B}^{\pm} = 0$ at all $k \neq 0$. This seems to contradict to the assignment $\Phi_{\rm B}^{\pm} = \pm 2\pi$ made in most of the previous work. [26, 89] In fact, there is no contradiction because the Berry phase is not unique: different choices for an overall phase of the wavefunction in Eq. (4.48) can shift $\Phi_{\rm B}^{\pm}$ by an arbitrary integer multiple of 2π. In the context of Landau quantization, such shifts can be compensated by relabeling the Landau index n, so that the physical quanitities — the radii $k_n^{\pm}$ of the orbits and their energies — remain the same.

Combining Eqs. (4.54) and (4.55), we obtain the analytic formula for the semiclassical phase:

$$\frac{\Phi_{\rm c}^{\pm}}{2\pi} = \mp\, s_3\,\frac{UE_\alpha}{\sqrt{(\gamma_1^2 + 4U^2)E_\alpha^2 - \gamma_1^2\,U^2}}\,, \tag{4.56}$$

This equation should be used away from momentum $k_\star$ where its denominator vanishes. Finally, the quantization rule (4.53) becomes

$$n + \frac{1}{2} = \left(\frac{\varepsilon_k}{\omega_0}\right)^2 + \frac{\Phi_c}{2\pi}\,. \tag{4.57}$$

In comparison, the precise relation between n and $\mathcal{E}_\alpha$ for the case $\gamma_3 = \gamma_4 = \Delta' = 0$ reads

$$n + \frac{1}{2} = \frac{\mathcal{E}_\alpha^2 + U^2}{\omega_0^2} - s_3\sqrt{\frac{\Gamma^4(\mathcal{E}_\alpha)}{\omega_0^4} + \frac{2\,U\mathcal{E}_\alpha}{\omega_0^2} + \frac{1}{4}}\,. \tag{4.58}$$

This result follows from Eq. (4.18); the composite label α denotes the set $\{n, s_1, s_2\}$. The semiclassical Eq. (4.57) does agree with the exact Eq. (4.58) to the leading order in ω_0^2, i.e. $\mathcal{O}(1/n)$ at large n. Fortuitously, it is also valid for $n = -1$. It predicts $\widetilde{k}^+_{1--} = 0$, which entails $\mathcal{E}^+_{1--} = U$, in agreement with our earlier result.

The valley splitting of the Landau levels can be expressed as follows:

$$\mathcal{E}^+_\alpha - \mathcal{E}^-_\alpha = -\frac{2\hbar}{T}\,\Phi^+_c = s_1 s_2 \frac{2\gamma_1^2\beta U}{\sqrt{\gamma_1^4 + 4(\gamma_1^2 + 4U^2)\,\varepsilon_k^2}}\,. \tag{4.59}$$

Here either $k_n^\pm$ or $\widetilde{k}_n^\pm$ can be used in place of k because this formula is valid only to the leading order in β. At low energies, it simplifies to

$$\mathcal{E}^+_\alpha - \mathcal{E}^-_\alpha \simeq -2\beta U\,, \quad n \gg 1\,, \tag{4.60}$$

in agreement with Eq. (4.28). We see that unlike the pseudo-Zeeman term, discussed in Sec. 4.3.1, the net valley-splitting of the Landau levels has little energy or n dependence.

It is now straightforward to apply the above quantization rules in order to understand qualitatively the evolution of some $n \gg 1$ Landau level as a function of U. For the K^+ valley, illustrated in Fig. 4.6, the situation is as follows. As U increases starting from zero, the radius of the orbit changes only slightly because $\Phi_B/2\pi \sim 1 \ll n$ for all U. On the other hand, the Mexican hat expands in both height (energy) and width (momentum). As a result, the quantized orbit slips from the exterior ($k > k_\star$) to the interior ($k < k_\star$) of the hat. In the process, the orbit passes through a region where its energy is inside the gap of the $B = 0$ dispersion because of the negative pseudo-Zeeman term. (For the K^+ valley this occurs only

if $U > 0$ but not if $U < 0$, see Eq. (4.44) and Sec. 4.4 below.) Eventually, at very large U, the orbit approaches the $n+1$st hole Landau level of graphene monolayer, except it is shifted upward by U.

4.4 Landau level spectrum

4.4.1 Level crossings

Figure 4.7 shows the first several Landau levels, which we calculated numerically as a function of U at a representative magnetic field of $B = 5\,\mathrm{T}$. Only $U > 0$ are shown because the energies at negative U can be obtained from the symmetry relation $\mathcal{E}_\alpha^+(U) = \mathcal{E}_\alpha^-(-U)$.

As more clearly seen in Fig. 4.14, the U-dependence of Landau level energies is nonmonotonic, which gives rise to a complicated net-like pattern with numerous crossings. In this section we explain the physical origin of these crossings. It should be clarified that electron interactions, which are ignored in our calculations, can produce significant corrections to the Landau level energies. However, we expect that topological properties of the level diagram would not change much.

Let us focus on the $s_1 = +1$ levels and consider the limits of small and large U (a similar argument can be applied to the $s_1 = -1$ levels with appropriate sign changes). For small U, the Landau levels are roughly equidistant and those with higher index n have higher energies (in agreement with Eq. (4.18) for $U = 0$). In the opposite limit of $U \gg \gamma_1$, from Eq. (4.4) it is easy to see that the BLG spectrum consists of two copies of the monolayer spectrum shifted by $\pm U$. Accordingly, the set $\left\{\mathcal{E}_{n+-}^{\pm}\right\}$ approaches the Landau level energies of the holes in the monolayer [25], but shifted by $U > 0$:

$$\mathcal{E}_{n+-}^{+} \simeq U - \sqrt{n+1}\,\omega_0 \quad , \quad \mathcal{E}_{n+-}^{-} \simeq U - \sqrt{n}\,\omega_0\,. \tag{4.61}$$

In this limit states of higher index have lower energies. Therefore, any two levels of the $s_2 = -1$ band cross at some value of U. This occurs when the corresponding quantized orbits are located at the same energy but on the opposite sides of the Mexican hat (see Fig. 4.6).

In addition, it is possible to have crossings of orbits on the same side of the Mexican hat if they belong to opposite valleys. In the semiclassical approximation, this occurs whenever $\Phi_c^{\pm}/\pi$ is an integer. In this case the difference in n is compensated by the difference in the semiclassical phase, yielding the same momentum $\widetilde{k}_n$ and energy $E_{s_1,s_2}(\widetilde{k}_n)$ (see Eq. (4.53)). For example, at $U = 0$ we have $\Phi_c^{\pm} = 0$, so that all Landau levels should be (and are) valley-degenerate. Next, $|\Phi_c^{\pm}| \to \pi$ as $U \to \infty$, so in this limit the *adjacent* Landau levels coincide, in agreement with Eq. (4.61). Using Eqs. (1.17), (1.19), and (4.56), one can show that the condition $|\Phi_c^{\pm}| = N\pi$ is met at

$$\mathcal{E}_\alpha^2 = \frac{E_\star^2}{1 - (2E_\star/N\gamma_1)^2} \qquad (\gamma_3 = \gamma_4 = \Delta' = 0)\,. \tag{4.62}$$

This implies that the level crossings are confined to the range of energies $E_\star \leq |\mathcal{E}_\alpha| \leq |U|$, which is precisely the range between the top and the bottom of the Mexican hat. The crossings at the top of the hat are between the adjacent Landau levels ($N = 1$). Since the special level $\mathcal{E}_{-1}^{\pm} = \pm U$ also happens to be at the same energy, these are actually *triple* crossings. In the $s_1 = \pm 1$ band, they involve nth level of $K^{\pm}$, the $n-1$st level of $K^{\mp}$, and the -1 level of $K^{\pm}$ (assuming $U > 0$). When $\gamma_3 = \gamma_4 = \Delta' = 0$ these unusual triple crossings appear when $U = U_n \equiv \frac{1}{2}\sqrt{n}\,\omega_0$. We can show by algebraic means that finite γ_4 and Δ' give corrections to U_n but do not lift the triple degeneracies. We suspect that this property stems from some hidden symmetry of the Hamiltonians $\mathcal{H}_n^{\pm}$.

4.4.2 Trigonal warping

The parameter γ_3 has a number of interesting effects on both the zero-field and Landau level spectra. It mixes Landau levels of the same valley with indices n different by an integer multiple of three, see Appendix 4.7.2. This turns crossings between such levels into avoided crossings. Strictly speaking, we can no longer label Landau levels by $\{n, s_1, s_2\}$. Nevertheless, the effect of γ_3 is small at low U, so that with proper care it is possible to track the levels through the avoided crossings and still retain our labeling scheme. The calculation of the Landau level spectra with $\gamma_3 \neq 0$ is handled numerically. To account for the level mixing at

high U we had to diagonalize matrices of size $4J$ with large enough J ($J \approx 100$) to ensure numerical accuracy, see Appendix 4.7.2. One effect of γ_3 is to lift the triple degeneracy of the adjacent Landau levels by moving the crossing point energy away from the top of the Mexican hat, as expected.

A more interesting effect is the shift of the $B = 0$ band edges, which are the boundaries of the central band gap in Fig. 4.3. This can be understood as follows. The hopping γ_3 induces a trigonal warping of the zero-field bands, as described by Eq. (4.23). Accordingly, the low-energy region of the conduction band develops three kidney-shaped pockets along $k = k_\star$ circle centered, in K^+ valley, at $\varphi = \frac{1}{3}\pi$, π, and $\frac{5}{3}$ angular positions [4]. To the leading order in γ_3, their energy is lowered below $E_\star$ by

$$\delta E \simeq \frac{\sqrt{8}\,\gamma_3}{\gamma_0}\,\frac{U^2}{\gamma_1} \qquad \left(\frac{\gamma_3}{\gamma_0} \ll \frac{U}{\gamma_1} \ll 1\right), \tag{4.63}$$

which follows from Eqs. (4.23). Accordingly, the band edge of the conduction/valence band at $B = 0$ shifts by $\mp\delta E$. For example, at $U = 0.15\,\mathrm{eV}$ we obtain $\delta E \approx 8\,\mathrm{meV}$. This is in a good agreement the numerical results shown in Figs. 4.3 and 4.7.

The effect of γ_3 on Landau levels is even more striking. As one can see from Fig. 4.7, it leads to a bunching of Landau levels near the conduction (and valence) band edges as U increases above 0.1 eV. Apparently, these Landau levels, which can be labeled $n = n_\star - 1$, $n_\star$, and $n_\star + 1$, become nearly degenerate. Within a simple quasiclassical picture, the explanation is straightforward: this trio of levels correspond to three orbits, which are identical in shape and energy but are separately confined inside the three equivalent pockets. [26] In a more refined description, such orbits are hybridized by a weak quantum tunneling, so that the Bloch functions have equal amplitude in each pocket but different phases. To verify this picture, we chose a set of U in the range between 0 and 0.15 eV and for each of them computed the Bloch function of the lowest-energy state numerically. We took $\gamma_3 = 0.15$, for which there is only a single threefold degenerate level lying just within the central gap. At all U, these functions exhibit maxima centered at $\varphi = \frac{1}{3}\pi$, π, and $\frac{5}{3}\pi$, as expected (see Fig. 4.8). However, for $U \gtrsim 0.1\,\mathrm{eV}$ such

[4] This agrees with Fig. 6 of Ref. [27] where $\gamma_3 > 0$ is also assumed. In contrast, in Ref. [26] where the sign of γ_3 is opposite to ours, values of φ are shifted by π.

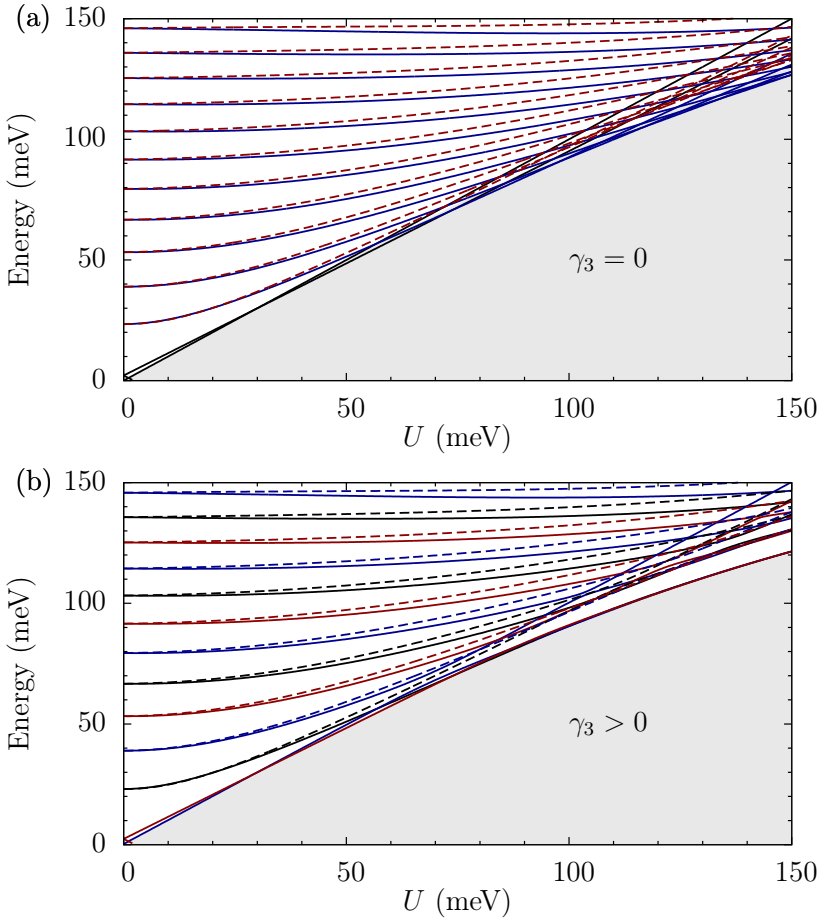

Figure 4.7: Landau level energies *vs.* interlayer bias U for a field value $B = 5\,\mathrm{T}$. (a) Top panel: $\gamma_3 = 0$; (b) bottom panel: $\gamma_3 = 0.3\,\mathrm{eV}$. The color and line type are as in Fig. 4.3. Note the bunching of levels at the edges of the central band gap when $\gamma_3 \neq 0$: the two levels just below the gap for $U \gtrsim 100\,\mathrm{meV}$ are both very nearly threefold degenerate.

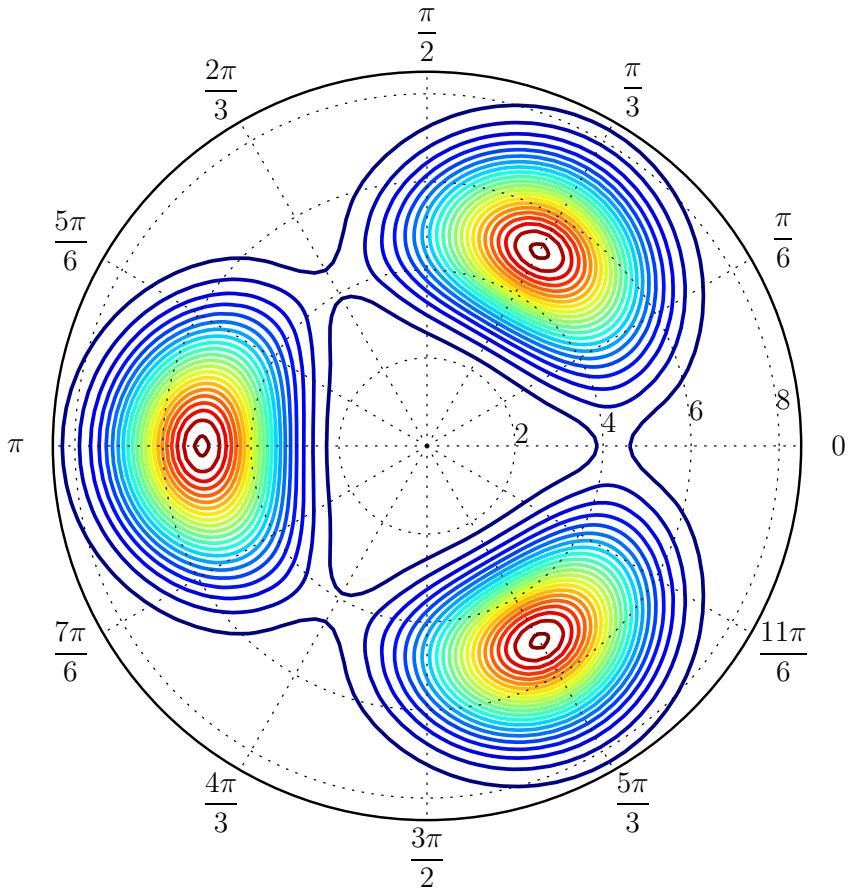

Figure 4.8: Absolute value of the Bloch function for the lowest-energy Landau level of the conduction band. The origin is at the K^+ point, the radial coordinate is $k\ell_B$, and $U = 0.15\,\text{eV}$.

maxima become very sharp, consistent with the picture of confinement and in concert with the coalescence of the energy levels into a single narrow bunch, as in Fig. 4.7.

In general, the influence of γ_3 on the spectrum gets stronger as B decreases or U increases. This is because the depth δE of the pockets and their width increases with U while the area in momentum space per orbit is equal to $2\pi/\ell_B^2 \propto B$, as discussed in Sec. 4.3. Hence, at large U and/or small B, each pocket may host several orbits, so that higher-energy Landau levels can also form bunches of three, as is apparent in Fig. 4.7, where there are two nearly three-fold degenerate sets of Landau levels separated by 10-20 meV from a tangle of higher energy states. The first bunch emerges at $U \approx 80\,\text{meV}$ and the second at $U \approx 120\,\text{meV}$. Conversely,

as B increases at fixed U, separate orbits no longer fit into the pockets and they unite into a single contiguous loop. At this point, the effect of γ_3 can safely be neglected.

4.4.3 Energy gap

The above discussion indicates that the energy gap of BLG can be controlled not only by U but also by B while keeping U fixed. Since this gap can strongly affect the low-temperature transport, it may be of interest in applications, and so it deserves some discussion. The magnetic field tends to reduce the gap relative to the zero-field case, as one can see in Figs. 4.3 and 4.7, where the gray area indicates the zero field gap. In other words, some Landau levels can reside *inside* the bandgap $|E| < E_\star$ of the $B = 0$ spectrum. This phenomenon is a direct manifestation of the pseudo-Zeeman shift. It is seen more clearly in Fig. 4.6(b), where only one Landau level (from the K^+ valley) is shown. For a certain $U > 0$ this level drops below the zero-field minimum $E_\star$ of the conduction band. Similarly, there is another Landau level from K^+ valley, not shown in the Fig. 4.6(b), which rises above the maximum $-E_\star$ of the valence band. This is because the pseudo-Zeeman effect has opposite signs in the two valleys. Based on this argument, we can use Eq. (4.44) to show that, e.g., the bottom of the conduction band shifts to

$$\widetilde{E}_\star \simeq E_\star - \frac{\beta\,|U|}{1 + (2U/\gamma_1)^2}\,, \tag{4.64}$$

where β is defined in Eq. (4.19). In principle, this approximate formula can be refined by semiclassical quantization. The true band edge is determined by the lowest-energy Landau level of the conduction band. Its index $n_\star$, which depends on U and B, can be found by setting $\widetilde{k} = k_\star$ and dropping the second term on the right-hand side of Eq. (4.57): $n_\star + \frac{1}{2} \simeq \varepsilon_\star^2/\omega_0^2 = (1/\beta)(\varepsilon_\star/\gamma_1)^2$. A similar result can be obtained from the low-energy effective theory, by minimizing the energy in Eq. (4.28) with respect to the Landau index n. With $\Delta' = 0$ we obtain

$$n_\star = \frac{1}{\beta}\,\frac{2U^2}{\gamma_1^2 + 4U^2}\,. \tag{4.65}$$

Since $\beta \propto B$, our approximate formula $2\widetilde{E}_\star^+$ for the gap predicts a linear gap narrowing as B increases at $U = \text{const}$. Figure 4.9 demonstrates that it is

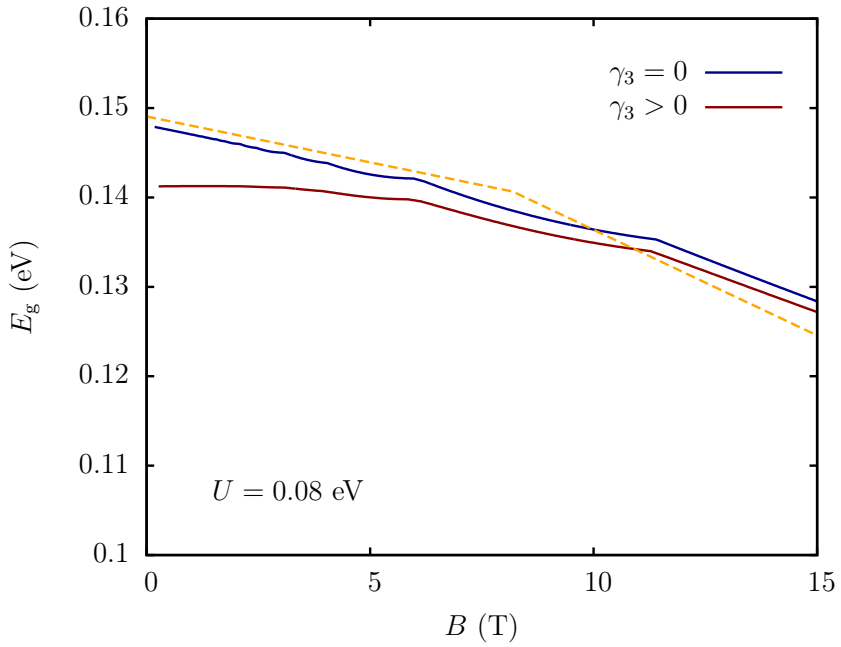

Figure 4.9: Energy gap separating Landau levels of the valence bands from those of the conduction band as a function of the magnetic field B. The cusps on the curves are due to discrete changes in Landau level index $n_\star$ (see main text). The upper solid curve is for $\gamma_3 = 0$ and the lower one for $\gamma_3 = 0.30\,\mathrm{eV}$. The analytic estimate per Eqs. (4.64) and (4.66) is shown by the dashed line.

quite accurate up to the point where $n_\uparrow$ drops to zero, i.e. up to the field where $\beta \approx 2U^2/\gamma_1^2$. Of course, this approximation misses the small cusps produced by the discrete changes in $n_\star$.

At larger B, the gap is determined by the energy of the special $n = 0$ Landau level for which Eq. (4.64) is not valid. Instead, we can use Eq. (4.27) to get

$$\widetilde{E}_\star \simeq E_\star - \left(2|U| - \widetilde{\Delta}\right)\beta \qquad (\beta < 2U^2/\gamma_1^2)\,. \tag{4.66}$$

We see that the B-dependence remains linear but the slope becomes larger by a factor of two or so. This prediction is in a reasonable agreement with numerical calculations (Fig. 4.9). The deviations seen at $B \gtrsim 10\,\mathrm{T}$ are due to insufficient accuracy of the low-energy theory at such fields. The total reduction of the gap as the field changes from $B = 0\,\mathrm{T}$ to $15\,\mathrm{T}$ is about $15\,\mathrm{meV}$ or 10%.

At even larger B, level $n = 0$ on the $s_1 = \mathrm{sgn}(U)$ side would cross with level $n = -1$, so that the slope of the linear dependence would change again. That $n = -1$ level would eventually intersect with the other $n = 0$ level if B keeps increasing, at which point the gap would momentarily vanish. An example of such an intersection is shown in Fig. 4.4 (although the energies are plotted as a function of U).

Let us now discuss the effect of γ_3. In Fig. 4.3, the energies of the lowest-energy levels of the conduction and its counterpart in the valence band seem to be lined up with the respective edges of the $B = 0$ spectrum, as though the pseudo-Zeeman effect is canceled. This cancellation is fortuitous. We attribute it to the zero point motion of the orbits confined inside the pockets. Clearly, the Bloch functions (Fig. 4.8) have some finite spread around the centers of the pockets. Thus, in the conduction band such orbits are raised in energy above the actual minima of the band, which counteracts the effect of the pseudo-Zeeman shift. Indeed, a better measure of the pseudo-Zeeman effect is the valley splitting, which is nearly the same in Figs. 4.7(a) and (b). (The latter is essentially the upper half of Fig. 4.3). The magnitude of the zero-point energy shift depends on U and B and just happens to be numerically close to the pseudo-Zeeman shift in a range of parameters used in Fig. 4.3.

The gap narrowing becomes more apparent at larger magnetic fields, see Fig. 12. The upper and the lower solid curves represent the energy gap without and with γ_3, respectively. At $B = 0$, the distance between the two curves is about 8 meV, which is close to $2\,\delta E \approx 9$ meV per Eq. (4.63). As B increases, this distance quickly diminishes, and the gap concomitantly narrows.

4.5 Anomalous Hall conductivity and valley magnetization

Systems that carry a finite Berry phase can exhibit a nonzero Hall conductivity $\sigma_{\rm H}$ even at $B = 0$. This is known as the anomalous Hall effect (AHE). The AHE and other manifestations of the Berry phase in electronic properties have been recently reviewed in Ref. [138]. It has been shown that for a partially filled band, $\sigma_{\rm H}$ in units of e^2/h is equal to the Berry curvature

$$\Omega \equiv [\boldsymbol{\nabla}_k \times \langle \alpha \,|i\boldsymbol{\nabla}_k| \,\alpha\rangle] \cdot \hat{\mathbf{z}}\,, \tag{4.67}$$

integrated over all occupied states. By the Stokes' theorem, in the two-dimensional case the result is determined solely by the Berry phase at the Fermi level. Therefore, we can readily compute the anomalous contribution to $\sigma_{\rm H}$ from our Eq. (4.55). To do so, we need the Berry phase as a function of energy. Substituting Eq. (4.41) into Eq. (4.55), we obtain

$$\frac{\Phi_{\rm B}^{\pm}}{2\pi} = \pm\frac{U}{E}\,\frac{2E^2 - \gamma_1^2 - 2s_3\mathit{\Gamma}^2(E)}{4U^2 + \gamma_1^2 - 2s_3\mathit{\Gamma}^2(E)}\,, \tag{4.68}$$

where $\mathit{\Gamma}(E)$ is defined in Eq. (1.19). The opposite signs in this formula indicate that the two valleys give opposite contributions to the AHE. Therefore, $\sigma_{\rm H}$ is nonzero only if unequal population of the valleys is created. While this occurs naturally for $B \neq 0$, we desire, in the context of the AHE, that it should also occur in the absence of an external magnetic field. Theoretical proposals for achieving that have been advanced in Refs. [139, 104, 140, 141]. Here we do not address any mechanisms of valley polarization but simply compute all the quantities for

K^+ valley only. Comparison with previous work will be given at the end of this section.

For brevity, we limit the consideration to the case where the Fermi level μ resides in the conduction bands ($s_1 = +$), i.e. $\mu > 0$. Using Eq. (4.55), we obtain:

$$\sigma_{\rm H} = \begin{cases} 0 & \mu < E_\star \,, \\ \bar{\sigma}_-(\mu) - \bar{\sigma}_+(\mu) & E_\star \le \mu < U \,, \\ \bar{\sigma}_-(\mu) - \bar{\sigma}_+(U) & U \le \mu < E_\diamond \,, \\ \bar{\sigma}_-(\mu) - \bar{\sigma}_+(U) + \bar{\sigma}_+(\mu) & E_\diamond \le \mu \,, \end{cases} \tag{4.69}$$

where

$$\bar{\sigma}_{s_3}(E) \equiv \frac{g_{\rm s} e^2}{h}\, \Phi^+_{\rm B}(s_3) \,, \tag{4.70}$$

$g_{\rm s} = 2$ is the spin degeneracy, and

$$E_\diamond \equiv E_{++}(k = 0) = \sqrt{\gamma_1^2 + U^2} \,. \tag{4.71}$$

Hence, $E_\star$, U, and $E_\diamond$ are the energies of the Mexican hat bottom, Mexican hat top, and the upper conduction band bottom, respectively. At these energies the topology of the Fermi surface changes: from two concentric circles to one and back to two (we ignore γ_3). Accordingly, $\sigma_{\rm H}(\mu, U)$ is nonanalytic at such energies: it has discontinuous derivative (cusps), which are marked by the dots in Fig. 4.10. Note that in the limit of small U, $\sigma_{\rm H}$ approaches the universal value of $2e^2/h$. This property is related to the 'double step' of the usual Hall conductivity at zero density (electroneutrality), which is a hallmark of the quantum Hall effect in a symmetric graphene bilayer. [25]

Another quantity we can easily compute is the total magnetization $\mathcal{M}$ of the K^+ valley. Recall that at finite U each state $\{s_1, s_2, \mathbf{k}\}$ carries the orbital magnetic moment $M^+_{s_1,s_2,\mathbf{k}}$. However, when computing the valley magnetization at given fixed μ, one must account for the pseudo-Zeeman contribution to the spectrum, which effectively modifies the density of states. The net result is that, in addition to summing the magnetic moment over the occupied states of the original spectrum, there is an additional contribution related to the Berry curvature. [104] Namely,

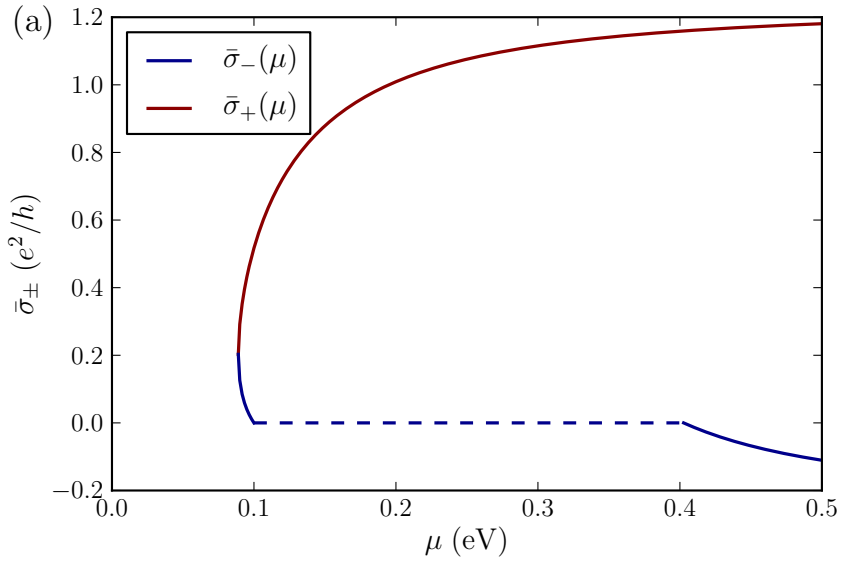

Figure 4.10: Berry phase [or more precisely, $\bar{\sigma}_{s_3}(E = \mu)$ of Eq. (4.68)] as a function of the Fermi energy μ. The upper (lower) curves correspond to $s_3 = \mp 1$. The solid curves in Fig. 4.10–4.12 are for $U = 0.1\,\text{eV}$ and only for K^+ valley. (The same quantities in the K^- valley are equal in magnitude but opposite in sign.)

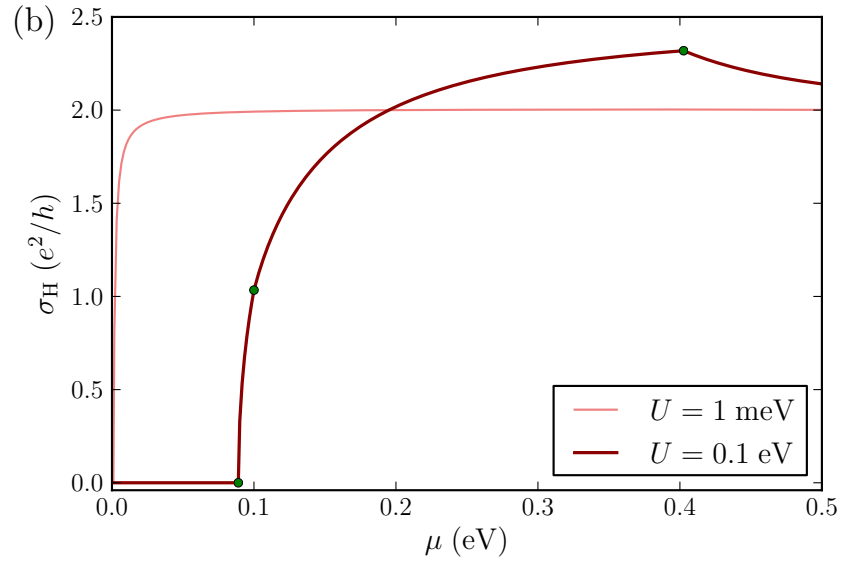

Figure 4.11: The anomalous Hall conductivity as a function of μ. The result for $U = 1\,\text{meV}$ is also shown by the dashed line. The dots mark the cusps that occur at the band extremities $\mu = E_\star$, U, and $E_\diamond$.

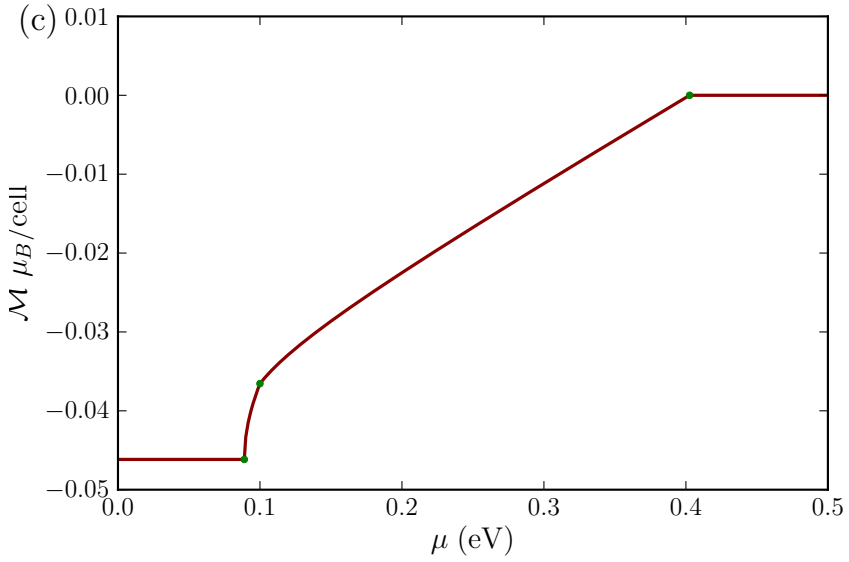

Figure 4.12: Total zero-field magnetization.

$\mathcal{M} = \mathcal{M}_M + \mathcal{M}_\Omega$, where

$$\mathcal{M}_M = g_\mathrm{s} \sum_{s_2,s_2} \int \frac{d^2k}{(2\pi)^2}\, M_\alpha\, \Theta\big(\mu - E_\alpha\big)\,, \tag{4.72a}$$

where $\alpha = \{s_1, s_2, \mathbf{k}\}$ is a composite index,

$$\mathcal{M}_\Omega = \frac{g_\mathrm{s} e}{\hbar c} \sum_{s_1,s_2} \int \frac{d^2k}{(2\pi)^2}\, (\mu - E_\alpha)_+\, \Omega_\alpha\,, \tag{4.72b}$$

where $F_+ \equiv F\,\Theta(F)$. Thus, for $\mu > U$, in which case the occupied states of both conductions bands fill a circle, the integration limits are from $k = 0$ to $k = k_{\mathrm{F},s_2}$ where

$$k_{\mathrm{F},s_2} = \frac{1}{\hbar v_0}\sqrt{\mu^2 + U^2 - s_2 \Gamma^2(\mu)}\,. \tag{4.73}$$

For $E_\star < \mu < U$, the occupied states fill an annulus in momentum space. The limits on k are from the inner radius $k_{\mathrm{F},+}$ to the outer one $k_{\mathrm{F},-}$.

Using

$$\Omega = \frac{1}{2\pi k}\frac{d\Phi_\mathrm{B}}{dk}\,, \tag{4.74}$$

which follows from Eq. (4.67), we reduce the expression for $\mathcal{M}_\Omega$ to the integral

over the Berry phase:

$$\mathcal{M}_\Omega = \frac{g_\mathrm{s} e}{\hbar c} \sum_{s_1,s_2} \int \frac{d^2k}{(2\pi)^2} \, \frac{|v_\mathrm{g}|}{k} \, \frac{\Phi_\mathrm{B}}{2\pi} \, \Theta\big(\mu - E_\alpha\big) \,. \tag{4.75}$$

At this point we recall that the orbital magnetic moment $M_\alpha^\pm$ given by is related to the difference of the semiclassical and Berry phases, see Eq. (4.42). As a result, the desired combination $\mathcal{M}_M + \mathcal{M}_\Omega$ is given by the integral over the semiclassical phase:

$$\mathcal{M} = \frac{g_\mathrm{s} e}{\hbar c} \sum_{s_1,s_2} \int \frac{d^2k}{(2\pi)^2} \, \frac{|v_\mathrm{g}|}{k} \, \frac{\Phi_\mathrm{c}}{2\pi} \, \Theta\big(\mu - E_\alpha\big) \,. \tag{4.76}$$

which can be evaluated in closed form. The contribution from the two (partially occupied) conduction bands, using $g_\mathrm{s} = 2$, is

$$\mathcal{M}(\mu, U) = -\frac{e\,U}{\pi\hbar c} + \frac{e}{\pi\hbar c} \cdot \frac{E_\star}{\gamma_1} \times \begin{cases} 0 & \mu < E_\star \,, \\ 2\sqrt{\mu^2 - E_\star^2} & E_\star \le \mu < U \,, \\ \sqrt{\mu^2 - E_\star^2} + \dfrac{2U E_\star}{\gamma_1} & U \le \mu < E_\diamond \,, \\ \sqrt{4U^2 + \gamma_1^2} & E_\diamond \le \mu \,. \end{cases} \tag{4.77}$$

Here the first term, which is linear in U, is due to the fully occupied valence bands, while the additional four possible contributions describe the contribution of the conduction bands. Interestingly, once the higher energy band $s_2 = +1$ becomes occupied, $\mu > E_\diamond$, the total magnetization no longer depends on μ, because of partial cancellation between the two conduction bands.

The function $\mathcal{M}(\mu, U)$ at $U = 80\,\mathrm{meV}$ is plotted in Fig. 4.12. Similar to the Hall conductivity, it has cusps at the energies where the Fermi surface topology changes. Specifically, for the first two of them we find

$$\mathcal{M}(E_\star) = -\frac{e\,U}{\pi\hbar c} \,, \quad \mathcal{M}(U) = -\frac{e\,U}{\pi\hbar c} \cdot \frac{\gamma_1^2}{\gamma_1^2 + 4U^2} \,. \tag{4.78}$$

In Fig. 4.12, the sign of $\mathcal{M}$ is negative. However, this is unrelated to either paramagnetism or diamagnetism because the external magnetic field is assumed to be zero, in which case the K^- valley makes an equal and opposite contribution

to the total magnetization of the system. As a result, only the square of M_α contributes to the magnetic susceptibility:

$$\chi_P = M_\alpha^2\,\nu = \frac{1}{4} g^2 \mu_{\rm B}^2 \nu\,. \tag{4.79}$$

In fact, χ_P is only one of the terms (known as the Pauli paramagnetism) which determine magnetic susceptibility. As shown in previous work, [142, 143, 144, 105] the total susceptibility χ of BLG also contains the Landau diamagnetic term

$$\chi_L = -\frac{1}{3}\left(m_{\rm e}/m_{\rm eff}\right)^2 \mu_{\rm B}^2 \nu\,, \tag{4.80}$$

as well as other contributions, which together generate a very complicated dependence of χ on μ. (Here ν is the total electron density of states at the Fermi energy and $1/m_{\rm eff} = dE_\alpha^2/dk^2$ is the inverse effective mass.)

Concluding this section, we note that M_α, $\sigma_{\rm H}(\mu)$, and $\mathcal{M}(\mu)$ in BLG were previously calculated numerically in Ref. [104]. Our analytic results for M_α agree with that work. (For the ease of comparison, a second axis is included in Fig. 4.5.) On the other hand, there are noticeable differences for $\sigma_{\rm H}(\mu)$ and $\mathcal{M}(\mu)$. Regarding $\sigma_{\rm H}(\mu)$, we suspect that the authors of Ref. [104] included the effect of impurity scattering in the form of the side-jump, which we ignore. The plot of $\mathcal{M}(\mu)$ presented in Ref. [104] lacks the cusps that should be there due to the changes in the Fermi surface topology, see our Fig. 4.12.

4.6 Discussion and conclusions

In this paper we have presented a quasiclassical Landau quantization procedure which includes both the Berry phase and the magnetoelectric effects on the band structure. This method provides an intuitive picture of the Landau level dispersion and several other measurable properties of biased BLG. In some cases, we have been able to derive analytic expressions for the Landau level energies; we also discussed how they may be computed numerically.

Our results are applicable in the analysis of a number of experiments which probe transport and thermodynamic properties of BLG, including cyclotron resonance, activated conductivity, charge compressibility, and magnetization. Of

course, a more realistic calculation of these quantities should also include interaction effects. The self-consistent mean field approximation for BLG has been addressed in several published works, but generally such treatments have neglected exchange and correlation effects, which were considered in Refs. [145, 146, 147, 148] and shown to give as much as a $\sim 30\%$ correction to the mean field (Hartree) approximation, similar to the case in two-dimensional (2D) electron systems in semiconductors [111, 149][5]

Currently, experimental results for the Landau level energies from the cyclotron resonance [91] and the charge compressibility studies [98] can be fitted to the theory if undetermined variables (U, for example) are treated as adjustable parameters. Incorporating all major experimentally relevant ingredients – Hartree, exchange, and disorder contributions — into the same calculation would be a more stringent test of the theory.

Although the Landau level dispersion and therefore Landau level crossing points cannot yet be calculated with a high degree of accuracy, phenomena that may be observed at such points are quite interesting. Indeed, crossing of Landau levels has been previously studied [111, 112, 113, 114, 115, 116, 117, 118, 119, 120, 121, 122, 123, 124, 125, 126, 127, 128, 129] in the context of the quantum Hall effect in conventional 2D systems. In those systems, the crossings are between Landau levels of different subbands or between spin-split levels of different Landau levels of the same subband. Near the crossing the energy gap vanishes, and so a spike in conductance is expected. In the quantum Hall effect conditions, this is simultaneously a spike in resistance. In experiments, such spikes have been observed to be hysteretic. Sometimes, they were also accompanied by a spatial anisotropy of the transport. The leading theoretical explanation [113] attributes these phenomena to quantum Hall ferromagnetism (QHF). Namely, when two Landau level are nearly degenerate and the chemical potential is close to the crossing energy, the occupation of the Landau levels are modeled as two states pseudo-spin system. Depending on the nature of the crossing, QHF can be of either easy-axis or easy-plane type. In the former case, one expects formation of domains whose

[5][for discussion of large ν, see also][and references therein]Fogler1995cos

collective dynamics can in principle generate both hysteresis and anisotropy. The BLG appears a promising system to study QHF because of its high tunability and a rich pattern of level crossings we discussed in the paper.

We are particularly grateful to F. Guinea for valuable interactions in the early stages of this work. We also thank V. Falko and Q. Niu and for discussions. This work is supported by the NSF under Grant DMR-0706654 and ASC UCSD Grant RG209G (LMZ and MMF). DPA is grateful to the Aspen Center for Physics, where some of this work was performed.

4.7 Appendix

4.7.1 Low-energy theory of BLG

In this section we derive the low-energy of BLG by the standard method of canonical transformation. Our results are in a good agreement with previous work. [26, 56, 27] Some minor discrepancies can be attributed to typographic errors therein or differences in notations.

We begin with the Hamiltonian of Eq. (1.10). The bilayer's electronic structure has four bands. When $\mathbf{q} = \mathbf{K}^{\pm}$, the two central levels lie at $E = \pm U$. For $|S_{\mathbf{q}}| \ll 1$, where $S_{\mathbf{q}}$ is given in Eq. (1.2), we can derive an effective 2×2 Hamiltonian by writing

$$H_{\mathbf{K}+\mathbf{k}} = H^0 + V\,, \tag{4.81}$$

where $H^0 = H(\mathbf{K}^{\pm})$ contains terms dependent on γ_1, Δ', and U, and V contains the $\gamma_0 S_{\mathbf{q}}$, $\gamma_3 S_{\mathbf{q}}$, and $\gamma_4 S_{\mathbf{q}}$ terms. (To lighten notations, the subscript $\mathbf{q}$ is dropped in the following.)

The unperturbed Hamiltonian H^0 has levels $E^0_{1,4} = \mp\sqrt{\gamma_1^2 + U^2}$ and $E^0_{2,3} = \Delta' \mp U$. The eigenfunctions $\left|\psi_j\right\rangle$ are the column vectors of the matrix

$$\Psi = \begin{pmatrix} 0 & 1 & 0 & 0 \\ \cos(\theta/2) & 0 & 0 & \sin(\theta/2) \\ -\sin(\theta/2) & 0 & 0 & \cos(\theta/2) \\ 0 & 0 & 1 & 0 \end{pmatrix}, \tag{4.82}$$

where $\tan\theta = \gamma_1/U$. Eliminating the high energy subspace spanned by $\left|\psi_{1,4}\right\rangle$ by unitary transformation

$$\widetilde{H} = e^{iQ} H e^{-iQ}\,, \tag{4.83}$$

we obtain the effective 2×2 Hamiltonian

$$\begin{aligned}\widetilde{H}_{nn'} &= E_n^0\,\delta_{nn'} + V_{nn'} \\ &\quad + \frac{1}{2}\sum_a \left(\frac{1}{E_n^0 - E_a^0} + \frac{1}{E_{n'}^0 - E_a^0}\right) V_{na}\,V_{an'}\,,\end{aligned} \tag{4.84}$$

up to terms of order V^2. Here $n, n' \in \{2,3\}$ are labels for the low energy subspace, while $a \in \{1,4\}$ labels the high energy subspace, and $V_{ij} = \left\langle \psi_i \left| V \right| \psi_j \right\rangle$. The matrix elements of Q are given by

$$\begin{aligned}Q_{na} = i\,\frac{V_{na}}{E_a^0 - E_n^0} &+ i\sum_{n'} \frac{V_{nn'}V_{n'a}}{(E_a^0 - E_n^0)(E_a^0 - E_{n'}^0)} \\ &- i\sum_{a'} \frac{V_{na'}V_{a'a}}{(E_a^0 - E_n^0)(E_{a'}^0 - E_n^0)} + o(V^2)\,,\end{aligned} \tag{4.85}$$

with $Q_{an} = (Q_{an})^\dagger$.

Proceeding in this manner, we obtain the 2×2 block for the inner bands,

$$\widetilde{H} = \begin{pmatrix} \varepsilon_0 - U + \omega & \xi \\ \xi^* & \varepsilon_0 + U - \omega \end{pmatrix}\,, \tag{4.86}$$

where, to lowest order in U and Δ',

$$\varepsilon_0 = \left(\frac{\gamma_0\gamma_4}{\gamma_1} + \frac{(\gamma_0^2+\gamma_4^2)\,\Delta'}{2\gamma_1^2}\right)\left\{S, S^\dagger\right\} + \frac{U\gamma_0^2}{\gamma_1^2}\left[S, S^\dagger\right], \tag{4.87}$$

$$\omega = \frac{U\gamma_0^2}{\gamma_1^2}\left\{S, S^\dagger\right\} + \left(\frac{\gamma_0\gamma_4}{\gamma_1} + \frac{(\gamma_0^2+\gamma_4^2)\,\Delta'}{2\gamma_1^2}\right)\left[S, S^\dagger\right], \tag{4.88}$$

$$\xi = \gamma_3\,S^\dagger - \left(\frac{\gamma_0^2+\gamma_4^2}{\gamma_1} + \frac{2\gamma_0\gamma_4\Delta'}{\gamma_1^2}\right)S^2\,. \tag{4.89}$$

Anticipating the introduction of an external magnetic field, we have allowed for the possibility that S and $S^\dagger$ do not commute. Recognizing that $\gamma_4/\gamma_0 = 0.05 \ll 1$,

it is permissible to drop the terms of order γ_4^2 and $\gamma_4\Delta'$, in which case

$$\varepsilon_0 = \frac{\gamma_0^2\,\widetilde{\Delta}}{2\gamma_1^2}\left\{S, S^\dagger\right\} + \frac{U\gamma_0^2}{\gamma_1^2}\left[S, S^\dagger\right], \tag{4.90}$$

$$\omega = \frac{U\gamma_0^2}{\gamma_1^2}\left\{S, S^\dagger\right\} + \frac{\gamma_0^2\,\widetilde{\Delta}}{2\gamma_1^2}\left[S, S^\dagger\right], \tag{4.91}$$

$$\xi = \gamma_3\, S^\dagger - \frac{\gamma_0^2}{\gamma_1} S^2\,, \tag{4.92}$$

leading to Eq. (4.21). Our results agree with those of Ref. [26] if Δ' and γ_4 are set to zero.

For $B = 0$, in the vicinity of the $\mathbf{K}^\pm$ points, the four bands disperse as shown in Fig. 1.3. The two central bands, which comprise the low energy sector, are separated by $2U$ at $\mathbf{k} = 0$. Their dispersion is described by the effective Hamiltonian of Eq. (4.86). One finds that for $\mathbf{k} = k\,\hat{\mathbf{x}}$ the central bands have a characteristic double hump (or Mexican hat) shape provided $U > 2\gamma_1\gamma_3/\gamma_0 \approx 80\,\text{meV}$.

It is convenient to write $\widetilde{H} = \varepsilon_0 + \boldsymbol{\mathcal{B}}(\mathbf{k})\,\boldsymbol{\text{œ}}$, where $\mathcal{B}_z = \omega$, $\mathcal{B}_x - i\mathcal{B}_y = \xi$, and $\boldsymbol{\text{œ}}$ is the vector of Pauli matrices. When the actual magnetic field B vanishes,

$$\varepsilon_0 = \frac{\widetilde{\Delta}\,\varepsilon_k^2}{\gamma_1^2}\,, \quad \omega = \frac{2\varepsilon_k^2}{\gamma_1^2}\,U\,, \tag{4.93}$$

$$\xi = \frac{\gamma_3}{\gamma_0}\,\varepsilon_k\, e^{-i\varphi} - \frac{\varepsilon_k^2}{\gamma_1}\, e^{+2i\varphi}\,, \tag{4.94}$$

where $\varepsilon_k = \hbar v_0 k$, the origin in $\mathbf{k}$-space is taken as one of the $K^\pm$ points, and $\varphi = \tan^{-1}(k_y/k_x)$ is the corresponding polar angle. The eigenvalues are

$$\widetilde{E}_{s_1,-,\mathbf{k}} = \varepsilon_0 + s_1|\boldsymbol{\mathcal{B}}(\mathbf{k})|\,. \tag{4.95}$$

Let us now discuss the Berry phase. Semiclassically, in the presence of a weak magnetic field, the wavevector $\mathbf{k}$ evolves in time according to Eq. (4.47):

$$\dot{\mathbf{k}} = \omega_{\rm c}\,\hat{\mathbf{z}} \times \mathbf{k} \quad , \quad \omega_{\rm c} \equiv \frac{2\pi}{T}\,\text{sgn}(v_{\rm g})\,.$$

If we can neglect γ_3, then the trajectory the pseudospin traces on the Bloch sphere winds *twice* for every cycle of $\mathbf{k}$, owing to the $e^{2i\varphi}$ factor in $\mathcal{B}_x - i\mathcal{B}_y = \xi$. Therefore, the accumulated Berry phase is equal to $2 \times \frac{1}{2} = 1$ times the solid angle traced

by vector $\boldsymbol{\mathcal{B}}(\mathbf{k})$. Actually, the Berry phase is defined modulo 2π. To be consistent with the earlier choice of the overall phase factor of the basis state (4.37), we need to subtract 2π from the solid angle. The result is

$$\Phi'_{\rm B} = 2\pi\left(1+\frac{\mathcal{B}_z}{|\boldsymbol{\mathcal{B}}|}\right) - 2\pi = \frac{2\pi U}{E_{s_1,-,k}}\left(\frac{2\varepsilon_k^2}{\gamma_1^2}-1\right). \tag{4.96}$$

However, it differs from our earlier Eq. (4.55) for the Berry phase in BLG. The discrepancy arises due to the canonical transformation by which we obtain the wavefunction in the new basis: $|\psi'\rangle = e^{-i\mathcal{S}}\,|\psi\rangle$:

$$\begin{aligned}\delta\Phi \equiv \Phi_{\rm B} - \Phi'_{\rm B} &= -2\pi i\left\langle \psi' \left| e^{i\mathcal{S}}\,\partial_\varphi\, e^{-i\mathcal{S}}\right| \psi'\right\rangle \\ &= 2\pi\frac{\varepsilon_k^2}{\gamma_1^2}\frac{\mathcal{B}_z}{|\boldsymbol{\mathcal{B}}|} \simeq \frac{\varepsilon_k^2}{\gamma_1^2}\,\frac{2\pi U}{E_{s_1,-,k}}\,.\end{aligned} \tag{4.97}$$

The combined phase $\Phi_{\rm B} = \Phi'_{\rm B} + \delta\Phi$ agrees with the four-band expression Eq. (4.55), to within the accuracy of this calculation.

Finally, we can go beyond the semiclassical approximation, obtaining the effective Hamiltonian in Eq. (4.24). If γ_3 is neglected, each pseudospin component Landau level is connected to a unique mate, and the Hamiltonian breaks up into a direct sum of 2×2 blocks, given by Eq. (4.26) ($n=-1$ and $n=0$ are special cases where $\widetilde{H}$ reduces to a scalar).

4.7.2 Matrix representation of the Hamiltonian in a finite magnetic field

In the presence of a magnetic field, the full Hamiltonian $\mathcal{H}^+$ in the K^+ valley is given by Eq. (4.4),

$$\mathcal{H}^+ = \begin{pmatrix} -U & -\omega_0\, a & \eta_4\,\omega_0\, a & \eta_3\,\omega_0\, a^\dagger \\ -\omega_0\, a^\dagger & -U+\Delta' & \gamma_1 & \eta_4\,\omega_0\, a \\ \eta_4\,\omega_0\, a^\dagger & \gamma_1 & U+\Delta' & -\omega_0\, a \\ \eta_3\,\omega_0\, a & \eta_4\,\omega_0\, a^\dagger & -\omega_0\, a^\dagger & U \end{pmatrix},$$

where a and $a^\dagger$ are Landau level lowering and raising operators, respectively. In the occupation number basis $|n\rangle$, the matrix elements of $\mathcal{H}^+$ can be understood

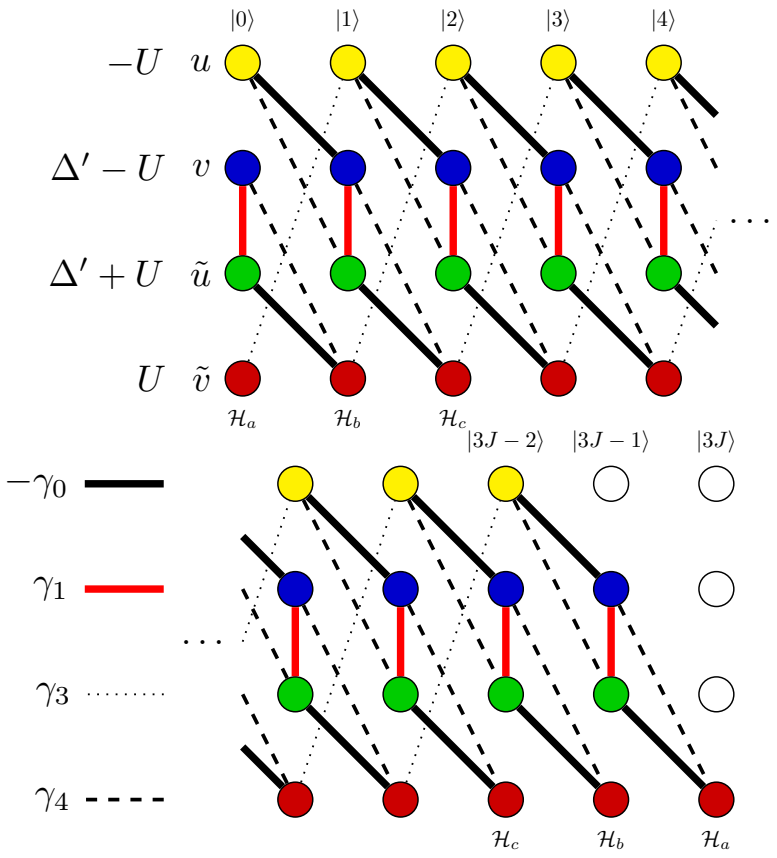

Figure 4.13: Sketch of the structure of the magnetic bilayer Hamiltonian, showing nonzero matrix elements as links. Each link between orbitals in column n and column $n+1$ is multiplied by a factor $\sqrt{n+1}\,(\omega_0/\gamma_0)$. The diagonal entries in the Hamiltonian for each orbital are given at the upper left. When $\gamma_3 = 0$, the Hamiltonian breaks up into a direct sum of 4×4 blocks.

pictorially, by referring to Fig. 4.13. Writing the general wavefunction as

$$|\Psi\rangle = \sum_{n=0}^{\infty} \Big(u_n \,|n\rangle \,,\, v_n \,|n\rangle \,,\, \tilde{u}_n \,|n\rangle \,,\, \tilde{v}_n \,|n\rangle \Big)^{\mathsf{T}} , \tag{4.98}$$

the links in Fig. 4.13 indicate matrix elements between components $\{u_n, v_n, \tilde{u}_n, \tilde{v}_n\}$.

One finds that $\mathcal{H} = \mathcal{H}_{\rm a} \oplus \mathcal{H}_{\rm b} \oplus \mathcal{H}_{\rm c}$ can be written as a direct sum of three terms. In evaluating the spectrum numerically, we truncate $\mathcal{H}_{\rm a,b,c}$ at a high Landau level index, as shown in the figure. Typically we chose a maximum index of $n_{\rm max} \approx 300$, checking that spectrum did not vary significantly as the upper index cutoff was further increased. This feature is most evident at high fields, such as in Fig. 4.14, where we have taken $B = 20\,{\rm T}$. The spectrum of $\mathcal{H}_{\rm a}$ is shown in black, that of $\mathcal{H}_{\rm b}$ in red, and that of $\mathcal{H}_{\rm c}$ in blue. Solid lines correspond to the K^+ valley and broken lines to the K^- valley. One sees in the figure that curves of the same color and line type cannot cross at an accidental degeneracy.

Frequently in this paper we have ignored the SWMc parameter γ_3, setting it to zero, In this approximation, as can be seen from Fig. 4.13, the occupation number space Hamiltonian further resolves itself into a direct sum of 4×4 blocks, given by the expression in Eq. (4.15), which connect $\{u_{n-1}\,,\, v_n\,,\, \tilde{u}_n\,,\, v_{n+1}\}$ for each n. (There is also a remaining 1×1 and 3×3 block associated with the indices $n = 0$ and $n = 1$.)

In addition to eigenvalues, we also calculated the eigenfunctions, one of which is shown in Fig. 4.8. To do so we chose the symmetric gauge, where the Bloch wavefunctions of $|m\rangle$ oscillator states are given by

$$\langle \mathbf{k}| \, n\rangle = \frac{\ell_B^{m+1}}{\sqrt{m!}} \left(\frac{k_x - i k_y}{\sqrt{2}} \right)^m e^{-k^2 \ell_B^2/4} \,. \tag{4.99}$$

These basis states were weighted with the coefficients obtained from diagonalizing the Hamiltonian matrix and then summed over all components (both n and the sublattice index).

From these calculations we concluded that the effect of γ_3 diminishes as B increases, as was previously observed in Ref. [26] The semiclassical argument that explains this behavior was given in Sec. 4.4.2. Here we mention another reasoning, [26] which is based on the usual perturbation theory.

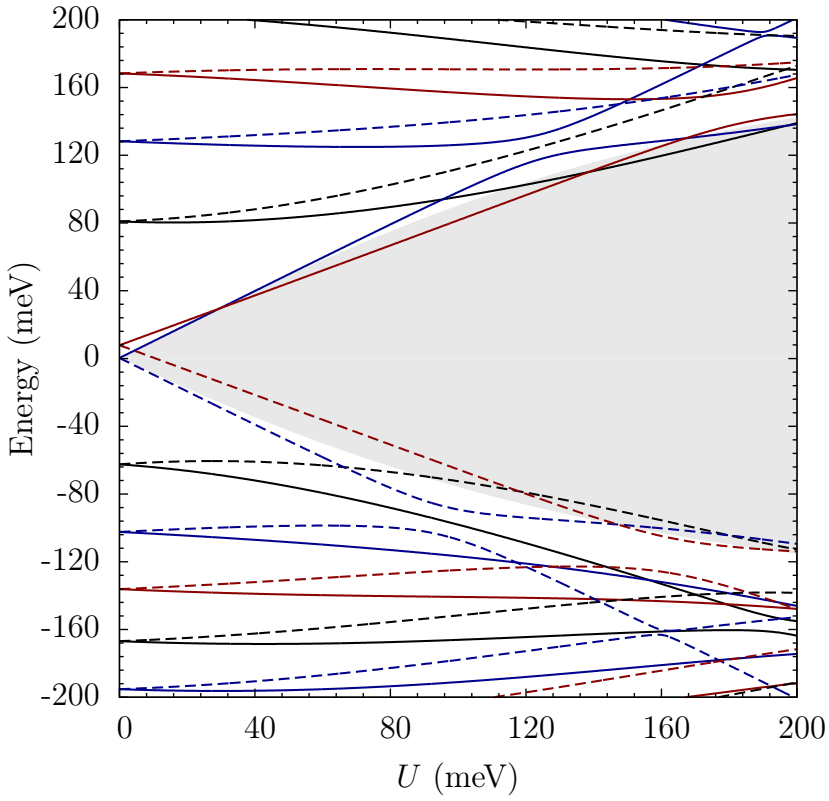

Figure 4.14: Landau level energies *vs.* interlayer bias U for a field value $B = 20\,\mathrm{T}$. Solid lines correspond to the K^+ valley and broken lines to the K^- valley. The color and line type are as in Fig. 4.3. The shaded area indicates the energy gap at $B = 0$.

The leading-order correction to the energies due to γ_3 is approximately $\omega_0^2/\Delta E$, where $\Delta E \approx \hbar|v_{\rm g}|/(k\ell_B^2)$ is the Landau level spacing. Therefore, the relative magnitude of this energy shift is small provided

$$\gamma_3 \ll \frac{\gamma_0}{k\ell_B}\,. \tag{4.100}$$

At $U = 0$ and $\varepsilon_k \ll \gamma_1$ this inequality gives [26] $\omega_0 \gg \gamma_3\gamma_1/\gamma_0$, which is roughly consistent with the threshold $B \sim 1\,\mathrm{T}$ where the effect of γ_3 is observed to become insignificant in the numerical calculations. On the other hand, at finite U and near the bottom of the Mexican hat, where $v_{\rm g} = 0$, the expression on the right-hand side of Eq. (4.100) diverges. This implies that the effect of γ_3 is larger and persists to higher B. This is also consistent with the numerics, see Sec. 4.4.2.

4.8 Acknowledgement

Chapter 4, almost in full, is a reprint of an unpublished manuscript submitted to *Phys. Rev. B* in 2010. The dissertation author was the primary investigator and author of this paper.

Bibliography

[1] L. M. Zhang, Z. Q. Li, D. N. Basov, M. M. Fogler, Z. Hao, and M. C. Martin, Phys. Rev. B **78**, 235408 (2008).

[2] L. M. Zhang and M. M. Fogler, Nano Lett. **6**, 2206 (2006).

[3] L. M. Zhang and M. M. Fogler, Phys. Rev. Lett. **100**, 116804 (2008).

[4] L. M. Zhang, M. M. Fogler, and D. P. Arovas, "Magnetoelectric coupling, berry phase, and landau level dispersion in a biased bilayer graphene," (2010), (Unpublished).

[5] K. S. Novoselov, A. K. Geim, S. V. Morozov, D. Jiang, Y. Zhang, S. V. Dubonos, I. V. Grigorieva, and A. A. Firsov, Science **306**, 666 (2004).

[6] A. K. Geim and K. S. Novoselov, Nat. Mat. **6**, 183 (2007).

[7] D. S. L. Abergel, A. Russell, and V. I. Fal'ko, App. Phys. Lett. **91**, 063125 (2007).

[8] P. R. Wallace, Phys. Rev. **71**, 622 (May 1947).

[9] J. W. McClure, Phys. Rev. **108**, 612 (Nov 1957).

[10] J. C. Slonczewski and P. R. Weiss, Phys. Rev. **109**, 272 (Jan 1958).

[11] W. S. Boyle and P. Nozières, Phys. Rev. **111**, 782 (Aug 1958).

[12] J. W. McClure, Phys. Rev. **112**, 715 (Nov 1958).

[13] D. E. Soule, J. W. McClure, and L. B. Smith, Phys. Rev. **134**, A453 (Apr 1964).

[14] M. S. Dresselhaus, G. Dresselhaus, and J. E. Fischer, Phys. Rev. B **15**, 3180 (Mar 1977).

[15] R. O. Dillon, I. L. Spain, and J. W. McClure, J. Phys. Chem. Sol. **38**, 635 (1977).

[16] N. B. Brandt, S. M. Chudinov, and Y. G. Ponomarev, *Semimetals I: Graphite and its Compounds* (North-Holland, Amsterdam, 1988).

[17] J.-C. Charlier, X. Gonze, and J.-P. Michenaud, Phys. Rev. B **43**, 4579 (Feb 1991).

[18] J.-C. Charlier, X. Gonze, and J.-P. Michenaud, Eur. Phys. Lett. **28**, 403 (Nov 1994).

[19] H. Rydberg, M. Dion, N. Jacobson, E. Schröder, P. Hyldgaard, S. I. Simak, D. C. Langreth, and B. I. Lundqvist, Phys. Rev. Lett. **91**, 126402 (Sep 2003).

[20] A. Castro Neto, F. Guinea, and N. M. Peres, Phys. World **19**, 33âĂŞ37 (2006).

[21] M. I. Katsnelson, Eur. Phys. Jour. B **51**, 157 (2006), ISSN 1434-6028.

[22] M. I. Katsnelson and K. S. Novoselov, Solid State Commun. **143**, 3 (Jul. 2007), ISSN 0038-1098.

[23] A. Calogeracos and N. Dombey, Contemporary Physics **40**, 313 (Sep 1999).

[24] C. Itzykson and J.-B. Zuber, *Quantum Field Theory* (Dover, New York, 2006).

[25] A. H. Castro Neto, F. Guinea, N. M. R. Peres, K. S. Novoselov, and A. K. Geim, Rev. Mod. Phys. **81**, 109 (2009).

[26] E. McCann and V. I. Fal'ko, Phys. Rev. Lett. **96**, 086805 (2006).

[27] J. Nilsson, A. H. Castro Neto, F. Guinea, and N. M. R. Peres, Phys. Rev. B **78**, 045405 (2008).

[28] B. Huard, J. A. Sulpizio, N. Stander, K. Todd, B. Yang, and D. Goldhaber-Gordon, Phys. Rev. Lett. **98**, 236803 (Jun 2007).

[29] M. I. Katsnelson, K. Novoselov, and A. Geim, Nat. Phys. **2**, 620 (Aug 2006).

[30] V. V. Cheianov and V. I. Fal'ko, Phys. Rev. B **74**, 041403 (2006).

[31] V. V. Cheianov, V. Fal'ko, and B. L. Altshuler, Science **315**, 1252 (2007).

[32] M. V. Fistul and K. B. Efetov, Phys. Rev. Lett. **98**, 256803 (Jun 2007).

[33] A. Ossipov, M. Titov, and C. W. J. Beenakker, Phys. Rev. B **75**, 241401 (Jun 2007).

[34] E. O. Kane and E. I. Blount, "Tunneling phenomena in solids," (Plenum, New York, 1969) pp. 79–91.

[35] T. Ando, J. Phys. Soc. Jpn. **75**, 074716 (2006).

[36] M. M. Fogler, D. S. Novikov, and B. I. Shklovskii, Phys. Rev. B **76**, 233402 (2007).

[37] M. M. Fogler, D. S. Novikov, L. I. Glazman, and B. I. Shklovskii, Phys. Rev. B **77**, 075420 (Feb 2008).

[38] P. M. Morse and H. Feshbach, *Methods of Theoretical Physics* (McGraw-Hill, New York, 1953).

[39] I. S. Gradshteyn and I. M. Ryzhik, *Table of Integrals, Series, and Products*, 6th ed. (Academic, San Diego, 2000).

[40] A. V. Andreev, Phys. Rev. Lett. **99**, 247204 (2007).

[41] J. L. Carter and J. A. Krumhansl, J. Phys. Chem. **21**, 2238 (1953).

[42] B. Partoens and F. M. Peeters, Phys. Rev. B **74**, 075404 (2006).

[43] M. Dresselhaus and G. Dresselhaus, Adv. Phys. **30**, 139 (April 1981).

[44] M. S. Dresselhaus and G. Dresselhaus, Adv. Phys. **51**, 1 (2002).

[45] L. M. Malard, J. Nilsson, D. C. Elias, J. C. Brant, F. Plentz, E. S. Alves, A. H. Castro Neto, and M. A. Pimenta, Phys. Rev. B **76**, 201401(R) (2007).

[46] W. W. Toy, M. S. Dresselhaus, and G. Dresselhaus, Phys. Rev. B **15**, 4077 (Apr 1977).

[47] D. D. L. Chung, J. Mat. Sci. **37**, 1475 (April 2002).

[48] R. C. Tatar and S. Rabii, Phys. Rev. B **25**, 4126 (Mar 1982).

[49] A. Grüneis, C. Attaccalite, T. Pichler, V. Zabolotnyy, H. Shiozawa, S. L. Molodtsov, D. Inosov, A. Koitzsch, M. Knupfer, J. Schiessling, R. Follath, R. Weber, P. Rudolf, L. Wirtz, and A. Rubio, Phys. Rev. Lett. **100**, 037601 (2008).

[50] S. B. Trickey, F. Müller-Plathe, G. H. F. Diercksen, and J. C. Boettger, Phys. Rev. B **45**, 4460 (Feb 1992).

[51] S. Latil and L. Henrard, Phys. Rev. Lett. **97**, 036803 (2006).

[52] S. Latil, V. Meunier, and L. Henrard, Phys. Rev. B **76**, 201402(R) (2007).

[53] H. Min, B. Sahu, S. K. Banerjee, and A. H. MacDonald, Phys. Rev. B **75**, 155115 (2007).

[54] M. Aoki and H. Amawashi, Solid State Commun. **142**, 123 (2007).

[55] M. Orlita, C. Faugeras, G. Martinez, D. K. Maude, M. L. Sadowski, and M. Potemski, Phys. Rev. Lett. **100**, 136403 (2008).

[56] E. McCann, D. Abergel, and V. Fal'ko, Solid State Commun. **143**, 110 (2007).

[57] F. Guinea, A. H. Castro Neto, and N. M. R. Peres, Phys. Rev. B **73**, 245426 (2006).

[58] E. V. Castro, K. S. Novoselov, S. V. Morozov, N. M. R. Peres, J. M. B. L. dos Santos, J. Nilsson, F. Guinea, A. K. Geim, and A. H. Castro Neto, Phys. Rev. Lett. **99**, 216802 (2007).

[59] J. B. Oostinga, H. B. Heersche, X. Liu, A. F. Morpurgo, and L. M. K. Vandersypen, Nat. Mat. **7**, 151 (2007).

[60] T. Ohta, A. Bostwick, T. Seyller, K. Horn, and E. Rotenberg, Science **313**, 951 (2006).

[61] Z. Q. Li, E. A. Henriksen, Z. Jiang, Z. Hao, M. C. Martin, P. Kim, H. L. Stormer, and D. N. Basov, Phys. Rev. Lett. **102**, 037403 (Jan 2009).

[62] F. Wang, Y. Zhang, C. Tian, C. Girit, A. Zettl, M. Crommie, and Y. R. Shen, Science **320**, 206 (2008).

[63] A. B. Kuzmenko, E. van Heumen, D. van der Marel, P. Lerch, P. Blake, K. S. Novoselov, and A. K. Geim, Phys. Rev. B **79**, 115441 (2009).

[64] D. S. L. Abergel and V. I. Fal'ko, Phys. Rev. B **75**, 155430 (2007).

[65] L. Benfatto, S. G. Sharapov, and J. P. Carbotte, Phys. Rev. B **77**, 125422 (2008).

[66] E. J. Nicol and J. P. Carbotte, Phys. Rev. B **77**, 155409 (2008).

[67] T. Ando, Y. S. Zheng, and H. Suzuura, J. Phys. Soc. Jpn. **71**, 1318 (2002).

[68] R. R. Nair, P. Blake, A. N. Grigorenko, K. S. Novoselov, T. J. Booth, T. Stauber, N. M. R. Peres, and A. K. Geim, Science **320**, 1308 (2008).

[69] V. P. Gusynin, V. P. Sharapov, and J. P. Carbotte, Int. J. of Mod. Phys. B **21**, 4611 (2007).

[70] E. McCann, Phys. Rev. B **74**, 161403 (2006).

[71] E. V. Castro, K. S. Novoselov, S. V. Morozov, N. M. R. Peres, J. M. B. Lopes dos Santos, J. Nilsson, F. Guinea, A. K. Geim, and A. H. Castro Neto, J. Phys. Cond. Matt. **22**, 175503 (2010).

[72] Z. Q. Li, E. A. Henriksen, Z. Jiang, Z. Hao, M. C. Martin, P. Kim, H. L. Stormer, and D. N. Basov, Nat. Phys. **4**, 532 (2008).

[73] Z. Q. Li, V. Podzorov, N. Sai, M. C. Martin, M. E. Gershenson, M. Di Ventra, and D. N. Basov, Phys. Rev. Lett. **99**, 016403 (2007).

[74] T. Stauber, N. M. R. Peres, and A. H. Castro Neto, Phys. Rev. B **78**, 085418 (2008).

[75] G. D. Mahan, *Many-Particle Physics* (Plenum, New York, 1990).

[76] A. H. R. Palser, Phys. Chem. Chem. Phys. **1**, 4459 (1999).

[77] A. N. Kolmogorov and V. H. Crespi, Phys. Rev. B **71**, 235415 (2005).

[78] I. Martin, Y. M. Blanter, and A. F. Morpurgo, Phys. Rev. Lett. **100**, 036804 (2008).

[79] J. D. Jackson, *Classical Electrodynamics* (Wiley, New York, 1998).

[80] J. Nilsson, A. H. Castro Neto, F. Guinea, and N. M. R. Peres, Phys. Rev. Lett. **97**, 266801 (2006).

[81] J. Nilsson, A. H. Castro Neto, N. M. R. Peres, and F. Guinea, Phys. Rev. B **73**, 214418 (2006).

[82] H. Min, G. Borghi, M. Polini, and A. H. MacDonald, Phys. Rev. B **77**, 041407(R) (2008).

[83] F. Zhang, H. Min, M. Polini, and A. H. MacDonald, Phys. Rev. B **81**, 041402 (Jan 2010).

[84] R. Nandkishore and L. Levitov, Phys. Rev. Lett. **104**, 156803 (2010).

[85] O. Vafek and K. Yang, Phys. Rev. B **81**, 041401 (2010).

[86] Y. Lemonik, I. L. Aleiner, C. Toke, and V. I. Falko, "Spontaneous symmetry breaking and lifshitz transition in bilayer graphene," (2010), (Unpublished), arXiv:1006.1399 [cond-mat].

[87] B. E. Feldman, J. Martin, and A. Yacoby, Nat. Phys. **5**, 889 (dec 2009).

[88] Y. Zhao, P. Cadden-Zimansky, Z. Jiang, and P. Kim, Phys. Rev. Lett. **104**, 066801 (2010).

[89] Y. Zhang, Yan-Wen, T. H. L. Stormer, and P. Kim, Nature **438**, 201 (2005).

[90] K. S. Novoselov, E. McCann, S. V. Morozov, V. I. Fal'ko, M. I. Katnelson, U. Zeitler, D. Jiang, F. Schedin, and A. K. Geim, Nat. Phys. **2**, 177 (2006).

[91] E. A. Henriksen, Z. Jiang, L.-C. Tung, M. E. Schwartz, M. Takita, Y.-J. Wang, P. Kim, and H. L. Stormer, Phys. Rev. Lett. **100**, 087403 (2008).

[92] K. F. Mak, C. H. Lui, J. Shan, and T. F. Heinz, Phys. Rev. Lett. **102**, 256405 (2009).

[93] A. B. Kuzmenko, I. Crassee, D. van der Marel, P. Blake, and K. S. Novoselov, Phys. Rev. B **80**, 165406 (2009).

[94] A. B. Kuzmenko, L. Benfatto, E. Cappelluti, I. Crassee, D. van der Marel, P. Blake, K. S. Novoselov, and A. K. Geim, Phys. Rev. Lett. **103**, 116804 (2009).

[95] Y. Zhang, T.-T. Tang, C. Girit, Z. Hao, M. C. Martin, A. Zettl, M. F. Crommie, Y. R. Shen, and F. Wang, Nature **459**, 820 (2009).

[96] M. M. Fogler and E. McCann, "Screening in gated bilayer graphene via variational calculus," (Mar. 2010), (Unpublished), arXiv:1003.5607 [cond-mat].

[97] S. Kim and E. Tutuc, "Quantum hall effect in dual-gated graphene bilayers with tunable layer density imbalance," (Sep 2009), (Unpublished), arXiv:0909.2288 [cond-mat].

[98] E. A. Henriksen and J. P. Eisenstein, "Measurement of the electronic compressibility of bilayer graphene," (2010), (Unpublished), arXiv:1004.2543 [cond-mat].

[99] M. V. Berry, Proc. Roy. Soc. London, Ser. A **392**, 45 (1984).

[100] A. Shapere and F. Wilczek, *Geometric Phases in Physics* (World Scientific, Singapore, 1989).

[101] G. P. Mikitik and Y. V. Sharlai, Phys. Rev. Lett. **82**, 2147 (Mar 1999).

[102] Y. Zheng and T. Ando, Phys. Rev. B **65**, 245420 (2002).

[103] V. P. Gusynin and S. G. Sharapov, Phys. Rev. Lett. **95**, 146801 (Sep 2005).

[104] D. Xiao, W. Yao, and Q. Niu, Phys. Rev. Lett. **99**, 236809 (Dec 2007).

[105] M. Koshino and T. Ando, Phys. Rev. B **81**, 195431 (2010).

[106] X.-L. Qi, T. L. Hughes, and S.-C. Zhang, Phys. Rev. B **78**, 195424 (Nov 2008).

[107] L. A. Falkovsky, Sov. Phys. JETP **22**, 423 (1966).

[108] M. Mucha-Kruczynski, E. McCann, and V. Fal'ko, Solid State Commun. **149**, 1111 (2009).

[109] M. Mucha-Kruczynski, D. S. L. Abergel, E. McCann, and V. I. Fal'ko, J. Phys.: Condens. Mat. **21**, 344206 (2009).

[110] M. Koshino and E. McCann, Phys. Rev. B **81**, 115315 (2010).

[111] C. Kallin and B. I. Halperin, Phys. Rev. B **30**, 5655 (1984).

[112] V. I. Fal'ko, Phys. Rev. Lett. **71**, 141 (Jul 1993).

[113] T. Jungwirth, S. P. Shukla, L. Smrčka, M. Shayegan, and A. H. MacDonald, Phys. Rev. Lett. **81**, 2328 (Sep 1998).

[114] T. Jungwirth and A. H. MacDonald, Phys. Rev. B **63**, 035305 (Dec 2000).

[115] J. T. Chalker, D. G. Polyakov, F. Evers, A. D. Mirlin, and P. Wölfle, Phys. Rev. B **66**, 161317 (Oct 2002).

[116] D.-W. Wang, S. Das Sarma, E. Demler, and B. I. Halperin, Phys. Rev. B **66**, 195334 (Nov 2002).

[117] E. H. Rezayi, T. Jungwirth, A. H. MacDonald, and F. D. M. Haldane, Phys. Rev. B **67**, 201305 (May 2003).

[118] S. Koch, R. J. Haug, K. v. Klitzing, and M. Razeghi, Phys. Rev. B **47**, 4048 (Feb 1993).

[119] H. Cho, J. B. Young, W. Kang, K. L. Campman, A. C. Gossard, M. Bichler, and W. Wegscheider, Phys. Rev. Lett. **81**, 2522 (Sep 1998).

[120] V. Piazza, V. Pellegrini, F. Beltram, W. Wegscheider, T. Jungwirth, and . A. H. MacDonald, Nature **402**, 638 (1999).

[121] E. P. De Poortere, E. Tutuc, S. J. Papadakis, and M. Shayegan, Science **290**, 1546 (2000).

[122] J. Eom, H. Cho, W. Kang, K. L. Campman, A. C. Gossard, M. Bichler, and W. Wegscheider, Science **289**, 2320 (2000).

[123] U. Zeitler, H. W. Schumacher, A. G. M. Jansen, and R. J. Haug, Phys. Rev. Lett. **86**, 866 (Jan 2001).

[124] E. P. De Poortere, E. Tutuc, and M. Shayegan, Phys. Rev. Lett. **91**, 216802 (Nov 2003).

[125] W. Pan, H. L. Stormer, D. C. Tsui, L. N. Pfeiffer, K. W. Baldwin, and K. W. West, Phys. Rev. B **64**, 121305 (Sep 2001).

[126] X. C. Zhang, D. R. Faulhaber, and H. W. Jiang, Phys. Rev. Lett. **95**, 216801 (Nov 2005).

[127] X. C. Zhang, I. Martin, and H. W. Jiang, Phys. Rev. B **74**, 073301 (Aug 2006).

[128] V. P. Gusynin and S. G. Sharapov, Phys. Rev. B **73**, 245411 (Jun 2006).

[129] F. Fischer, R. Winkler, D. Schuh, M. Bichler, and M. Grayson, Phys. Rev. B **75**, 073303 (Feb 2007).

[130] E. M. Lifshitz and L. P. Pitaevskii, *Statistical Physics, Pt. 2* (Pergamon, Oxford, 1980).

[131] M.-C. Chang and Q. Niu, Phys. Rev. B **53**, 7010 (Mar 1996).

[132] G. Sundaram and Q. Niu, Phys. Rev. B **59**, 14915 (Jun 1999).

[133] L. Onsager, Phil. Mag. **43**, 1006 (1952).

[134] R. G. Littlejohn and W. G. Flynn, Phys. Rev. Lett. **66**, 2839 (Jun 1991).

[135] R. G. Littlejohn and W. G. Flynn, Phys. Rev. A **44**, 5239 (Oct 1991).

[136] P. Carmier and D. Ullmo, Phys. Rev. B **77**, 245413 (2008).

[137] P. Gosselin, H. Boumrar, and H. Mohrbach, Eur. Phys. Lett. **84**, 50002 (2008).

[138] D. Xiao, M.-C. Chang, and Q. Niu, Rev. Mod. Phys. **82**, 1959 (2010).

[139] A. Rycerz, J. Tworzydło, and C. W. J. Beenakker, Nat. Phys. **3**, 172 (2007).

[140] W. Yao, D. Xiao, and Q. Niu, Phys. Rev. B **77**, 235406 (Jun 2008).

[141] A. S. Moskalenko and J. Berakdar, Phys. Rev. B **80**, 193407 (Nov 2009).

[142] S. A. Safran, Phys. Rev. B **30**, 421 (1984).

[143] R. Saito and H. Kamimura, Phys. Rev. B **33**, 7218 (1986).

[144] M. Koshino and T. Ando, Phys. Rev. B **76**, 085425 (2007).

[145] Y. Barlas, R. Côté, K. Nomura, and A. H. MacDonald, Phys. Rev. Lett. **101**, 097601 (2008).

[146] S. Viola Kusminskiy, D. K. Campbell, and A. H. Castro Neto, Eur. Phys. Lett. **85**, 58005 (2009).

[147] D. S. L. Abergel and T. Chakraborty, Phys. Rev. Lett. **102**, 056807 (2009).

[148] D. A. Abanin, S. A. Parameswaran, and S. L. Sondhi, Phys. Rev. Lett. **103**, 076802 (2009).

[149] M. M. Fogler and B. I. Shklovskii, Phys. Rev. B **52**, 17366 (1995).